Designing and Measuring Novel Van der Waals Semiconductor Photonic Devices

by

Eunice Paik

A dissertation submitted in partial fulfillment
of the requirements for the degree of
Doctor of Philosophy
(Physics)
in the University of Michigan
2022

Doctoral Committee:

Professor Hui Deng, Chair
Assistant Professor Parag Deotare
Professor Çağlıyan Kurdak
Professor Vanessa Sih
Professor Kai Sun

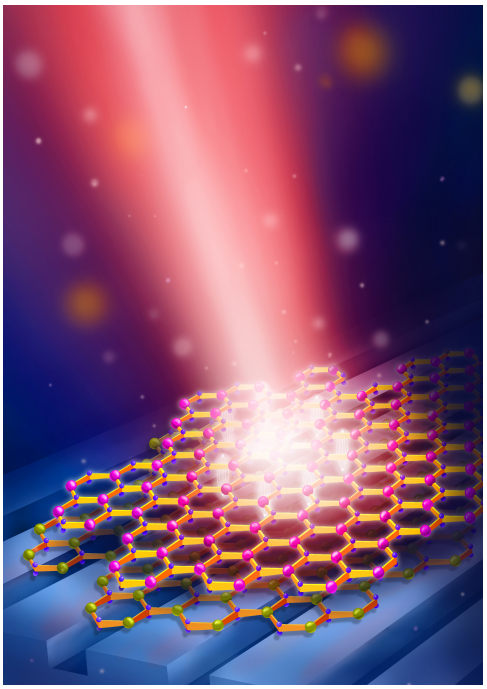

Eunice Paik
eypaik@umich.edu
ORCID iD: 0000-0002-7664-2769

For Tyler

ACKNOWLEDGMENTS

An African proverb says, “It takes a village to raise a child”. Having had a human baby while working on my thesis baby, this proverb hits closer to home. This work would not have been possible without my “village”, and I would like to express my gratitude to the people who made this journey possible.

First and foremost, my thesis would not exist without the support of my advisor, Professor Hui Deng. Her boundless patience, scientific acumen, and personal interest in her students made it easier to navigate the ups and downs of graduate school. Her door is always open, and she genuinely cares about her students as individuals, not just as researchers. I thank her for the unwavering support and understanding throughout my PhD, even when progress was slow. She taught me to be a critical thinker and the importance of effectively presenting my work. She connected me with collaborators and sought new opportunities for me. Thank you for being a great role model.

Hui also attracted some great people to her group. I thank Adam Katcher who showed me the ropes in the lab and let me tag along during his experiments. Long Zhang played a pivotal role in my research career. He is not only an excellent researcher, but also an extremely kind and patient person. He taught me everything I know about 2D materials and nanofabrication and was always willing to take the time to explain everything clearly. I think him for his mentorship. I had the pleasure of working with other Deng group alumni: Rahul Gogna, Jason Horng, Yu-Hsun (Tim) Chou, Yingyu Lai, Jiaqi Hu, Glenn Leung, Seonghoon Kim, and Zhaorong Wang. I also thank the current members of the group: Adam Alfrey, Lingxiao Zhou, Yuze Liu, Chulwon Lee, Nathan Lydick, Qiuyang Li and Xin Xie. The lab is in good hands. I would like to thank Adam Alfrey for helping me with the seemingly endless hours of lab cleaning and organizing and sample fabrication.

Special thanks to my committee members, Professors Vanessa Sih, Kai Sun, Çağlıyan Kurdak, and Parag Deotare for taking the time to review this thesis. I would also like to thank Professor Emanuel Tutuc and his students Will Burg and Yimeng Wang, for our fruitful collaboration. I thank Professor Stephen Forrest and Shaocong Hou for providing us DBR samples.

Many thanks to the friends in my cohort who helped me survive first year of graduate school and pulled me out of the dark sub-basement for coffee and chats. I am thankful

for the staff that keeps the Physics department running smoothly. I thank the LNF staff, especially Dr. Pilar Herrera-Fierro for not only helping me with sample fabrication, but also being a mentor.

The support, encouragement, and respite my family provides have been instrumental to this thesis. Catherine and Doug have always shown immense love and support for anything I do and made me part of their family. I thank them for helping us with Rowan for a month so I can write this thesis.

I would not have made it this far if it were not for my parents and brother Josh. My dad instilled in me a love for physics from a very young age and has always been willing to help me in any way he can. Without him, this thesis would not have been possible. My mom taught me the importance of learning and always knows how I am feeling before I even tell her. She is a superhero – the first few months after Rowan was born, she made food for us, took care of Rowan, gave me time to work, all while trying to get her own work done. Thanks, Josh, for always willing to hang out with me, his old older sister, even though he is much cooler than me.

One of the best things that came out of being in Hui's group was meeting Tyler. He has provided unconditional support, biking many miles to bring me dinner when I would run experiments late into the night, reminding me that I deserve to be here whenever I felt like an imposter, and always making me smile with his silly jokes. Words cannot describe how much I love the family we have created together and how much I am looking forward to our next adventures. And to my baby Rowan, you have made me happier than I ever have been before, and I thank you for being exactly who you are.

PREFACE

The projects presented in this thesis are based on Ref. [1] and Ref. [2].

The work presented in Chapter 6 was done in close collaboration with Long Zhang, who is now a professor at Xiamen University. Professor Emanuel Tutuc's group at University of Texas Austin provided the transition metal dichalcogenide (TMDC) heterobilayer sample.

Preliminary work for Chapter 5 was done by Long Zhang and Shaocong Hou, who is now a professor at Wuhan University. I took part in making the sample, performing the optical measurements, analyzing the data, and writing the manuscript.

A small portion of the writing was paraphrased from my own work in Ref. [3]. Part of the abstract and introduction was used for a Rackham fellowship application.

The image shown after the title page was drawn by Larrea Young (littleknids.com).

TABLE OF CONTENTS

LIST OF FIGURES

LIST OF TABLES

LIST OF ABBREVIATIONS

AFM atomic force microscope

ALD atomic layer deposition

AlGaAs aluminium gallium arsenide

BZ Brillouin zone

CBM conduction band minimum

CCD charge-coupled device

CMOS complementary metal-oxide semiconductor

CVD chemical vapor deposition

cw continuous wave

DBR distributed Bragg reflector

DCM dichloromethane

DFT density functional theory

EBL electron-beam lithography

EL electroluminescence

FWHM full width at half maximum

GaAs gallium arsenide

hBN hexagonal boron nitride

HWP half waveplate

IPA isopropyl alcohol

LED light-emitting diode

MBE molecular beam epitaxy

MgF_2 magnesium fluoride

MIBK methyl isobutyl ketone

MoS_2 molybdenum disulfide

$MoSe_2$ molybdenum diselenide

$MoTe_2$ molybdenum ditelluride

NA numerical aperture

PC polycarbonate

PCB print circuit board

PDMS polydimethylsiloxane

PET polyethylene terephthalate

PL photoluminescence

PMMA polymethyl methacrylate

PPC polypropylene carbonate

QED quantum electrodynamics

RCWA rigorous coupled wave analysis

RIE reactive-ion etching

SEM scanning electron microscope

SHG second harmonic generation

Si silicon

SiN silicon nitride

SiO_2 silicon dioxide

TiO_2 titanium dioxide

TMDC transition metal dichalcogenide

VBM valence band maximum

vdW van der Waals

VTE vacuum thermal evaporation

WS_2 tungsten disulfide

WSe_2 tungsten diselenide

ZnS zinc sulfide

1D one-dimensional

2D two-dimensional

3D three-dimensional

ABSTRACT

Semiconductor photonic devices enable efficient optical communication using light for fast transmission and detection of information. Conventional photonic devices primarily use group III-V semiconductors. However, these devices have limited integrability with silicon-based circuits, are bulky, and it is challenging to engineer their fundamental properties. Van der Waals (vdW) semiconductors are good candidates for the next generation of devices because they are atomically thin and feature strong emission, making them easy to integrate and efficient. Furthermore, they enable engineering of optical, electrical, and structural properties through formation of heterostructures and moiré superlattices.

We design and create novel photonic devices by leveraging the optical tunability of vdW semiconductors. Our transferrable distributed Bragg reflector (DBR) cavity has a high quality factor, can strongly couple with vdW materials, and constructed using cavity fabrication methods that are robust and reliable. The DBR cavity coupled with hexagonal boron nitride (hBN) encapsulated monolayer $MoSe_2$ forms strongly coupled exciton-polaritons.

To further study photonic devices with vdW heterobilayers, we design and create the first WSe_2/$MoSe_2$ heterostructure laser and perform rigorous power dependence and first-order spatial coherence measurements to ensure lasing. The device shows a non-linear increase of the output intensity, linewidth narrowing, and a formation of extended spatial coherence, signifying lasing. Lastly, we study electrically controlled and cavity coupled WS_2/$MoSe_2$ hybrid excitons to better understand the exciton-cavity coupling mechanism. Together, this improved understanding of vdW cavities and heterostructures sets the stage for designable photonic technologies and allows exploration of novel physics.

CHAPTER 1

Introduction

One shouldn't work on semiconductors, that is a filthy mess;
who knows if they really exist? –Wolfgang Pauli, 1931

Semiconductor photonic devices utilize the interaction of light and matter to store and transmit information. They form the bedrock of modern optical telecommunications and sensing technologies. Current photonics rely on group III-V 3D semiconductors, such as gallium arsenide (GaAs), which have limited choice of substrates and lack tunability. The emergence of van der Waals (vdW) two-dimensional (2D) semiconducting materials provides an unprecedented opportunity for the next generation of photonic devices that are more compact, tunable, versatile for integration, and more energy efficient compared to the existing technology. This thesis focuses on designable 2D material photonics that are customizable in their optical, electronic, and structural properties, in both strong and weak light-matter coupling regimes.

1.1 Semiconductor photonics: brief history and context

A world without semiconductors is difficult to fathom. At the time of this writing, there is an ongoing global semiconductor chip shortage, which impacts an abundance of digital products including cars, computers, cell phones, cameras, and even washing machines, therefore opening our eyes on how intertwined semiconductors are into our daily lives. The earliest measurements of semiconductors date back to the 18th century. Through decades of research and the invention of transistors in the 1920s that revolutionized electronics, the semiconductor industry maintains a firm standing in the scientific community [15].

An important property of semiconductors is their ability to emit light. Light is faster than electrons, so naturally it is optimal for efficient storage and transmission of information. The light-emitting property of semiconductors can be harnessed to develop photonic

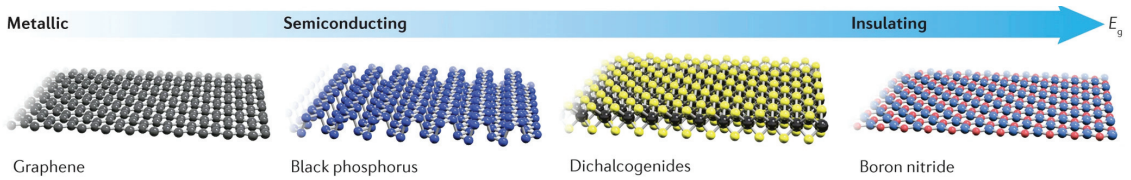

Figure 1.1: Types of 2D materials. Reproduced with permission from [4].

devices, such as lasers and light-emitting diode (LED)s, that serve as key components to many electronic and communication devices. Despite the success of these devices, there is an ever-increasing demand for more energy efficient and compact photonics that could satiate the need for higher computing power and better performance. A way of accomplishing this is to confine light into a smaller regions using microcavities and finding new semiconductor materials that are smaller in size.

2D monolayer semiconductor materials are single atomic layer thick, have strong light emission, and have tunable properties that allow additional degrees of freedom. Naturally, there is widespread effort to make photonic devices with 2D materials for the next generation of semiconductor technology.

1.2 Two-dimensional materials

Van der Waals 2D materials are layered atomic sheets bound by vdW forces, and encompasses metals, semiconductors, and insulators (Figure 1.1). Geim and Novoselov's Nobel prize winning work pioneered the field of 2D materials by isolating a single layer of graphene using scotch tape [16]. TMDCs are a class of 2D materials which have an indirect bandgap (like silicon) in bulk form but become direct bandgap (like GaAs) in the monolayer limit. Unlike conventional 3D semiconductors, TMDCs have a reduced dimensionality, which enables exceptionally strong interactions with light and integration with a wide range of substrates. TMDC heterostructures can be constructed by stacking different combinations of TMDCs, much like stacking Lego bricks, allowing customizable optical, electrical, and structural properties while retaining the benefits of monolayer TMDCs. For instance, the optical properties can be engineered by changing the specific combination of TMDCs used to form heterostructures. Furthermore, the ability to manipulate the electronic band structures by changing the twist-angle between layers opens up possibilities of studying strongly correlated physics. These unique optical and structural properties prompted active research of TMDCs for photonics and optoelectronic applications [17].

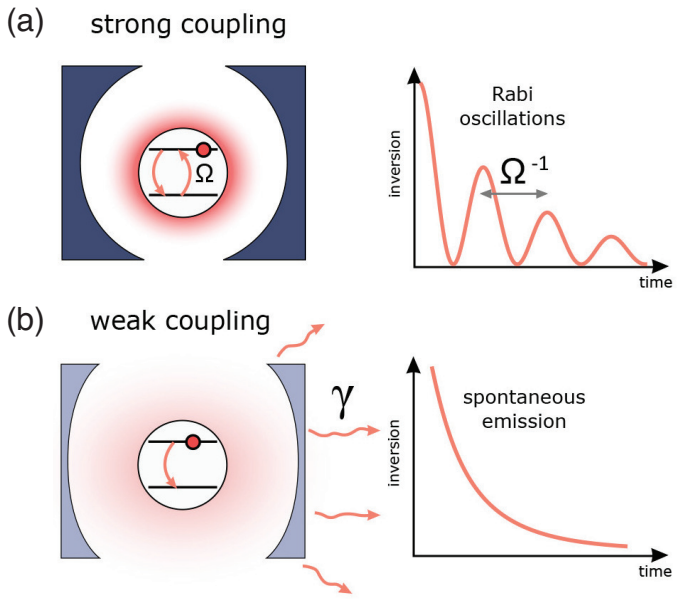

Figure 1.2: Strong coupling versus weak coupling. (a) Schematic illustration of strong coupling. Ω is the exciton-photon coupling constant. (b) Schematic illustration of weak coupling. γ is the spontaneous decay rate. Reproduced with permission from [5].

1.3 Light matter interactions for photonics

When carriers (electrons and holes) in TMDCs are excited by a laser, they form excitons, which are electron hole pairs bound by coulomb forces. Excitons can recombine to emit light. The binding energy is related to the intensity of light-matter interaction, characterized by the oscillator strength. Large oscillator strength equals high emission intensity, which is crucial for photonic devices.

In monolayers, the excitons are confined in the in-plane direction and are referred to as intralayer excitons. Intralayer excitons have a large binding energy that is an order of magnitude greater than that of GaAs. Therefore, the monolayer exciton emission can persist at room temperature and can strongly interact with light.

In heterobilayers, electrons and holes can be spatially separated into different layers, resulting in interlayer excitons. Interlayer excitons have smaller oscillator strength compared to intralayer excitons and thus weakly interact with light. Nevertheless, interlayer excitons have long lifetimes and a strong dipole-dipole interaction strength, which could facilitate collective many-body phenomena such as exciton condensation and superfluidity [18, 19]. In addition, moiré superlattices in heterostructures provides additional tunability of the excitonic band structures and the out-of-plane dipole moment of interlayer excitons allows easy electrical tuning of exciton properties and electrical injection of carriers [20, 21, 22].

Photonic cavities provide a method of controlling and enhancing the interactions be-

tween excitons and photons in TMDCs. The exciton-photon interaction strength determines two distinct regimes of light-matter coupling: strong coupling and weak coupling. In the strong coupling regime, the exciton and the cavity photon energy exchange rate (the coupling strength) is greater than the decay rates of the system and results in a reversible spontaneous emission rate and a formation of new hybridized eigenmodes called exciton-polaritons (Figure 1.2(a)). Exciton-polaritons are a unique platform for observing many-body phenomena and developing ultra-low threshold semiconductor lasers. Intralayer TMDC excitons are ideal for studying exciton-polaritons due to their strong oscillator strength.

In the weak coupling regime, the decay rate is greater than the energy exchange rate and the spontaneous emission rate is irreversible and enhanced by the cavity (Figure 1.2(b)). This can result in conventional photon lasing. Interlayer TMDC excitons have smaller oscillator strength and therefore couple weakly with the cavity photons and provide a platform for studying photon lasing.

1.4 Goals of this thesis

The goal of this thesis is to use cavity structures to control the exciton light-matter interactions in TMDCs. In particular we:

- Demonstrate a new type of cavity that can strongly couple with TMDCs and perform systematic studies on the controllability and reliability of the cavity parameters.
- Fabricate and characterize a novel semiconductor photon laser using a TMDC heterobilayer.
- Study the optical properties of different TMDC exciton species and how to control them.

1.5 Thesis outline

This thesis demonstrates novel semiconductor photonic devices using 2D materials by engineering and measuring the optical, electrical, and structural properties of TMDCs and designing and fabricating new cavity structures. Chapter 2 presents the theoretical background of monolayer and heterobilayer excitons in TMDCs and introduces ways of controlling them. Chapter 3 introduces semiconductor microcavities and presents the theory of

light-matter coupling in the strong and weak coupling regimes. Chapter 4 lists the experimental methods used for fabrication and measurement of devices. This includes sample preparation, optical spectroscopy, and electrical device preparation methods. Chapter 5 discusses results on a new type of TMDC exciton-polariton device that utilizes an original, high quality cavity structure. Chapter 6 discusses photon lasing in TMDC heterobilayers and the optical measurement results used to verify lasing. Chapter 7 introduces methods of controlling the electrical and structural properties of TMDCs. Lastly, chapter 8 discusses the conclusion and outlook.

CHAPTER 2

Excitons in TMDCs

An exciton is an electron-hole quasi-particle that is an elementary unit of optical excitation in solids. It serves as the basis of light-matter interactions in semiconductor materials. Semiconductors have a valence band filled with electrons and an empty conduction band. When the electron in the valence band is excited to the conduction band by an external source, it leaves behind a positively charged hole. The electron and hole are bound by Coulomb interaction forces and form an energetically favorable quasi-particle called excitons. The exciton electron-hole pair forms a dipole moment that interacts with the electromagnetic field of light and therefore serves as an essential component of photonic devices. In this chapter, we will discuss the physics behind excitons in TMDCs. Section 2.1 presents the theory of excitons in monolayer TMDCs. Section 2.2 discusses interlayer excitons in TMDC heterobilayers. Section 2.3 introduces ways of controlling excitons in TMDCs.

2.1 Excitons in monolayer TMDCs

Unlike multilayers, monolayers are optically accessible because they have a direct band gap. Excitons in monolayers feature a strong binding energy, large oscillator strength, and momentum valley physics. This makes monolayer excitons (also known as intralayer excitons) a fundamental component of studying light-matter interactions in TMDCs. In this section, we explore the crystal and band structures of monolayer TMDCs and discuss the theory behind monolayer excitons.

2.1.1 Crystal structure of monolayer TMDCs

The class of 2D material encompasses a wide range of materials including insulators, semiconductors, and semimetals. The burgeoning field of 2D materials has been revolutionized by the discovery of graphene exfoliation in 2004 [16]. This discovery has propelled and

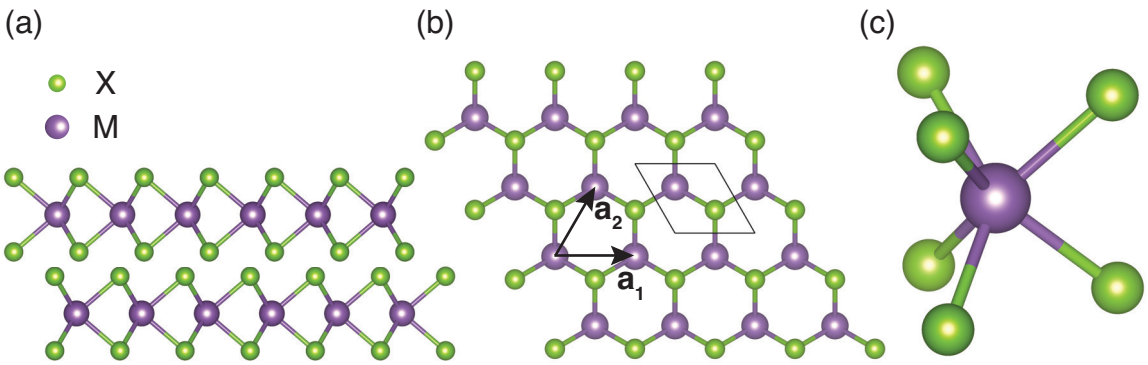

Figure 2.1: Crystal structure of TMDCs. (a) Side view of two TMDC layers showing a 2H stacking structure. (b) Top view of the hexagonal crystal lattice structure. $\vec{a}_1$ and $\vec{a}_2$ indicate the Bravais lattice vectors and the polygon shape outlines the unit cell. (c) Unit cell of MX_2 with a trigonal prismatic geometry. Drawings created using VESTA.

expanded the research on 2D materials and continues to attract research interest. Out of the 2D materials, we focus our attention on the semiconducting TMDCs, particularly the ones that have the chemical name in the format of MX_2, where M represents a transition metal atom such as molybdenum (Mo) and tungsten (W), and X represents a chalcogen atom such as sulfur (S) and selenium (Se). These materials have been known for many decades [23, 24], but the study on monolayer TMDCs have only been made possible since the discovery of mechanical exfoliation methods.

Bulk TMDC crystals are composed of atomically thin layers of materials that are bound together by vdW forces. Because vdW forces are weak in comparison to the covalent bonds between atoms, the layers of material can be peeled off down to a single layer. This process is called exfoliation. The bulk crystal has a 2H stacking order, with each layer rotated by 180 degrees with respect to the neighboring layers, as shown in Figure 2.1(a).

A single layer of TMDC material is about 6 – 7 Å thick and has a hexagonal lattice structure in the in-plane direction, with alternating transition metal and chalcogen atoms occupying each lattice site as depicted in Figure 2.1(b). This alternating occupation of atoms breaks the inversion symmetry, which has important consequences for the electronic and optical properties. The unit cell of MX_2 has a trigonal prismatic molecular geometry, with the transition metal as the central atom, and six chalcogen atoms arranged at the vertices of the triangular prism (Figure 2.1(c)). The Bravais lattice is spanned by basis vectors:

$$\vec{a}_1 = (a, 0, 0), \quad \vec{a}_2 = \frac{a}{2}(1, \sqrt{3}, 0), \tag{2.1}$$

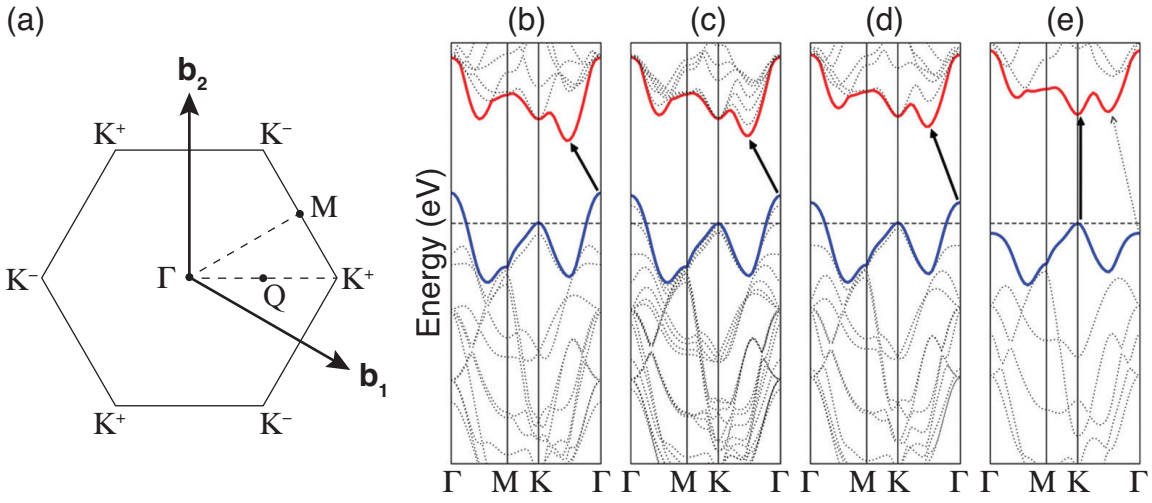

Figure 2.2: Electronic band structure of TMDCs. (a) Hexagonal BZ reciprocal lattice structure. $\vec{b}_1$ and $\vec{b}_2$ are reciprocal lattice basis vectors, and Γ, M, $K^{\pm}$, Q are symmetry points. (b-e) Electronic band structures of (b) bulk, (c) quadrilayer, (d) bilayer, and (e) monolayer MoS_2 calculated using DFT. The solid arrows indicate the lowest energy transition. Reproduced with permission from [6].

and the reciprocal lattice has the basis vectors:

$$\vec{b}_1 = \frac{4\pi}{\sqrt{3}a}\left(\frac{\sqrt{3}}{2}, -\frac{1}{2}, 0\right), \quad \vec{b}_2 = \frac{4\pi}{\sqrt{3}a}(0, 1, 0) \tag{2.2}$$

[25].

2.1.2 Band structure of monolayer TMDCs

In solid state physics, a single free electron in a periodic lattice structure can be represented by Bloch waves, and the periodic modulation of the potential opens gaps in the energy band structure. The local extrema in the band structure are called 'valleys'. The crystal structure of TMDCs result in a hexagonal BZ in reciprocal space with valleys at the K^+ and K^- points as depicted in Figure 2.2(a).

TMDCs have a direct band gap at the K^+ and K^- points in the monolayer limit. To explain this, we can consider the electronic band structure of bulk TMDCs. The direct band gap in monolayers occurs at the K point while the indirect band gap in multilayers occurs at the Γ point. The out-of-plane mass for electrons and holes at the K point exceeds the free electron mass, while at the Γ point it is a fraction the free electron mass [26]. Therefore, reducing the layer number results in increased quantum confinement, which causes an increase in the indirect band gap, while the direct band gap remains the same. Comparing the

monolayer TMDC band structure to that of graphene, graphene has a linear Dirac cone dispersion with a closed band gap, while monolayer TMDCs have a parabolic dispersion with an open band gap. This difference is due to the broken sub-lattice symmetry in TMDCs as compared to graphene, which results from the alternating occupation of lattice sites by transition metal and dichalcogenide atoms [27]. DFT calculations show the band structure of the TMDC monolayers in more detail. Figures 2.2(b-e) are DFT calculated band structures of multilayers and monolayer MoS_2, which show the lowest energy valence-to-conduction band transition to be indirect in multilayers and direct in monolayers.

2.1.3 Monolayer exciton physics

The discussion on band structures and band gap in the previous section assumes that electrons and holes behave like free carriers. However, the carriers could experience a variety of forces from their environment. In this section, we discuss the physics behind excitons, which are electron-hole pairs bound by coulomb interaction forces. Specifically, we discuss the binding energy, oscillator strength, and valley selection rules of monolayer TMDC excitons.

2.1.3.1 Basics of excitons and trions

A semiconductor at absolute zero temperature has a valence band filled with electrons and an empty conduction band. At finite temperatures, there is a probability of holes occupying the valence band and electrons occupying the conduction band, which is determined by the carrier density of states and the Fermi-Dirac distribution function. External sources, such as electromagnetic waves or electric fields, can further excite electrons into the conduction band, leaving a hole in the valence band. The electrons and holes can form a bound quasiparticle called excitons (Figure 2.3(a)), which is analogous to a hydrogen atom, where an electron is bound to a proton. Unlike hydrogen atoms however, excitons in semiconductors (also known as Wannier excitons) have a larger Bohr radius spanning multiple lattice sites, and a smaller binding energy. This is due to the small effective mass of electrons compared to that of holes and the presence of dielectric screening in semiconductors. Excitons can recombine to emit light and thus are a key component in studying light-matter interaction in TMDCs. Some of the beneficial properties of excitons will be discussed further in the following sections.

The interaction of electron and holes has important consequences for optical and electronic properties in the material. The free particle band gap is determined by the Bloch wave approximation and corresponds to the energy in which the electrons and holes are in

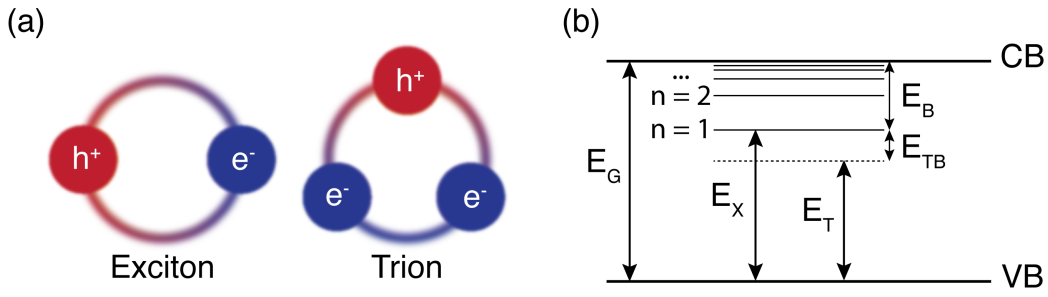

Figure 2.3: Excitons and trions in monolayer TMDCs. (a) Schematic drawing of an exciton and a negatively charged trion. (b) Simplified energy diagram of the conduction band (CB), valence band (VB), monolayer band gap (E_G), exciton energy (E_X), trion energy (E_T), exciton binding energy (E_B), and trion binding energy (E_{TB}).

a continuum state. Compared to the free particle band gap (E_G), exciton energy (E_X) is lower because it is a bound state. The exciton binding energy (E_B) is defined as the energy required to disassociate the electrons from the holes, and can be used to express the exciton energy:

$$E_X = E_G - E_B. \tag{2.3}$$

The exciton energy is also referred to as the optical band gap. The optical band gap is the lowest-energy state ($n = 1$) of the exciton. The energy diagram of the exciton energies are drawn in Figure 2.3(b).

Commonly in monolayer TMDCs, an additional electron or hole can bind to the exciton and form trions with energy (E_T) lower than the exciton energy (Figure 2.3(b)). In traditional 3D semiconductors, trion binding energy is small ($\approx 1-2$ meV) [28]. In comparison, the trion binding energy (E_{TB}) in TMDCs is about 30 meV, allowing emission even up to room temperature [29, 30]. Trions also have strong emission and are gate tunable, making them an interesting component of studying light-matter interactions and many-body physics in TMDCs [31, 32, 33]. For purposes of this thesis however, we focus on the charge neutral excitons.

Due to the 2D nature of TMDCs, the exciton binding energy is large, which has important implications for light emission. We investigate the details of binding energy and light emission in the upcoming sections.

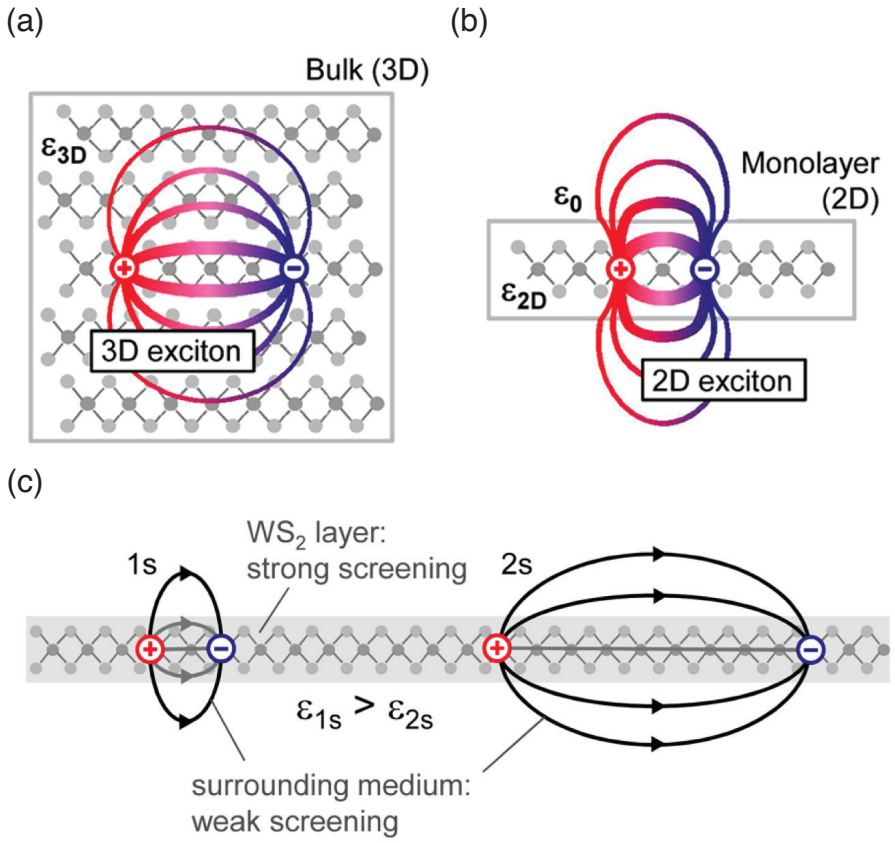

Figure 2.4: Dielectric screening of excitons in monolayers. (a-b) Schematic drawing of the exciton dielectric screening in (a) 3D and (b) 2D. (c) Schematic drawing of 1s and 2s excitons in non-uniform dielectric environment. Reproduced with permission from [7].

2.1.3.2 Binding energy

Excitons in monolayer TMDCs have binding energies on the order of 500 meV [34], orders of magnitude greater than that of traditional 3D semiconductors, such as GaAs. This is due to the decrease in dimensionality going from 3D to 2D that results in a smaller electron-hole separation, smaller electron and hole effective masses, and reduced dielectric screening. A schematic drawing of the dielectric screening in 3D versus 2D is shown in Figure 2.4(a), 2.4(b). The monolayer exciton binding energy is larger than the room temperature thermal energy ($\approx$ 25 meV), which makes monolayer excitons stable at room temperature, allowing room temperature photonic and optoelectronic devices.

To calculate the exciton binding energy, we start from the Wannier equation, which is a two-particle Schödinger equation that describes an electron in the conduction band and a hole in the valence band interacting via an attractive Coulomb potential [35]:

$$-\left[\frac{\hbar^2\nabla^2}{2\mu}+V(r)\right]\psi_\nu(r)=E_\nu\psi_\nu(r). \tag{2.4}$$

μ is the reduced mass of the exciton:

$$\mu=\frac{m_e m_h}{m_e+m_h}, \tag{2.5}$$

where m_e is the electron effective mass and m_h is the hole effective mass. $V(r)$ is the Coulomb potential:

$$V(r)=\frac{e^2}{4\pi\epsilon_r\epsilon_0 r}, \tag{2.6}$$

where e is the elementary charge, ϵ_r is the relative permittivity, and ϵ_0 is the vacuum permittivity. The Wannier equation is analogous to the Schrödinger equation for an hydrogen atom. Solving the Wannier equation in 2D (using the 2D Laplace operator in polar coordinates) we obtain the eigen-energy:

$$E_B^n=\frac{\mu e^4}{2\hbar^2\epsilon_{\text{eff}}^2\left(n-1/2\right)^2},\ \text{with } n=1,2,3,\cdots, \tag{2.7}$$

where ϵ_{eff} is the effective dielectric screening from the environment. Experimental measurements and theoretical studies of 2D excitons in monolayer TMDCs have shown deviation from this simplified model [36, 7, 37, 38]. This is due to the nonuniform dielectric environment experienced by the exciton in 2D materials [39]. Qualitatively, this is due to the different levels of dielectric screening experienced by the electric field lines between electrons and holes. The electric field lines experience a larger screening when

going through the 2D material than when going through the surrounding medium as shown in Figure 2.4(c). For higher order excitons (higher quantum number n), the separation between electron and hole becomes larger, fewer electric field lines go through the 2D material, and thus the screening is reduced. This can be modeled as the Rytova-Keldysh potential [40, 41]:

$$V_{eh}(r) = -\frac{\pi e^2}{2r_0}\left[H_0\left(\frac{r}{r_0}\right) - Y_0\left(\frac{r}{r_0}\right)\right], \tag{2.8}$$

where H_0 and Y_0 are Struve and Bessel functions and r_0 is the effective screening length.

Because of the 2D nature of monolayer TMDCs, the substrate or capping material can increase the dielectric screening and reduce the exciton binding energy. However, the additional dielectric screening also renormalizes and reduces the free particle band gap [42]. This combined with the reduced binding energy results in minimal changes to the exciton ground state energy.

The strong binding energy of monolayer TMDC excitons offer benefits for the study of light-matter interactions. First, the large binding energy results in room-temperature stable excitons. Next, the higher order exciton states ($n = 2, 3, \cdots$) are experimentally observable [7] and have been used to demonstrate exciton-polaritons with higher interaction strength [43]. Lastly, the excitons interact strongly with light, which we will discuss further in the next section.

2.1.3.3 Oscillator strength and linewidth

The strong binding energy of TMDC excitons leads to a small spatial separation of electrons and holes and thus a larger wave function overlap. As a result, the excitons have a large oscillator strength and interact strongly with light. The exciton oscillator strength is a dimensionless quantity that quantifies the interaction between the exciton and electromagnetic waves. It can be derived from the inter-band optical transition matrix and is defined as follows [14]:

$$f = \frac{2\mu\omega}{\hbar}\left|\langle u_v|\boldsymbol{r}\cdot\boldsymbol{e}|u_c\rangle\right|^2 \frac{V}{\pi a_{B,2D}^3}, \tag{2.9}$$

where u_c and u_v are Bloch wave functions of electron and hole, respectively, ω is the frequency of the transition, V is the exciton quantization volume, and $a_{B,2D}$ is the Bohr radius in 2D. To determine the Bohr radius in 2D, we first consider the general form of the exciton radius in 3D:

$$r_{X,3D} = n a_{B,3D}, \text{ with } n = 1, 2, 3, \cdots. \tag{2.10}$$

Here, $a_{B,3D}$ is the exciton Bohr radius in 3D. It turns out, going from 3D to 2D, the n quantum number goes from $n \rightarrow (n - 1/2)$ [35, 44, 45]. This change manifests itself during the change of coordinates from spherical (3D) to polar (2D). The detailed analytical derivation can be found in Ref [46]. The Bohr radius in 2D (where $n = 1$) is therefore:

$$a_{B,2D} = \frac{1}{2} a_{B,3D} = \frac{\epsilon_r \epsilon_0 \hbar^2}{2\mu e^2}. \tag{2.11}$$

Hence, in 2D the exciton binding energy is 4 times larger and the Bohr radius is 2 times smaller than in 3D. Using a simplified picture, this is due the the exciton being confined to a 2D plane and being 'squeezed' together. In TMDCs, the exciton Bohr radius for the 1s state is on the order of 1 nm [47].

Excitons that are optically active can recombine to emit light. The radiative decay rate of excitons can be described by Fermi's golden rule [48]:

$$\Gamma_0 \sim |\langle f|\boldsymbol{e}\cdot\boldsymbol{r}|i\rangle|^2 \, \rho_{c,v}(\omega) \, \delta(E_c - E_v - \hbar\omega), \tag{2.12}$$

where f and i are final and initial states, $\rho_{c,v}(\omega)$ is the density of states, E_c and E_v are final and initial state energies, respectively, and $\hbar\omega$ is the energy of the electromagnetic field. In order for exciton radiative decay to occur, the exciton center-of-mass wave vector $\boldsymbol{k}$ must be equal to the in-plane projection of the photon wave vector $\boldsymbol{q}_{\parallel}$ [34]. Thus, the allowed wave vectors are $k < q_0 = \omega/c$, where ω is the photon frequency corresponding to the exciton resonance. In other words, the excitons that are within the "light cone" (also known as bright excitons) couple to light by absorption or emission, while excitons outside of the light cone (dark excitons) are optically inactive. A schematic illustration of dark and bright exciton formation is shown in Figure 2.5.

In monolayer TMDCs, there are both bright and dark excitons. The optical transition between the same spin states in the valence and conduction bands results in the formation of two bright excitons called the A exciton (lower energy) and the B exciton (higher energy) as represented in Figure 2.5(b). Furthermore, the dark exciton is the lowest energy state in tungsten-based TMDCs, namely WS_2 and WSe_2 [49]. Consequently, the dark states reduces the emission of WS_2 and WSe_2 at low temperature [50].

The exciton linewidth gives some information about the dynamics of the excited state population and how it interacts with light. Theoretical studies predict the radiative lifetime of 1s excitons in TMDCs to be on the order of 1 ps, which corresponds to a radiative linewidth of 1 meV [51, 52], about two orders of magnitude smaller than that of GaAs [53]. The radiative lifetime sets a lower bound for the linewidth. In real systems, there are de-

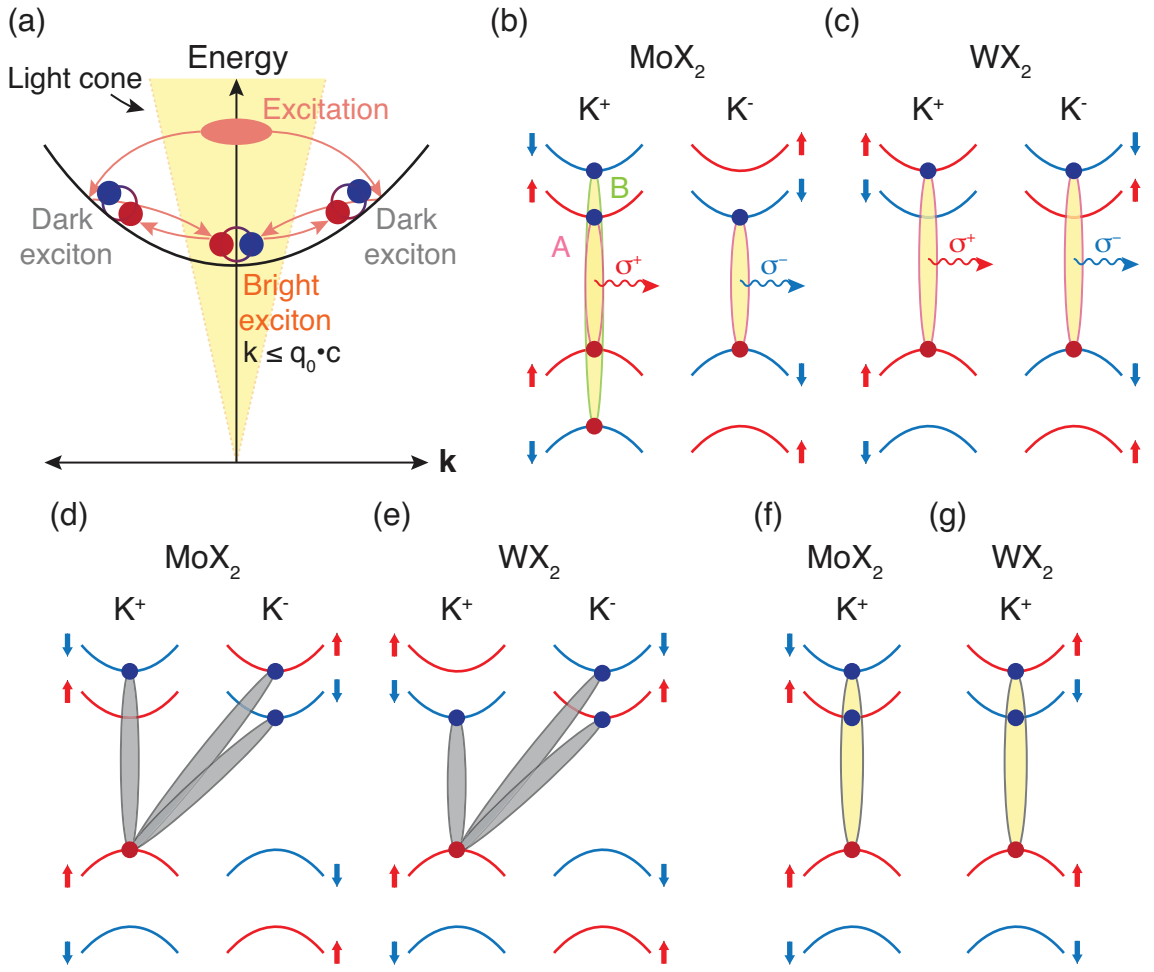

Figure 2.5: Exciton formation and emission. (a) Schematic diagram of the exciton formation dynamics in the two-particle representation. The light cone is colored in yellow. Excitons inside of the light cone are bright excitons and excitons outside of the light cone are dark excitons. Excitons are created by excitation of carriers and subsequent relaxation to the ground state. Dark excitons can scatter into the light cone via phonon scattering and at finite temperatures bright excitons can scatter outside of the light cone. (b-c) Spin-valley band configurations and optical transitions for bright excitons in (b) Molybdenum-based, and (c) Tungsten-based monolayers. A and B represent the A-exciton and B-exciton transitions, respectively. Spin up and spin down states are represented in red and blue, respectively. (d-e) Dark exciton formation in (d) Molybdenum-based and (e) Tungsten-based monolayers. (f-g) Inter-valley bright trion formation for (f) Molybdenum-based and (g) Tungsten-based monolayers.

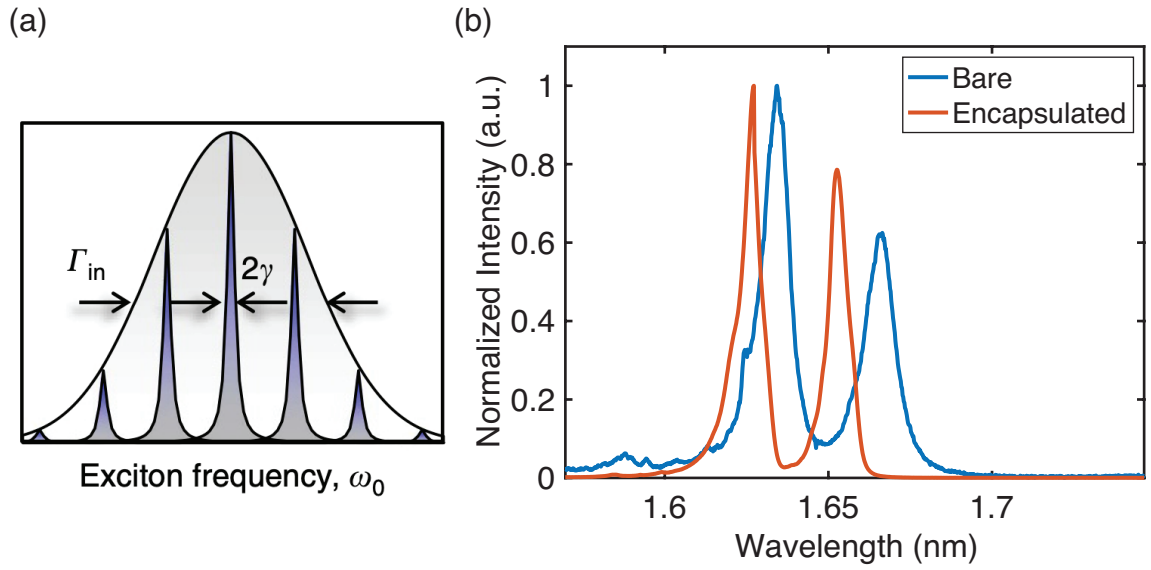

Figure 2.6: Exciton linewidth in TMDCs. (a) Schematic representation of inhomogeneous linewidth broadening. Individual oscillators with linewidth 2γ have different frequencies due to the environmental variations. This results in an inhomogeneously broadened total linewidth (Γ_{in}). Figure reproduced with permission from [8]. (b) Photoluminescence measurements of bare and encapsulated monolayer $MoSe_2$ at 5K.

fects, inhomogeneity, and impurities that shift the exciton resonance and therefore inhomogeneously broaden the linewidth (Figure 2.6(a)). Therefore, special experimental techniques, such as 2D Fourier transform spectroscopy [8, 54], mid-infrared absorption spectroscopy [55], and high-resolution time-resolved spectroscopy [56] are required to extract the radiative lifetime.

Decreasing the exciton linewidth is important for thermalization of excitons and exciton-polaritons. In TMDCs, the best way to reduce the linewidth is by encapsulating the monolayer with hBN [57, 58, 59]. Capping the monolayers with hBN can ensure the surface roughness of the substrate does not transfer to the monolayer, and can also protect the exciton from charge transfers or local electric fields, thus reducing the inhomogeneous broadening of the linewidth. Experimental studies show that hBN encapsulation results in linewidths as low as 2 meV [57]. Encapsulation also alters the dielectric environment experienced by the excitons and trions and can change their energies (Figure 2.6(b)).

An important aspect of light emission from bright excitons is the optical selection rules that determine the allowed inter-band transitions. Valley-dependent optical selections rules are a unique property of monolayer TMDCs and will be introduced in the following section.

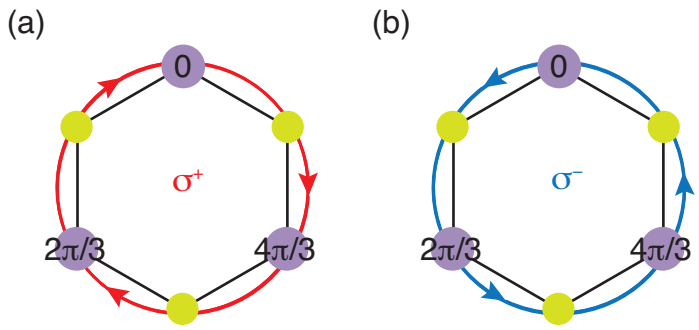

Figure 2.7: Valley-contrasting Berry curvature. Opposite valley curvature in (a) K^+ and (b) K^- valleys results in opposite helicity of circularly polarized light coupled to each valley.

2.1.3.4 Valley selection rules

A unique property that monolayer TMDCs have over other conventional semiconductors is their spin-valley properties and valley-dependent optical selection rules. As discussed in section 2.1.1, the monolayer unit cell has a trigonal prismatic crystal structure, and the inversion symmetry is broken. In other words, if we take the transition metal as the inversion center and perform the space-inversion transformation, the chalcogen atoms will be mapped to an empty lattice site. This broken symmetry results in changes in the band structure property, namely the large spin-orbit coupling and the valley-contrasting Berry phase.

The valence and conduction bands at the K^+ and K^- valleys are partially composed of d atomic orbitals. Due to the broken inversion symmetry, the energy bands develop a spin-splitting, and because of the heavy transition metal d orbitals (compared to that of carbon atoms) the spin-orbit coupling is strong compared to that of graphene [60, 61]. The spin-orbit splitting in the valence band is around 200 meV in Mo-based TMDCs, and 400 meV in W-based TMDCs. The splitting in the conduction band is smaller, a few tens of meV [62].

Another consequence of the broken inversion symmetry is to the Berry phase. Berry showed that when an eigenstate slowly moves in a closed loop through a vector field, the eigenstate will return to the initial state but will acquire a phase [63, 64]. The acquired phase is called the Berry phase, and the curl of the vector field is called the Berry curvature. In the context of monolayer semiconductors, the K^+ and K^- valleys have opposite signs of Berry curvature. When Bloch electrons move in a closed loop around the K^+ and K^- valley band extrema, they acquire a Berry phase that is equal and opposite between the valleys [61, 65]. Schematic drawing of the Berry curvature for each valley is shown in Figure 2.7. The Berry curvature results in a valley orbital magnetic momentum and therefore an opposite

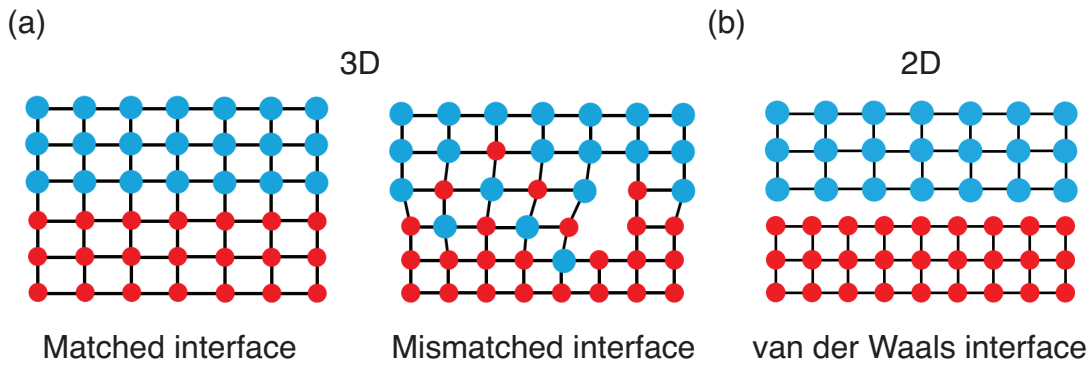

Figure 2.8: Heterostructure lattice matching. (a) Schematic drawing of a 3D lattice matched (left) and lattice mismatched (right) heterostructure interface. The lattice mismatch induces strain and defects along the boundary. (b) 2D heterostructure interface. The layers are bound together by vdW forces. Reproduced with permission from [9].

helicity of circularly polarized light that couples to the K^+ (σ^+ polarization) and K^- (σ^- polarization) valleys (Figure 2.5(b) and 2.5(c)).

These valley properties can give rise to interesting phenomena, such as valley Zeeman and Hall effects [66], and can provide an extra degree of freedom for applications in Quantum information storage and processing.

2.2 Interlayer excitons in TMDC heterobilayers

A beneficial property of TMDCs is the ability to form heterostructures without lattice matching constraints. Unlike 3D materials, 2D materials do not have dangling bonds, which means they can be integrated with other materials without inducing strain or defects at the boundary (Figure 2.8). Furthermore, there is a wide variety of 2D materials with different band gaps and work functions that can be used for heterostructure engineering, allowing a greater degree of flexibility than 3D bulk semiconductors.

When two different semiconductor materials are combined to form a heterostructure, an electron in one layer and a hole in another can be bound to form an interlayer exciton. The electron and hole wave functions in interlayer excitons are spatially separated, whereas in intralayer excitons they are closer together. Therefore, interlayer excitons are also known as spatially indirect excitons, and they have been first reported in GaAs/aluminium gallium arsenide (AlGaAs) coupled quantum wells to use as electro-optical modulators [67]. The spatial separation of electron and holes result in a long radiative lifetime, a strong dipole-dipole interaction strength, and a permanent out-of-plane dipole moment. In 2D materials, interlayer excitons in both homo- and heterobilayers feature a strong binding energy compared

to 3D semiconductors, making them useful for high-temperature applications. Spatially indirect excitons can exhibit a variety of physical phenomena including quantum-confined Stark effect [68, 69, 70, 71], exciton condensation and superfluidity [72, 73, 74, 18, 75, 76], and strongly-correlated electronic states [77, 78, 79].

Interlayer excitons have been demonstrated in a wide range of TMDCs materials, including $MoSe_2$ [80], WSe_2 [71], and MoS_2 [81] homobilayers, and $MoSe_2/WSe_2$ [82, 83, 22, 84, 85, 86], MoS_2/WS_2 [87, 88], MoS_2/WSe_2 [89, 90], and WS_2/WSe_2 [91] heterobilayers. For this thesis, we focus on the heterobilayers, mainly $MoSe_2/WSe_2$ and $MoSe_2/WS_2$.

In this section, we discuss the band structure of heterobilayers, the theory of interlayer excitons, and optical selection rules.

2.2.1 Band structure of TMDC heterobilayers

When two different semiconductors are combined to form a heterostructure, the relative band alignment between the layers is an important factor in determining the physical properties of the heterostructure devices. There are three different types of band alignments. Type I is straddling, type II is staggered, and type III is broken [92] (Figure 2.9(a-c)). Band alignment of TMDC heterostructures is overwhelmingly type II, with some type I. This is determined by the relative band structures of the currently available TMDC materials as shown in Figure 2.9(d). Type II band alignment is when the conduction band minimum and the valence band maximum are in different layers so that electrons are localized in one layer and holes are localized in the other. The coulomb interaction between the electrons and holes in the two layers results in the formation of spatially indirect, interlayer excitons. Schematic drawing of interlayer exciton formation is shown in Figure 2.10(a). The energy of the interlayer exciton depends on the interlayer bandgap, which is smaller than the individual bandgaps of the monolayers. The binding energy of interlayer excitons in $WSe_2/MoSe_2$ is around 150 meV, which is smaller than that of intralayer excitons, due to the spatial separation of electron and holes [93]. A simplified energy diagram of the $WSe_2/MoSe_2$ is shown in Figure 2.10(b). The type II band alignment in TMDC heterostructures can be experimentally confirmed by using sub-micrometer angle-resolved photoemission spectroscopy (μ-ARPES) [11].

For optical studies, it is important to ensure that interlayer excitons have a direct band gap. However, the coupling between the two layers can affect the band structure of the heterobilayer [94]. Therefore, we must ensure that the conduction band minimum (CBM) and the valence band maximum (VBM) remain in the K^+ and K^- valleys. Interlayer hybridization occurs when the interlayer hopping is comparable to the band offsets and causes the

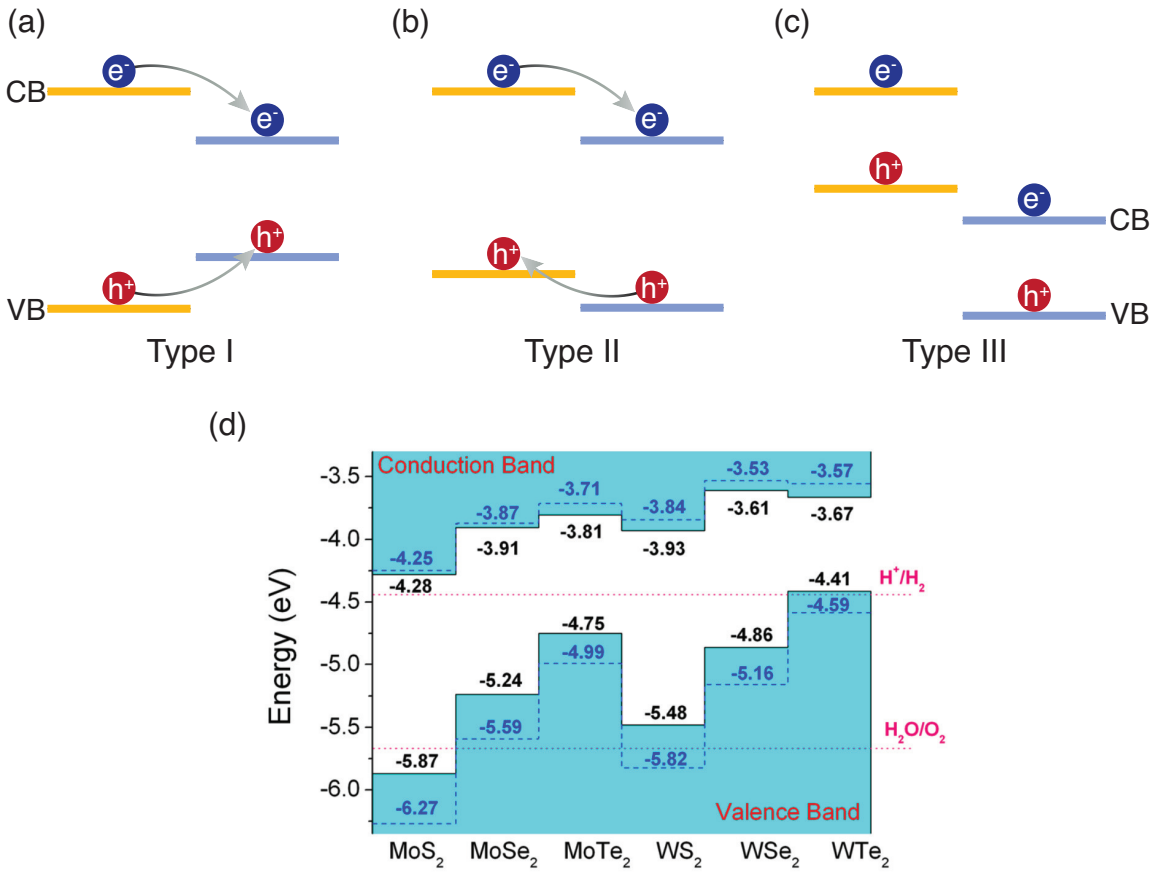

Figure 2.9: Heterostructure band alignment. (a-c) Schematic representation of the (a) type I, (b) type II, and (c) type III heterostructure band alignment. (d) Calculated band alignment of TMDC monolayers. Solid and dashed lines represent values calculated from two different methods, and the dashed lines indicate the water reduction and oxidation potentials. Reproduced with permission from [10].

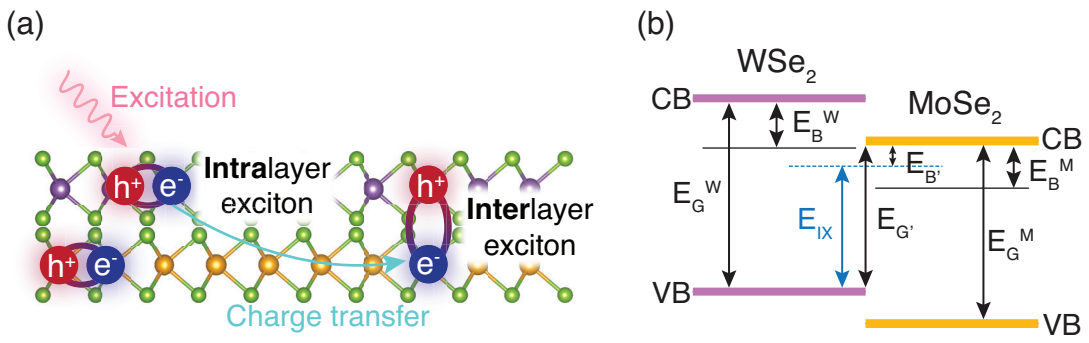

Figure 2.10: Interlayer exciton schematic. (a) Schematic illustration of the intralayer and interlayer exciton formation. Intralayer excitons are created by external excitation of charges. Charge transfer of carriers between layers created spatially separated interlayer excitons. (b) Type II band alignment of a WSe_2/$MoSe_2$ heterobilayer. E_G^W (E_G^M) is the band gap energy of WSe_2 ($MoSe_2$). E_B^W (E_B^M) is the binding energy of WSe_2 ($MoSe_2$) intralayer exciton. $E_{G'}$ is the interlayer band gap energy, $E_{B'}$ in the interlayer exciton binding energy, and E_{IX} is the interlayer exciton energy (Note: this is a simplified picture that ignores the twist angle between layers). Figure made with data presented in [11].

band structure to shift. The interlayer hopping in $K^{\pm}$ valleys is smaller than the band offset, and thus the interlayer hybridization is small [95]. In the Γ and Λ valleys, the interlayer hopping strength is comparable to the band offset, but it decays exponentially with the interlayer distance. Therefore, studies show that most heterobilayers have a CBM and VBM in the $K^{\pm}$ valleys, in opposite layers, resulting in a direct band gap optical transition [96, 94].

To fully understand interlayer excitons in heterobilayers, we must examine the effects of stacking two layers together on the electronic and optical properties, which we discuss in the following sections.

2.2.2 Theory of interlayer excitons

The real-space alignment and two distinct material types that make up heterobilayers affect their band structure, electronic, and optical properties. In particular, the relative rotation angle between the two layers and the lattice constants are the main factors at play. A small twist angle between layers is unavoidable for manually stacked heterobilayers, so the layers are not perfectly commensurate. In addition, the lattice constants of the four major TMDCs ($MoSe_2$, MoS_2, WSe_2, and WS_2) can differ up to 4% [97]. This real-space mismatch between the atomic registries translate directly into rotation of the BZ in each monolayer. If the twist angle is too large, the momentum mismatch at the BZ corners (the K valleys) is too large and can inhibit optical transitions. Therefore, we focus our attention on relatively small twist angles. Moiré superlattice can also form in heterobilayers and

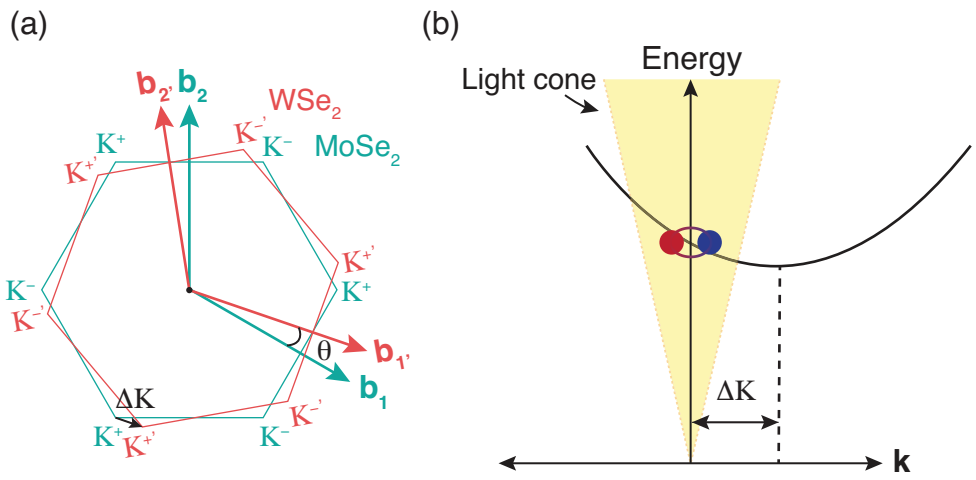

Figure 2.11: Twisted heterobilayer momentum valley physics. (a) Brillouin zone of a twisted heterobilayer. θ is the twist angle and ΔK is the shift in the K valleys. (b) Schematic depiction of the interlayer exciton dispersion in the two-particle representation. Optically bright interlayer exciton has a finite momentum.

can affect the electronic and optical properties, but we reserve the discussion until later sections.

For a $MoSe_2$/WSe_2 heterobilayer, the center-of-mass momentum K that result from the shift in the K valleys is given by [98]:

$$\Delta K = K_{\mathrm{MoSe_2}} \sqrt{\delta^2 + \theta^2}, \text{where } \delta = 1 - \frac{a_{\mathrm{MoSe_2}}}{a_{\mathrm{WSe_2}}}, \tag{2.13}$$

where δ is the lattice mismatch and θ is the twist angle. Figure 2.11(a) shows the BZs of a twisted heterobilayer. The interlayer exciton energy has the following dispersion:

$$E_{IX} = E_{G'} - E_{B'} + \frac{\hbar^2 (\boldsymbol{Q} - \boldsymbol{\Delta K})^2}{2M_{IX}}, \tag{2.14}$$

where $E_{G'}$ is the interlayer exciton band gap, $E_{B'}$ is the binding energy, $\boldsymbol{Q}$ is the exciton center-of-mass momentum, and M_{IX} is the total mass of the interlayer exciton ($M_{IX} = m_e + m_h$).

The light emission from interlayer exciton must satisfy momentum conservation constraints. However, the twist angle introduces a momentum mismatch between the valleys in each layer. This can be compensated if the interlayer exciton has a finite momentum, and therefore the interlayer exciton has a finite kinetic energy that is offset from the band

minimum. At the light cone ($Q = 0$) the interlayer kinetic energy is [99]:

$$E(Q = 0) = \frac{\hbar^2 \Delta K^2}{2M_{IX}}, \tag{2.15}$$

as illustrated in Figure 2.11(b).

Interlayer excitons can emit circularly polarized light, and the polarization depends on the crystal symmetry. We explore this concept in the next section.

2.2.3 Optical properties of interlayer excitons

Compared to intralayer excitons, interlayer excitons have a longer lifetime and a smaller binding energy due to the spatial separation of electrons and holes and increased dielectric screening. Time-resolved photoluminescence measurements show an interlayer exciton lifetime of 100s of ns or even up to μs for high quality samples [100, 101]. A consequence of long interlayer exciton lifetime is the lower oscillator strength compared to intralayer excitons, about two orders of magnitude lower [21]. Studies also report a high degree of valley polarization, over 80%, making interlayer excitons a good platform for 'valleytronic' studies [84]. The binding energy of $MoSe_2$/WSe_2 heterobilayer is around 150 meV [93], which is about 30% lower than the intralayer excitons, due to the increased dielectric screening in heterostructures compared to monolayers. The binding energy is still higher than the thermal energy, meaning interlayer excitons can persist up to room temperature.

For heterobilayers with relatively small twist angles, the optical selection rules can be determined by symmetry arguments. First, there are two types of stacking orders we must consider: R-type and H-type. R-type (H-type) stacking is when the two layers have close to 0° (180°) relative rotation angle, as shown in Figure 2.12. The two stacking orders have different selection rules. The crystalline structure of monolayer TMDCs have a $2\pi/3$ rotational symmetry ($\hat{C}_3$) which determines the allowed optical transitions. The detailed derivation of the Bloch functions, optical transition matrix element and the selection rules are shown in Refs. [12, 94], and we summarize the results below.

The $\hat{C}_3$ symmetry dictates the optical transition of interlayer excitons. Specifically, the C_3 quantum number for the transition between conduction band of one layer (c') and the valence band of another (v) determines the polarization of light [12]:

$$\sigma\pm, \text{when } C_3(c') - C_3(v) + S'_z - S_z = 3N \pm 1, \tag{2.16}$$

$$z, \text{when } C_3(c') - C_3(v) + S'_z - S_z = 3N, \tag{2.17}$$

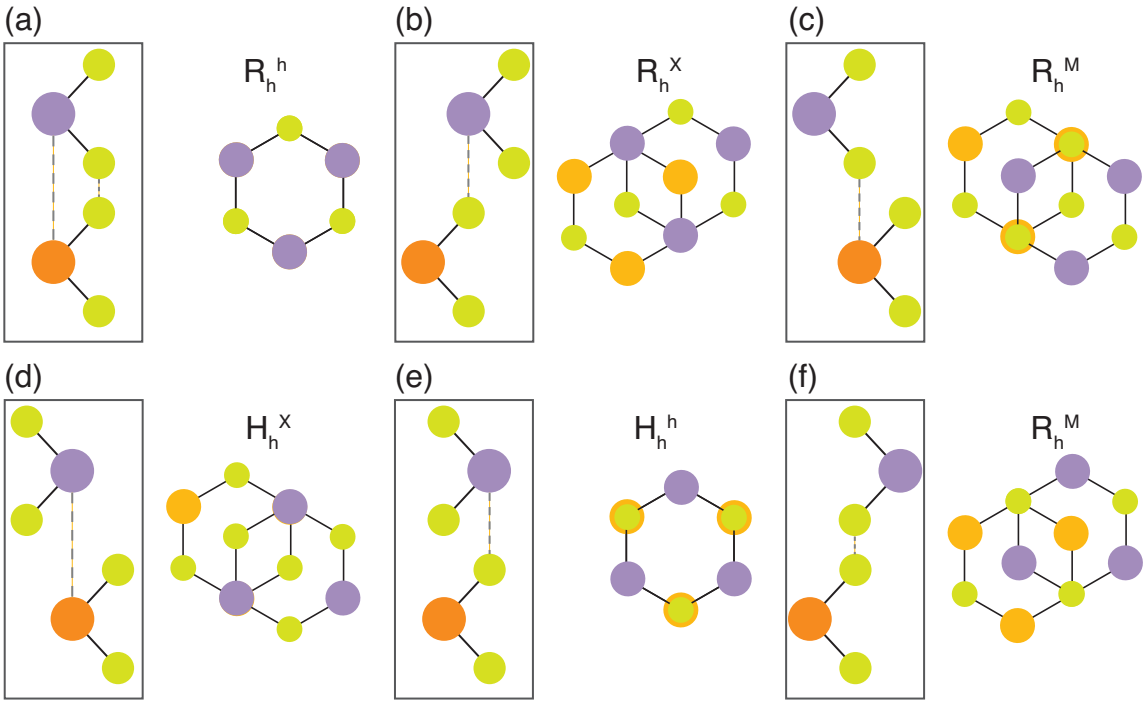

Figure 2.12: Stacking order and atomic registries of heterobilayers. (a-c) Atomic registries of R-stacked heterobilayer. (d-f) Atomic registries of H-stacked heterobilayer. Both the side view (on left) and the top view (on right) are illustrated. Figure recreated from [12] with permission.

	R_h^h	R_h^X	R_h^M	H_h^X	H_h^h	H_h^M
$v,\uparrow \leftrightarrow c',\uparrow$	σ^+	σ^-	z	σ^+	σ^-	z
$v,\uparrow \leftrightarrow c',\downarrow$	z	σ^+	σ^-	z	σ^+	σ^-
$v,\downarrow \leftrightarrow c',\downarrow$	σ^+	σ^-	z	σ^+	σ^-	z
$v,\downarrow \leftrightarrow c',\uparrow$	σ^-	z	σ^+	σ^-	z	σ^+

Table 2.1: The inter-valley optical selection rules between the valence band of one layer and the conduction band of another layer. Reproduced with permission from [12].

where $N = 0, \pm1, \pm2, \cdots$ are integers, S_z is the z-component of the spin angular momentum, and z is the out-of-plane polarization.

There are six atomic registries for R-type and H-type stacking (Figure 2.12). The light polarization that corresponds to the inter-valley optical transition at each atomic registry is summarized in Table 2.1.

2.3 Controlling excitons in TMDCs

Changing and controlling the properties of excitons in TMDCs allows more opportunities to engineer optoelectronic devices, such as LEDs, transistors, photodetectors, and solar cells, and to observe many-body physics phenomena, such as correlated electronic states and quantum simulators. In this section, we discuss electrical control of excitons via gating and doping, and the effects of moiré lattice on the exciton physics.

2.3.1 Electrical control

Changing the properties of excitons is important for both exploring the physics behind the materials and practical device applications. In semiconductors, controlling the flow of carriers through electrical contacts has been the primary method for making optoelectronic devices. For monolayer TMDCs, electrical doping can introduce carriers into the monolayer and generate new exciton species or change the dielectric environment. Electrostatic doping introduces free carriers and can form stable positively and negatively charged states whose energies are lower than the neutral exciton [102, 29]. Increasing the doping density will decrease the binding energy due to the increased screening of the Coulomb interaction. Therefore, electrical doping was used to demonstrate continuous change of the exciton binding energy in monolayer WSe_2 [103]. Similarly, the additional charges induced

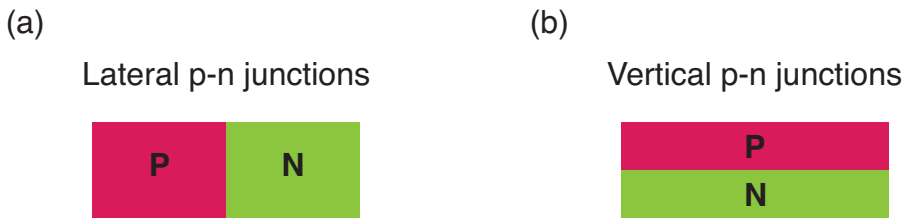

Figure 2.13: Schematic drawing of p-n junctions. (a) Lateral p-n junction and (b) vertical p-n junction.

by doping can also change the interconversion rate of the neutral and charge excitons and change the absorption and refractive index of the material [104, 105].

Another important application of electrostatic doping and carrier injection is the formation of p-n junctions for electroluminescence (EL), which is important for practical, on-chip integration of photonic devices [106]. There are two main ways of forming p-n junctions in TMDCs as illustrated in Figure 2.13. First is a lateral p-n junction that relies on carrier diffusion and radiative recombination. These devices have split gates and the distance between electrodes is limited by the diffusion length of electron and holes in the material. The lateral p-n junctions have been used to show EL in monolayers [107, 108, 109] and heterobilayers [20, 21]. A second method is the vertical p-n junction, which uses graphene top and bottom gates and a thin hBN tunnel barrier to allow electrons and holes to tunnel from the graphene to the conduction and valence band of the TMDC material. This method can be used to make larger area p-n junctions and has been used to demonstrate EL in monolayers and multilayers [110].

Interlayer excitons in heterobilayers have a permanent out-of-plane dipole moment. Therefore, an external electrical field can tune the exciton resonance and oscillator strength. The interlayer exciton energy shifts according to the Stark shift, which is proportional to the dipole moment and the electric field across the heterostructure ($\sim edE_{\text{hs}}$) [22]. Electric field can also be used to switch between interlayer, intralayer, and inter-intralayer hybridized excitons. Certain combinations of heterobilayers have closely aligned valence or conduction bands which can be tuned with external electric field, changing the exciton species present in the material and redistributing the oscillator strength. In addition, optical reflection spectroscopy shows a characteristic anti-crossing of the energy levels [111, 112].

2.3.2 Moiré superlattice

Stacking of two atomic lattices with small differences in lattice constants or twist angle can create a superlattice that has larger periodicity, called the moiré lattice (Figure 2.14(a)).

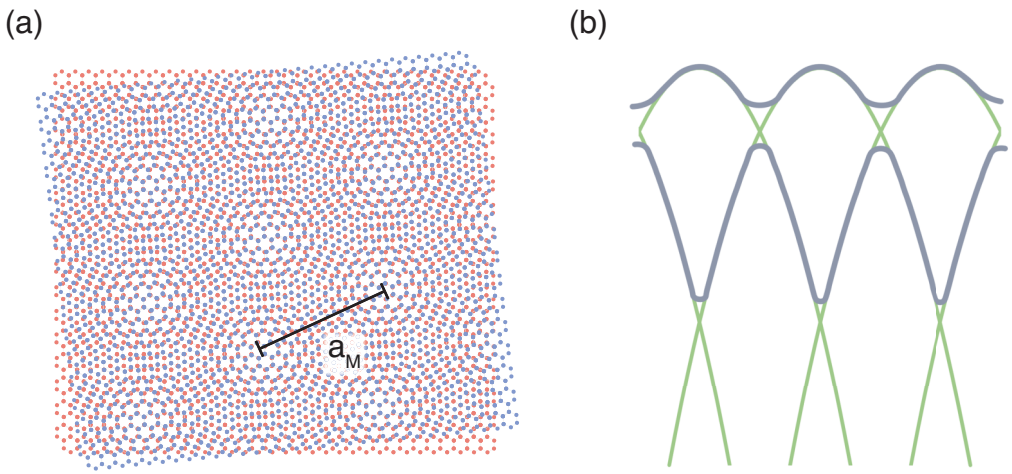

Figure 2.14: Moiré superlattice. (a) Diagram of a moiré superlattice pattern. a_M is the superlattice constant. (b) Schematic of the monolayer TMDC bands folded due to the superlattice potential. The green lines represent the monolayer band dispersion and the gray lines represent the new folded mini bands. Reproduced with permission from [3].

The superlattice constant is defined as:

$$a_M = \frac{a_0}{\sqrt{\delta^2 + \theta^2}}, \text{ where } \delta = \frac{|a_0' - a_0|}{a_0}. \tag{2.18}$$

a_0 and a_0' are the lattice constants of the two layers, and θ is the twist angle. The moiré lattice produces a periodic change in the potential energy experienced by electron and holes. This change in potential energy can result in localized moiré excitons [113, 114, 115] and trions [86, 116], and modified optical selection rules [19, 117]. The periodicity of the moiré lattice induces a modification of the band structure and results in folded 'mini bands' and mini BZs as shown in Figure 2.14(b). The mini bands are relatively flat, providing an ideal platform for observing strongly correlated electronic states [118, 119, 120, 121].

CHAPTER 3

Light-Matter Coupling in TMDCs

Controlling and enhancing the interactions between light and matter are essential for constructing integrated photonic devices which use light to efficiently store and process information. Classically, light-matter interaction is a resonant interaction of charged particles and electromagnetic waves. This classical model is also known as the Lorentz oscillator model, where atoms are considered to be small harmonically oscillating dipoles and the driving force is the electromagnetic waves. Quantum mechanically, we can consider a transition between two atomic states, ψ_1 with energy E_1, and ψ_2 with energy E_2. The time-dependent wave functions are:

$$\psi_1(\boldsymbol{r}, t) = \psi_1(\boldsymbol{r}) e^{-iE_1 t/\hbar}, \tag{3.1}$$

$$\psi_2(\boldsymbol{r}, t) = \psi_2(\boldsymbol{r}) e^{-iE_2 t/\hbar}. \tag{3.2}$$

The average position of the atom is defined as:

$$\langle \boldsymbol{r}(t) \rangle = \int \psi^*_{\text{tot}} \boldsymbol{r} \psi_{\text{tot}} d^3\boldsymbol{r}, \tag{3.3}$$

where ψ_{tot} is the superposition of ψ_1 and ψ_2 ($\psi_{\text{tot}} = \psi_1 + \psi_2$). The strength of the light-matter interaction depends on the transition dipole moment:

$$\langle \boldsymbol{p} \rangle = e \langle \boldsymbol{r} \rangle, \tag{3.4}$$

which has a matrix component:

$$e \int \psi^*_2(\boldsymbol{r})\ \boldsymbol{r}\ \psi_1(\boldsymbol{r}) d^3\boldsymbol{r}, \tag{3.5}$$

and an oscillation component:

$$e^{-i(E_1 - E_2)t/\hbar}. \tag{3.6}$$

We can see that an incident electromagnetic field resonant with the transition energy ($E_2 - E_1$) can put the atom into a superposition state of ψ_1 and ψ_2, and the atom can oscillate between the two states and emit electromagnetic radiation.

As the dipole radiates, the total power decays at a rate called the radiative decay rate (γ_{rad}). There are also non-radiative decay channels and decay rate (γ_{nr}). As the dipoles collide with each other, they can pick up a phase and can decrease the macroscopic polarization ($\boldsymbol{P}$). This is called the dephasing rate ($1/T_2'$). All of these decay channels determine the total polarization decay rate (γ).

We can solve the equation of motion for the macroscopic polarization and define:

$$\boldsymbol{P} = \epsilon_0 \chi \boldsymbol{E}. \tag{3.7}$$

$\boldsymbol{E}$ is the incident electric field with frequency ω, and χ is the electric susceptibility:

$$\chi = \frac{Ne^2}{m\epsilon_0} \frac{1}{(\omega_0^2 - \omega^2) + 2i\gamma\omega}, \tag{3.8}$$

where N is the number of dipoles and ω_0 is the resonant frequency. The real part of χ is a dispersive function and describes the real refractive index of the material. The imaginary part is a Lorentzian function and describes the absorption of the material [122]. Qualitatively, the susceptibility of a material contains information about the strength of the light-matter interaction and the optical properties.

Aside from the light-matter interaction that is intrinsic to the material, we can use external methods to control and enhance the interactions. A common way of achieving this is to use a cavity. The interaction strength between excitons and cavities determines the underlying physics and applications. This chapter will discuss the theory and background research on cavity light-matter coupling in TMDCs. Section 3.1 will introduce the available cavities for TMDCs and discuss the cavities relevant for this thesis in more detail. Section 3.2 discusses the strong coupling regime and section 3.3 discusses the weak coupling regime.

3.1 Semiconductor microcavities

A cavity is an optical resonator that confines and stores light at resonant frequencies. A microcavity has size that is comparable to the wavelength of light [123]. Microcavities confine light by reflecting it back when it reaches the boundary of the cavity. The microcavities used for semiconductors rely primarily on the photonic band gap and internal reflection. Much like an electronic band gap, photonic band gap is created when a periodic

modulation of the dielectric material results in band folding and opens up a band gap. Cavities that utilize internal reflection are often made with high index materials and rely on the reflection of light at the interface between a dielectric and the surrounding medium to trap light within the cavity.

Optical resonators are characterized by two main parameters: the quality factor and mode volume. The quality factor (Q) is a measure of how well the light stays confined in the cavity. In another words:

$$Q = 2\pi \frac{\text{stored energy}}{\text{energy loss per cycle}}, \tag{3.9}$$

which is equivalent to:

$$Q = \frac{\omega_c}{\Delta\omega_c}, \tag{3.10}$$

where ω_c is the resonance frequency, and $\Delta\omega_c$ is the spectral linewidth, or the full width at half maximum (FWHM), of the resonator modes [124]. A microcavity with a high Q-factor can allow longer photon lifetime, which is important for strong coupling.

The mode volume is the volume occupied by the optical mode:

$$V_{\text{eff}} = \frac{\int_V \epsilon(\boldsymbol{r})|\boldsymbol{E}(\boldsymbol{r})|^2 d^3\boldsymbol{r}}{\max[\epsilon(\boldsymbol{r})|\boldsymbol{E}(\boldsymbol{r})|^2]}, \tag{3.11}$$

where ϵ_r is the dielectric constant, $|\boldsymbol{E}(\boldsymbol{r})|$ is the electric field strength, and V is a quantization volume encompassing the resonator [125].

There are many different types of cavity configurations that are available for study, including mirror cavities, fibers or waveguides, whispering gallery modes, DBRs, and photonic-crystal defects (Figure 3.1).

In this section, we will discuss the two main types of cavities relevant to this thesis study, DBR microcavities and photonic grating waveguide cavities.

3.1.1 DBR microcavity

DBR microcavities are one of the most widely used cavities for semiconductors because they have high reflectivity. DBR is a periodic structure composed of alternating high and low refractive index materials, each with an optical thickness of $\lambda/(4n)$, where n is the index of refraction. Considering a single dielectric layer of thickness $\lambda/(4n)$, the optical path difference of incident light reflected off of the bottom surface is $\lambda/(2n)$ (which results in a total phase shift of π), and therefore adds in phase with the light reflected off of the top surface (which experiences a π phase shift), maximizing the reflectivity.

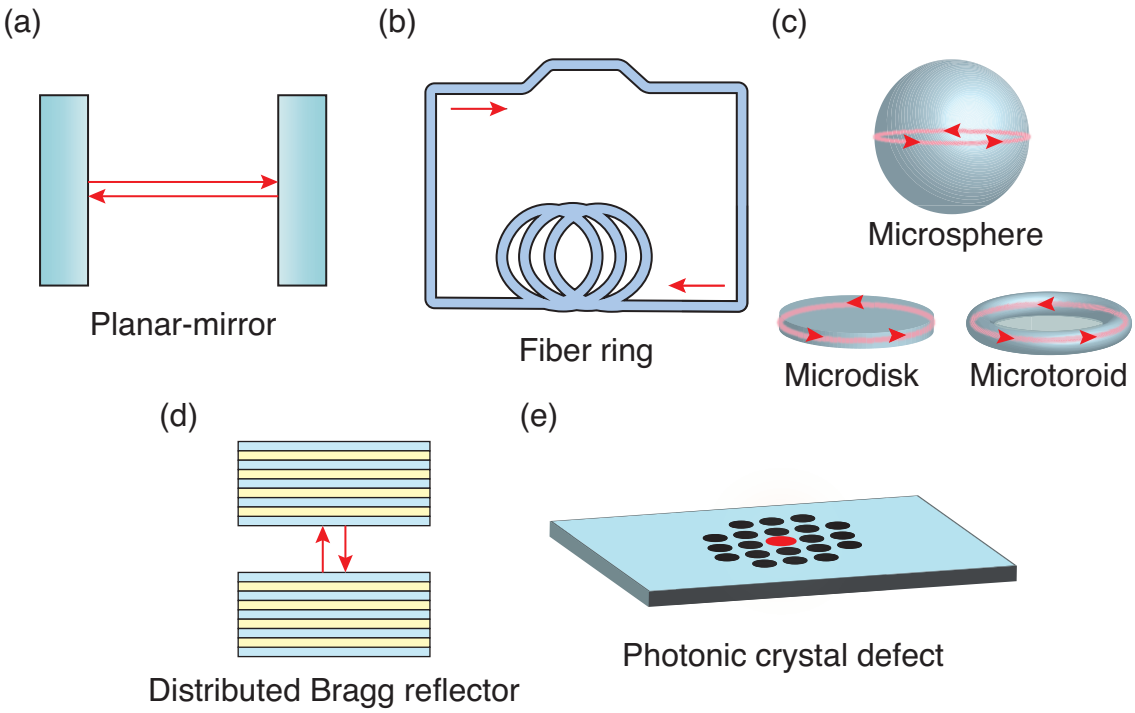

Figure 3.1: Types of cavities. (a) Planar-mirror cavity, (b) fiber ring cavity, (c) whispering gallery mode cavities, (d) DBR cavities, and (e) photonic crystal defect cavity.

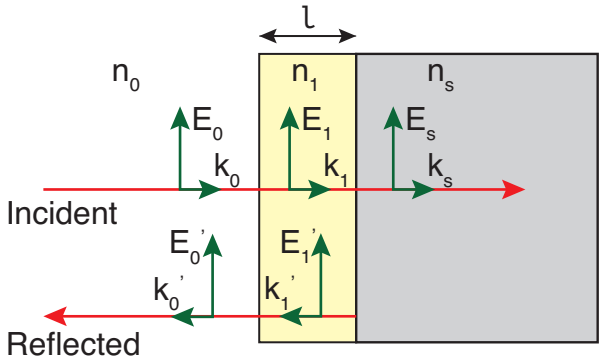

Figure 3.2: Electric field (E) and wave vectors (k) for a single dielectric layer on a substrate. The index of refraction of the incident material is n_0, dielectric material is n_1, and substrate is n_s. l is the thickness of the dielectric material.

The reflectivity of the DBR stack can be calculated using the transfer matrix method. First, we consider a single layer of material with index of refraction n_1 and thickness l, with electromagnetic waves incident from a material with index n_0, and the material is on a substrate with index of refraction n_s. A schematic illustration is shown in Figure 3.2. For simplicity, we consider normally incident light. The boundary conditions dictate that the tangential component of electric ($\vec{E}$) and magnetic ($\vec{H}$) fields must be continuous across the boundary. Along the first interface:

$$E_0 + E_0' = E_1 + E_1' \tag{3.12}$$

$$H_0 - H_0' = H_1 - H_1' \tag{3.13}$$

$$\text{or } \; n_0 E_0 - n_0 E_0' = n_1 E_1 - n_1 E_1'. \tag{3.14}$$

At the second interface,

$$E_1 e^{ikl} + E_1' e^{-ikl} = E_s \tag{3.15}$$

$$H_1 e^{ikl} - H_1' e^{-ikl} = H_s \tag{3.16}$$

$$\text{or } \; n_1 E_1 e^{ikl} - n_1 E_1' e^{-ikl} = n_s E_s. \tag{3.17}$$

The above equations can be simplified to:

$$1 + \frac{E_0'}{E_0} = \left(\cos kl - i \frac{n_s}{n_1} \sin kl \right) \frac{E_s}{E_0} \tag{3.18}$$

$$n_0 - n_0 \frac{E_0'}{E_0} = \left(-i n_1 \sin kl + n_s \cos kl \right) \frac{E_s}{E_0}. \tag{3.19}$$

Re-writing it in matrix form:

$$\begin{bmatrix} 1 \\ n_0 \end{bmatrix} + \begin{bmatrix} 1 \\ -n_0 \end{bmatrix} \frac{E_0'}{E_0} = \begin{bmatrix} \cos kl & -\frac{i}{n_1} \sin kl \\ -i n_1 \sin kl & \cos kl \end{bmatrix} \begin{bmatrix} 1 \\ n_s \end{bmatrix} \frac{E_s}{E_0}, \tag{3.20}$$

which can be further simplified to:

$$\begin{bmatrix} 1 \\ n_0 \end{bmatrix} + \begin{bmatrix} 1 \\ -n_0 \end{bmatrix} r = M \begin{bmatrix} 1 \\ n_s \end{bmatrix} t, \tag{3.21}$$

where r is the reflection coefficient, t is the transmission coefficient, and M is the transfer

matrix:

$$M = \begin{bmatrix} \cos kl & -\frac{i}{n_1}\sin kl \\ -in_1 \sin kl & \cos kl \end{bmatrix}. \tag{3.22}$$

For N layers the transfer matrix is:

$$M = M_1 M_2 M_3 \cdots M_N = \begin{bmatrix} A & B \\ C & D \end{bmatrix}, \tag{3.23}$$

and the reflection coefficient is:

$$r = \frac{An_0 + Bn_s n_0 - C - Dn_s}{An_0 + Bn_s n_0 + C + Dn_s}. \tag{3.24}$$

Now, we consider a pair of layers, one with a low index n_l and one with a high index n_h, each with $\lambda/(4n)$ layer thickness. Here, kl is $\pi/2$ so the transfer matrix is:

$$\begin{bmatrix} 0 & -\frac{i}{n_l} \\ -in_l & 0 \end{bmatrix} \begin{bmatrix} 0 & -\frac{i}{n_h} \\ -in_h & 0 \end{bmatrix} = \begin{bmatrix} -\frac{n_h}{n_l} & 0 \\ 0 & -\frac{n_l}{n_h} \end{bmatrix}. \tag{3.25}$$

If the DBR has N pairs, the transfer matrix is:

$$M = \begin{bmatrix} \left(-\frac{n_h}{n_l}\right)^N & 0 \\ 0 & \left(-\frac{n_l}{n_h}\right)^N \end{bmatrix}. \tag{3.26}$$

The reflectance of the DBR is:

$$R = |r|^2 = \left[\frac{(n_0/n_s)(-n_l/n_h)^{2N} - 1}{(n_0/n_s)(-n_l/n_h)^{2N} + 1}\right]^2 \tag{3.27}$$

[126]. We can see that more layers and higher refractive index contrast result in higher reflectance of the DBR mirror. A DBR has a broad, high reflectivity band called the stop band corresponding to a 1D photonic band gap. The width of the stop band is [127]:

$$\delta\lambda = \lambda_0 \frac{4}{\pi} \arcsin\left(\frac{n_h - n_l}{n_h + n_l}\right), \tag{3.28}$$

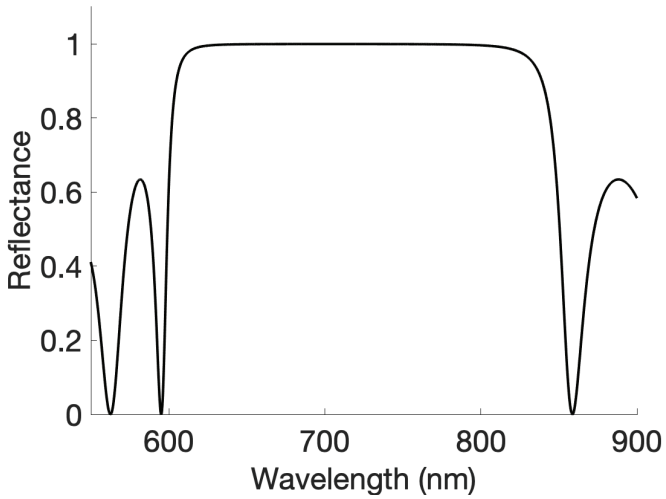

Figure 3.3: Reflection spectrum of a DBR mirror calculated using the transfer matrix method.

where λ_0 is the center wavelength of the stop band. Higher refractive index contrast results in a wider stop band. An example of a 1D DBR reflection spectrum calculated using the transfer matrix method is shown in Figure 3.3.

To form a cavity, two high-reflectance DBRs are stacked together with a spacer layer in between. The optical thickness of the spacer layer is a multiple of $\lambda_c/2$, where λ_c is the cavity resonance wavelength (Figure 3.4(a)). A plot of the refractive index and calculated electric field intensity is shown in Figure 3.4(b). In essence, the DBR cavity is a Fabry-Perot etalon with a sharp transmission peak at the resonance wavelength given by the airy function. The transmission is [126]:

$$T = \frac{(1-R_1)(1-R_2)}{[1-\sqrt{R_1R_2}]^2 + 4\sqrt{R_1R_2}\sin^2(\phi/2)}, \tag{3.29}$$

where R_1 and R_2 is the reflectivity of the two mirrors and ϕ is the phase difference that light acquires during a cavity round trip. The cavity resonance is a dip in the reflection spectrum, as shown in Figure 3.4(c).

The cavity dispersion energy for a planar DBR cavity is defined as [128]:

$$E_{\text{cav}} = \frac{\hbar c}{n_c}\sqrt{k_{\parallel}^2 + k_z^2}, \tag{3.30}$$

where n_c is the cavity index of refraction, and $k_{\parallel}$ (k_z) is the wave vector parallel (perpendicular) to the mirror layers. In the limit where $k_{\parallel} << k_z$, the above equation can be

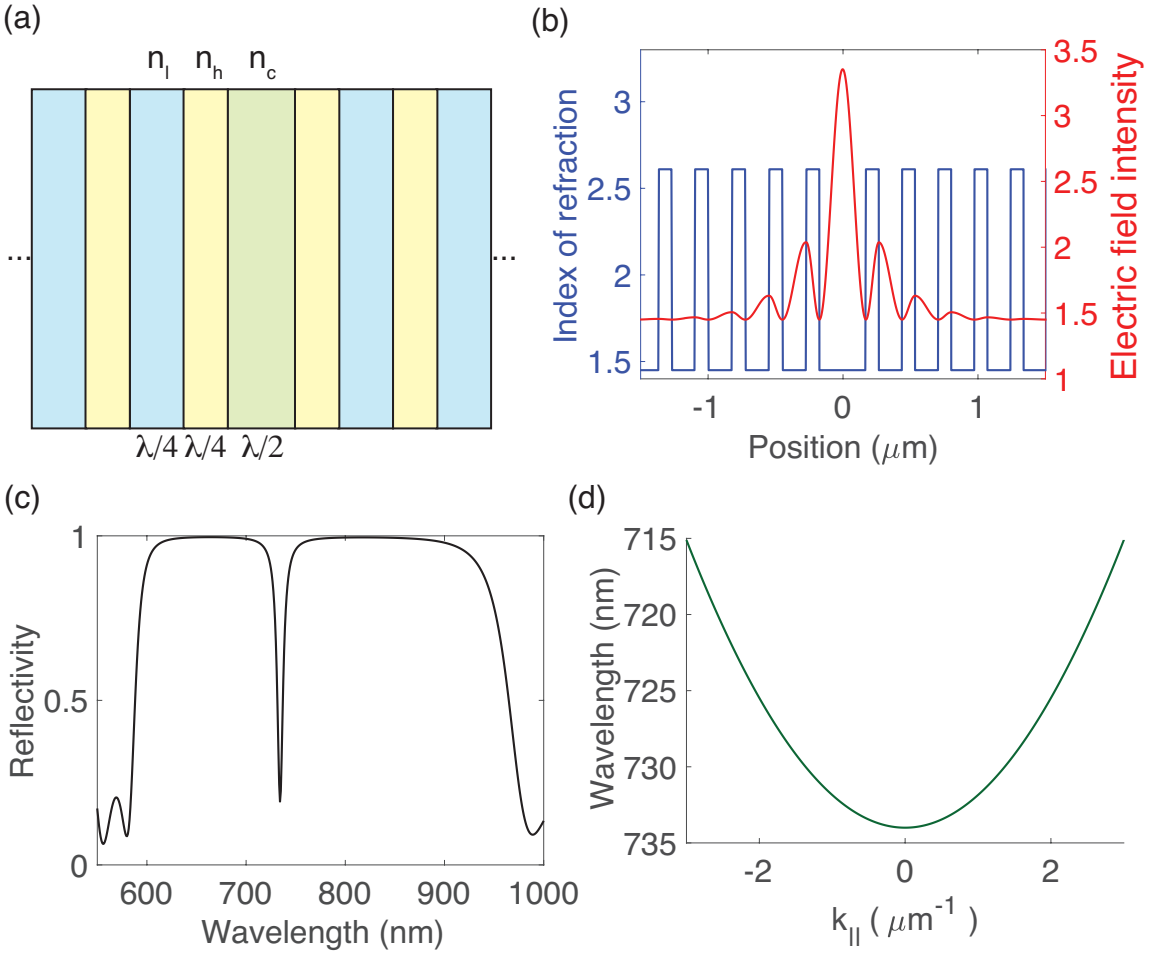

Figure 3.4: DBR microcavity. (a) Simplified schematic of the planar DBR microcavity structure. Each of the DBR layers has a $\lambda/4$ optical thickness with alternating high-index (n_h) and low-index (n_l) materials. The cavity optical length is $\lambda/2$ and the cavity index of refraction is n_c. (b) Cavity index of refraction and electric field intensity profiles. (c) Reflectivity spectrum of the DBR cavity calculated by the transfer matrix method. (d) Calculated angle-resolved energy dispersion of the DBR cavity.

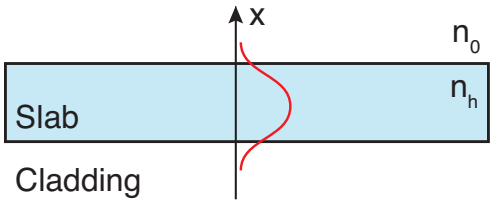

Figure 3.5: Slab waveguide. n_0 is the index of refraction of the cladding and n_h is the index of the slab. Red solid line is an illustration of the electric field profile of a symmetric mode.

simplified as:

$$E_{\text{cav}} \approx \frac{\hbar c}{n_c} k_z + \frac{\hbar^2 k_{\parallel}^2}{2m_{\text{cav}}}, \tag{3.31}$$

where the cavity effective mass is:

$$m_{\text{cav}} = \frac{2\pi\hbar}{\lambda_c c}. \tag{3.32}$$

Figure 3.4(d) shows the plotted cavity dispersion.

Since DBR microcavities can reach high Q-factors, it is an ideal platform for making strongly coupled exciton-polariton devices that show many-body physics phenomena, such as Bose-Einstein condensation or superfluidity. There are several different types of DBR cavities that are compatible with TMDCs, which we will discuss in Chapter 4.

3.1.2 Photonic grating cavity

A photonic grating cavity is a slab of dielectric material patterned with a sub-wavelength periodic modulation along the in-plane direction. Essentially, it is a slab waveguide with a periodic pattern. The waveguide supports a guided mode and the periodic pattern couples light in and out of the waveguide.

A slab waveguide is a high index medium (the 'slab') sandwiched between lower index layers (the 'cladding'), as illustrated in Figure 3.5. Then, total internal reflection traps light within the wave guide. Solving the electromagnetic wave equation from Maxwell's equations, we can obtain a solution for the S-polarized waves (in-plane, perpendicular to the wave propagation direction), which is an exponential function in the cladding and a

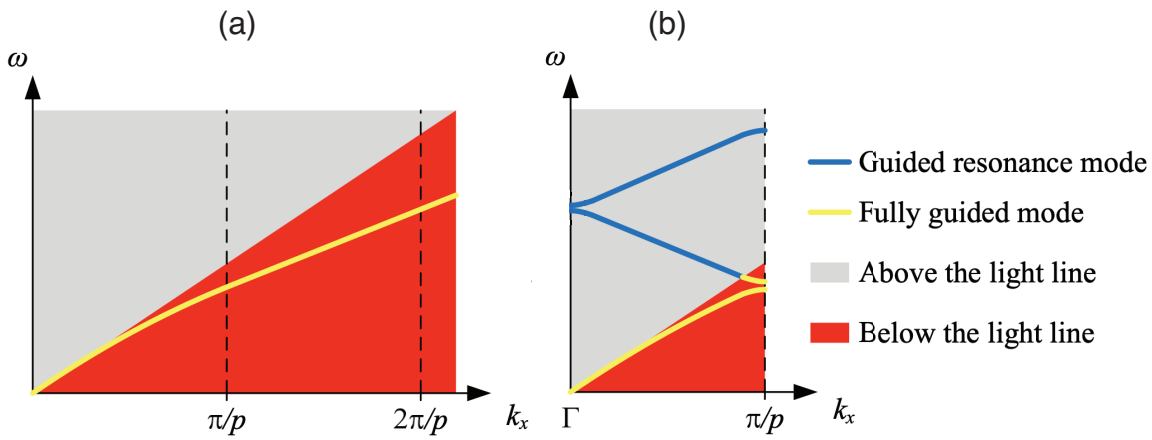

Figure 3.6: Guided resonance mode of (a) a slab waveguide versus (b) a patterened photonic grating mode. p is the periodicity of the photonic grating. Reproduced with permission from [13].

oscillatory function in the slab:

$$E_{\text{cladding}} = E_c e^{\pm \alpha x}, \text{ where } \alpha = \sqrt{\beta^2 - n_0^2 k_0^2}, \tag{3.33}$$

$$E_{\text{slab}} = E_s \cos(hx) + E_a \sin(hx), \text{ where } h = \sqrt{n_h^2 k_0^2 - \beta^2}. \tag{3.34}$$

β is the total propagation constant, n_0 is the refractive index of the cladding, $k_0 = \omega^2/c^2$ is the vacuum wave vector, and n_h is the refractive index of the slab. At the edges of the slab boundary, the fields must be continuous. We can see that a higher index contrast between the slab and the cladding results in more confinement of the electromagnetic fields within the slab. The electric field of the resonant mode is confined in the slab and exponentially decays in the cladding region. Therefore, for a realistic device, it is important to place the active medium as close to the waveguide as possible and also have a slab that is thick enough to support a guided mode but not too thick as to reduce the coupling between the mode and the active medium.

The guided mode resonance in a slab waveguide is not optically accessible and lies outside of the light cone. The periodic patterning of the slab folds the resonance band and makes the guided mode optically accessible (Figure 3.6). Because the periodicity is present only along one of the directions, the guided mode is anisotropic and has polarization dependence. On resonance, the light must be trapped inside of the cavity and not interfere destructively with each other. Thus, the phase difference between the diffracted and transmitted wave is π and total destructive interference of transmitted light occurs at the resonance [129]. Experimentally, the resonance mode shows up as a peak in the reflectance

spectrum. The line shape of the reflectance peak is an anti-symmetric Fano resonance due to the interference between the portion of the light that goes directly through the slab and the light that couples to the guided mode before decaying [130].

Photonic grating cavities are compact and relatively simple to fabricate, making them ideal for integrating with a variety of materials and photonic structures. Details of the grating fabrication procedure is shown in Chapter 4.

3.2 Strong coupling exciton-polaritons

In the strong coupling regime, the photon can be emitted and reabsorbed by excitons coherently and reversibly, and the light-matter coupling rate is larger than the decay rate of the system. In other words, the photon is reabsorbed by the exciton before it escapes the cavity. In the strong coupling regime, the energy eigenstates of excitons and cavity photons mix and hybridize to form new energy eigenstates that are a superposition of the exciton and cavity modes. Thus, the new elementary excitations are called exciton-polaritons, which are quasi-particles that result from strongly coupled light and matter. Experimentally, strong coupling is demonstrated by measuring the anti-crossing pattern between the exciton and cavity modes, either through reflectivity or PL measurements.

The Hamiltonian of exciton-polaritons in a microcavity is given by:

$$\hat{H}_{\text{pol}} = \hat{H}_{\text{cav}} + \hat{H}_{\text{exc}} + \hat{H}_{\text{I}}, \tag{3.35}$$

where $\hat{H}_{\text{cav}}$ is the cavity, $\hat{H}_{\text{exc}}$ is the exciton, and $\hat{H}_{\text{I}}$ is the interaction Hamiltonians. In the matrix format this Hamiltonian is:

$$\hat{H}_{\text{pol}} = \begin{pmatrix} E_{\text{exc}}(k_{\parallel}) & \hbar\Omega \\ \hbar\Omega & E_{\text{cav}}(k_{\parallel}, k_z) \end{pmatrix}, \tag{3.36}$$

where the exciton $|X\rangle$ and cavity $|C\rangle$ vectors are the basis vectors:

$$|X\rangle = \begin{pmatrix} 1 \\ 0 \end{pmatrix}, \; |C\rangle = \begin{pmatrix} 0 \\ 1 \end{pmatrix}. \tag{3.37}$$

$E_{\text{exc}}(k_{\parallel})$ and $E_{\text{cav}}(k_{\parallel}, k_z)$ are the exciton and cavity resonant energies, respectively, and $k_{\parallel}$ (k_z) is the in-plane (out-of-plane) wave number. The term $2\hbar\Omega$ is called the Rabi splitting

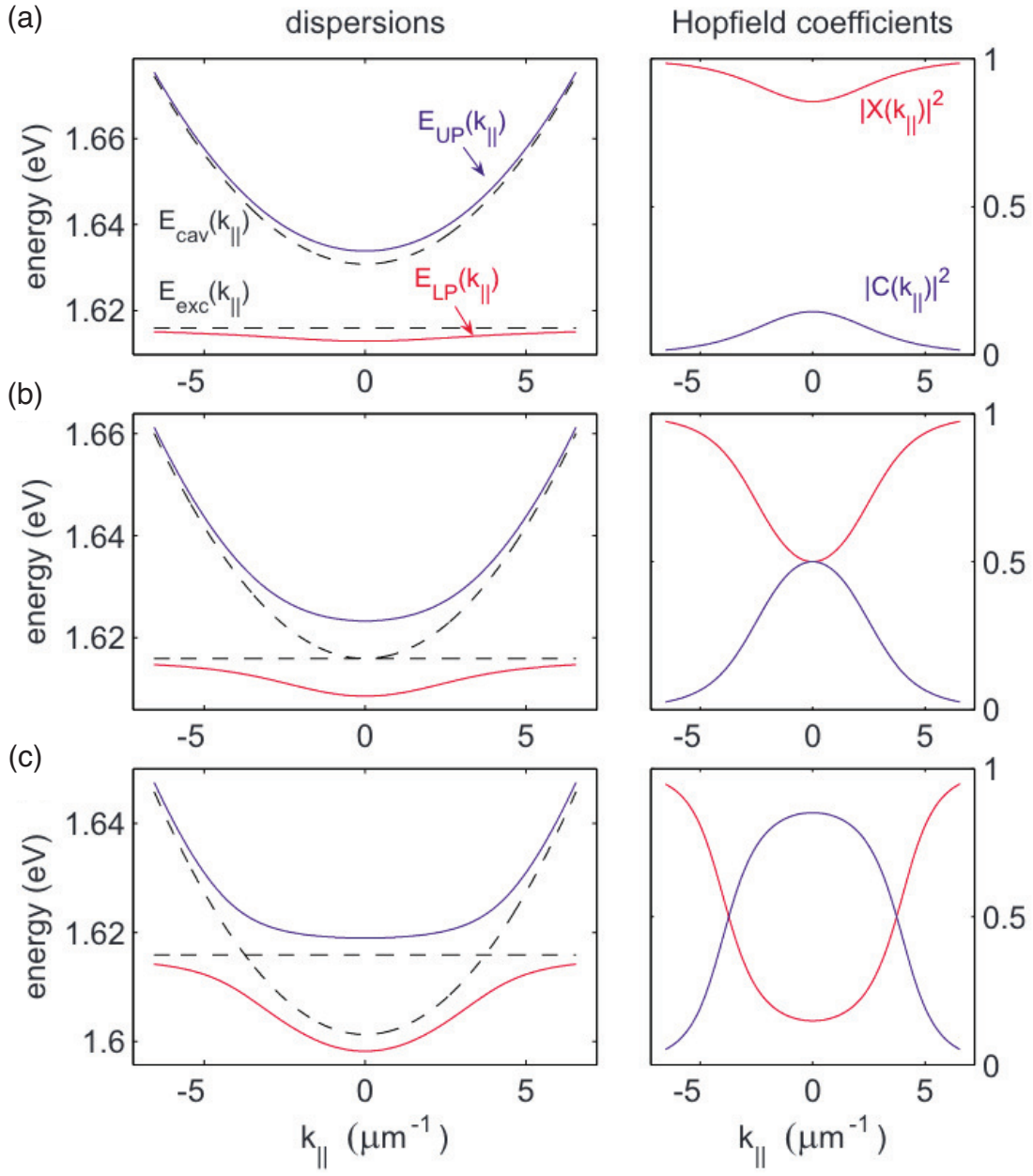

Figure 3.7: Polariton energy dispersion and Hopfield coefficients at different detunings. The detunings are: (a) $+2\hbar\Omega$, (b) 0, and (c) $-2\hbar\Omega$. Reproduced with permission from [14].

and it describes the exciton cavity coupling strength. Diagonalization of the Hamiltonian matrix leads to:

$$\hat{H} = \begin{pmatrix} E_{\text{UP}}(k_\parallel) & 0 \\ 0 & E_{\text{LP}}(k_\parallel) \end{pmatrix}, \tag{3.38}$$

where $E_{\text{UP}}(k_\parallel)$ and $E_{\text{LP}}(k_\parallel)$ are upper and lower polariton energies. The new basis vectors are linear combinations of exciton and cavity basis vectors.

Another way of writing the polariton Hamiltonian is in the equation form [131]:

$$\hat{H}_{\text{pol}} = \sum E_{\text{cav}}(k_\parallel, k_z)\, \hat{a}^\dagger_{k_\parallel} \hat{a}_{k_\parallel} + \sum E_{\text{exc}}(k_\parallel)\, \hat{b}^\dagger_{k_\parallel} \hat{b}_{k_\parallel} + \sum \hbar\Omega(\hat{a}^\dagger_{k_\parallel} \hat{b}_{k_\parallel} + \hat{a}_{k_\parallel} \hat{b}^\dagger_{k_\parallel}), \tag{3.39}$$

where $\hat{a}^\dagger$ and $\hat{a}$ are the photon creation and annihilation operators, and $\hat{b}^\dagger$ and $\hat{b}$ are the exciton creation and annihilation operators. This Hamiltonian can be diagonalized using new basis vectors:

$$\hat{P}_{k_\parallel} = X_{k_\parallel} \hat{b}_{k_\parallel} + C_{k_\parallel} \hat{a}_{k_\parallel} \tag{3.40}$$

$$\hat{Q}_{k_\parallel} = -C_{k_\parallel} \hat{b}_{k_\parallel} + X_{k_\parallel} \hat{a}_{k_\parallel}. \tag{3.41}$$

The new Hamiltonian becomes:

$$\hat{H}_{\text{pol}} = \sum E_{\text{LP}}(k_\parallel)\, \hat{P}^\dagger_{k_\parallel} \hat{P}_{k_\parallel} + \sum E_{\text{UP}}(k_\parallel)\, \hat{Q}^\dagger_{k_\parallel} \hat{Q}_{k_\parallel}. \tag{3.42}$$

$\hat{P}^\dagger_{k_\parallel}$ and $\hat{P}_{k_\parallel}$ are creation and annihilation operators of the lower polaritons, and $\hat{Q}^\dagger_{k_\parallel}$ and $\hat{Q}_{k_\parallel}$ are creation and annihilation operators of the upper polaritons. The difference between cavity and exciton energies is referred to as the detuning:

$$\Delta E(k_\parallel) = E_{\text{cav}}(k_\parallel, k_z) - E_{\text{exc}}(k_\parallel). \tag{3.43}$$

$X_{k_\parallel}$ and $C_{k_\parallel}$ are Hopfield coefficients and they describe the exciton and photon fraction in lower and upper polaritons. They are defined as [132]:

$$|X_{k_\parallel}|^2 = \frac{1}{2}\left(1 + \frac{\Delta E(k_\parallel)}{\sqrt{\Delta E(k_\parallel)^2 + 4\hbar^2\Omega^2}}\right) \tag{3.44}$$

$$|C_{k_\parallel}|^2 = \frac{1}{2}\left(1 - \frac{\Delta E(k_\parallel)}{\sqrt{\Delta E(k_\parallel)^2 + 4\hbar^2\Omega^2}}\right), \tag{3.45}$$

where $|X_{k_\parallel}|^2 + |C_{k_\parallel}|^2 = 1$. The eigen-energies of the diagonalized Hamiltonian is:

$$E_{\text{LP, UP}}(k_\parallel) = \frac{1}{2}\left[E_{\text{exc}} + E_{\text{cav}} \pm \sqrt{4\hbar^2\Omega^2 + (E_{\text{exc}} - E_{\text{cav}})^2}\right]. \tag{3.46}$$

When $E_{\text{exc}} = E_{\text{cav}}$, the energy difference between upper and lower polaritons is: $E_{\text{UP}} - E_{\text{LP}} = 2\hbar\Omega$, which is the Rabi splitting. A requirement for strong-coupling is a non-vanishing Rabi splitting that is greater than the sum of the cavity and exciton FWHMs:

$$\hbar\Omega > (\gamma_{\text{cav}} + \gamma_{\text{exc}})/2. \tag{3.47}$$

Exciton-polaritons possess properties of both excitons and photons so their properties can be determined by the exciton and photon fractions, or the Hopfield coefficients. The polariton effective mass is:

$$\frac{1}{m_{\text{LP}}} = \frac{|X|^2}{m_{\text{exc}}} + \frac{|C|^2}{m_{\text{cav}}} \tag{3.48}$$

$$\frac{1}{m_{\text{UP}}} = \frac{|C|^2}{m_{\text{exc}}} + \frac{|X|^2}{m_{\text{cav}}}, \tag{3.49}$$

where X and C are Hopfield coefficients, m_{exc} is the exciton effective mass, and m_{cav} is the cavity effective mass. The polariton radiative lifetime is:

$$\gamma_{\text{LP}} = |X|^2\gamma_{\text{exc}} + |C|^2\gamma_{\text{cav}} \tag{3.50}$$

$$\gamma_{\text{UP}} = |C|^2\gamma_{\text{exc}} + |X|^2\gamma_{\text{cav}}, \tag{3.51}$$

where γ_{exc} is the exciton lifetime and γ_{cav} is the cavity photon lifetime.

Exciton-polaritons' unique properties make them ideal for a novel coherent light sources and observing many-body physics. Our work on engineering a new type of exciton-polariton device with TMDCs is shown in Chapter 5.

3.3 Weak coupling

In the weak coupling regime, the photon escapes the cavity before being resonantly reabsorbed by the exciton, and the light-matter coupling rate is smaller than the decay rate of the system. Therefore, the decay of exciton is irreversible and the cavity only alters the radiative lifetime of the exciton. When the exciton energy is resonant with the cavity mode energy, the optical density of states increases and the spontaneous decay rate of the exciton is enhanced. On the other hand, when the exciton energy is off-resonant, the emission rate

decreases.

The spontaneous emission rate of a dipole emitter follows the Fermi's golden rule:

$$\Gamma_{i\to f} = \frac{2\pi}{\hbar^2} \left|\boldsymbol{p}\cdot\boldsymbol{E}(\boldsymbol{r},t)\right|^2 \rho(\omega), \tag{3.52}$$

where $|\boldsymbol{p}\cdot\boldsymbol{E}(\boldsymbol{r},t)|^2$ is the transition dipole matrix element and $\rho(\omega)$ is the photon density of states. For photons that have a linear dispersion relation ($E = \hbar\omega = \hbar ck$), the 3D density of states in vacuum is:

$$\rho_{\text{vac}}(\omega) = \frac{\omega^2 V n^3}{\pi^2 c^3}, \tag{3.53}$$

where ω is the angular frequency of light, V is the mode volume, and n is the refractive index. On the other hand, the density of states in a cavity is modified and can be calculated using a new cavity wave vector. The cavity density of states is [133]:

$$\rho_{\text{cav}}(\omega) = \frac{2}{\pi} \frac{\Delta\omega_c^2}{4(\omega-\omega_c)^2 + \Delta\omega_c^2}. \tag{3.54}$$

Recall $Q = \omega_c/\Delta\omega_c$. At resonance, the ratio of spontaneous emission rates inside the cavity and in the vacuum can be written as:

$$F_P = \frac{\Gamma_{\text{cav}}}{\Gamma_{\text{vac}}} = \frac{3}{4\pi^2}\left(\frac{\lambda_c}{n}\right)^3 \frac{Q}{V}, \tag{3.55}$$

where λ_c is the resonance wavelength. This is also known as the Purcell factor.

Weak coupling is a way of modifying the light-matter interactions in semiconductors are used for photonic technologies, such as semiconductor photon lasers and cavity-enhanced single photon sources. We introduce a weakly coupled interlayer exciton photon laser in Chapter 6.

CHAPTER 4

Experimental Methods

This chapter introduces the key experimental methods and techniques used to prepare, fabricate, and measure TMDC monolayer and heterobilayer devices. Specifically, section 4.1 discusses monolayer sample exfoliation and transfer techniques. Section 4.2 discusses heterobilayer sample preparation techniques, including crystal axes identification through second harmonic generation spectroscopy, and rotational alignment and transfer of heterobilayers. Section 4.3 introduces the different microcavity fabrication techniques. Section 4.4 illustrates the various optical measurement setups and techniques. Section 4.5 introduces electrical device fabrication and measurement techniques.

4.1 Monolayer sample preparation

TMDCs are direct bandgap and optically accessible in the monolayer limit. The discovery of monolayer sample preparation techniques revolutionized the field of 2D materials and continues to be revised and improved upon to produce larger and cleaner monolayers with better optical quality. There are several different monolayer sample preparation techniques. First is mechanical polymer exfoliation, which is relatively cheap and easy to perform, and can produce clean samples with high optical quality. However, the size of the monolayer flakes are only on the order of tens of microns. Next, large-area monolayer growth techniques such as chemical vapor deposition (CVD) , molecular beam epitaxy (MBE), and atomic layer deposition (ALD) can produce wafer-sized monolayers but the optical quality is still lower than that of mechanically exfoliated monolayers. In this thesis, we focus on the mechanically-exfoliated samples and this section will introduce an exfoliation technique that uses PDMS.

Encapsulation of monolayer with hBN has been shown to improve the optical quality of monolayers by reducing the inhomogeneous broadening of the emission linewidth. This section will introduce the hBN encapsulation and transfer techniques, namely PET and PC

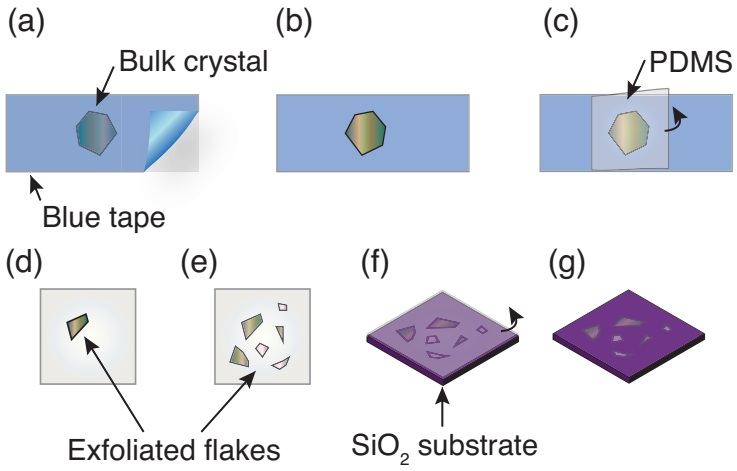

Figure 4.1: Monolayer exfoliation. (a) Blue tape is pressed onto the bulk crystal. (b) A thin layer of bulk crystal is transferred onto the blue tape. (c) A sheet of PDMS is pressed and lifted up to exfoliate the crystal. (d) Exfoliated crystal on PDMS. (e) Another sheet of PDMS is used to further exfoliate the flakes. (f) PDMS is pressed onto the SiO_2 substrate and lifted up. (g) Exfoliated flakes on SiO_2 substrate.

transfers.

4.1.1 Monolayer exfoliation

A graphical representation of the monolayer exfoliation process is shown in Figure 4.1. The first step of monolayer exfoliation is preparing the substrate. A typical substrate is a SiO_2/Si wafer with 285 nm oxide thickness (Graphene Supermarket). This wafer provides good visibility of the TMDC flakes for easy identification of monolayers. To prepare the SiO_2 substrate, the wafer is cut into small (approximately 1.5 cm $\times$ 1.5 cm) pieces using a diamond scribe. Then, the dust and particles on the substrate are cleaned off using a nitrogen gun. Lastly, the substrate is baked on a hotplate at 100 °C for about 3 minutes to reduce the moisture content.

Next step is to isolate a thin, sub-millimeter layer of bulk crystal onto a clear blue PVC tape (Nitto SPV 224). This blue tape has low residue and therefore is good for keeping the sample clean. We press the sticky side of the blue tape onto a bulk TMDC crystal (HQ graphene) and lightly press down with a cotton swab to coat the crystal with the tape. Then, we gently peel off the blue tape, revealing a layer of exfoliated bulk crystal on the tape. This blue tape is often called the 'mother tape'.

Then, we further thin down the crystal on the mother tape with a sheet of polymer material, such as PDMS, Scotch Tape, or blue tape. In this thesis, we focus on the PDMS method because it produces monolayers at a high yield. We use a commercial PDMS

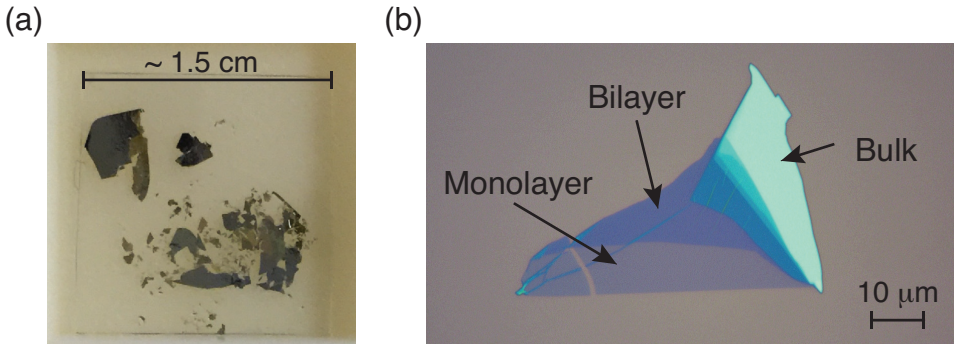

Figure 4.2: Images of exfoliated TMDCs. (a) Image of a sheet of PDMS with exfoliated TMDCs. Final exfoliation onto the substrate using this PDMS is likely to produce a monolayer. (b) Optical microscope image of an exfoliated TMDC flake that has monolayer, bilayer, and bulk regions.

(Gel-Pak X4 6.4 mils) which is clean and has uniform thickness. To prepare the PDMS, we cut it into small pieces to roughly match the size of the prepared substrate. Then, the polyethylene coversheet is peeled off, revealing the PDMS polymer. The polymer is then brought into contact with the crystals on the mother tape and pressed down to ensure full contact. Then, the PDMS sheet is gently but swiftly peeled off with a tweezer. Note that PDMS is more adhesive when peeled off quickly. Therefore, more crystals can transfer onto it when removed quickly from the mother tape. Another clean sheet of PDMS can be pressed onto the original PDMS to further thin the layers down. This process can be repeated several times until the crystals reach an optimal thickness. In order to determine whether the crystals have optimal thickness, we visually inspect the PDMS sheet and look for thin and transparent layers. An example of a PDMS sheet that is highly likely to produce a monolayer is shown in Figure 4.2(a).

Next, the PDMS sheet is pressed onto the prepared substrate and peeled off slowly to transfer some of the flakes onto the substrate. Then, using an optical microscope, we search the substrate for monolayers. Monolayers can be identified by their color contrast. An optical image of monolayers, bilayers and bulk is shown in Figure 4.2(b).

On average, this method produces at least one monolayer per 1.5 cm $\times$ 1.5 cm size wafer. The size of the monolayer flake is highly varied, but for practical devices we seek monolayers that are large (larger than 10 μm $\times$ 10 μm), clean, and uniform to maximize the chances of producing a good sample for optical and electrical measurements.

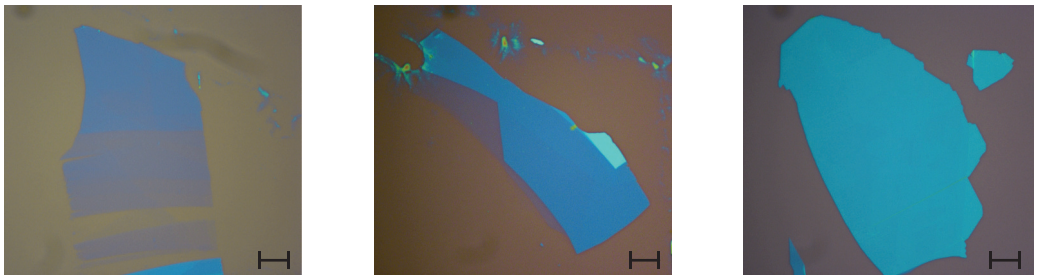

Figure 4.3: Images of exfoliated hBN. Optical microscope images of three different exfoliated hBN flakes that can be used to encapsulate TMDCs. The scale bar is 10 μm.

4.1.2 hBN exfoliation

The process of exfoliating hBN is very similar to that of monolayers, with the exception of a few key steps. First, high quality hBN is more valuable, so we take additional steps to conserve the bulk crystal. We use Scotch Tape to exfoliate a piece of hBN from its bulk crystal and repeatedly fold the tape onto itself to further thin down the material, making sure the exfoliated flakes do not overlap when folding the tape. This minimizes tearing and breaking of the hBN flakes. This first tape is the mother tape. Then we press a new layer of Scotch Tape onto the mother tape and peel it off to transfer some of the flakes onto the new tape. The new tape is pressed onto a substrate and peeled very slowly and uniformly to exfoliate the hBN flakes onto the substrate. It is important to do this procedure slowly to ensure high yield of large and clean hBN flakes. We search the substrate under the microscope for hBN that is few tens of layers thick (15 nm - 25 nm). Layers that are too thin can crack and does not sufficiently flatten the monolayer. Layers that are too thick can hinder the optical emission. Optical images of suitable hBN flakes are shown in Figure 4.3. After the exfoliation, we store the mother tape in a desiccator and reuse the tape until it no longer produces good hBN flakes.

4.1.3 Encapsulation

Once we have the monolayers and hBN, the next step is to encapsulate the monolayer with hBN. Encapsulation is a delicate process because it involves picking up the monolayer (which is only several tens of microns large and about 0.6 nm thick) from its substrate without causing damage and sandwiching it between two layers of hBN. There are several different methods of encapsulation but here, we present two main methods that we have fine-tuned and optimized over the past several years to produce high quality TMDC samples.

The first method is so-called the PET method, which is fast, simple, and ideal for pro-

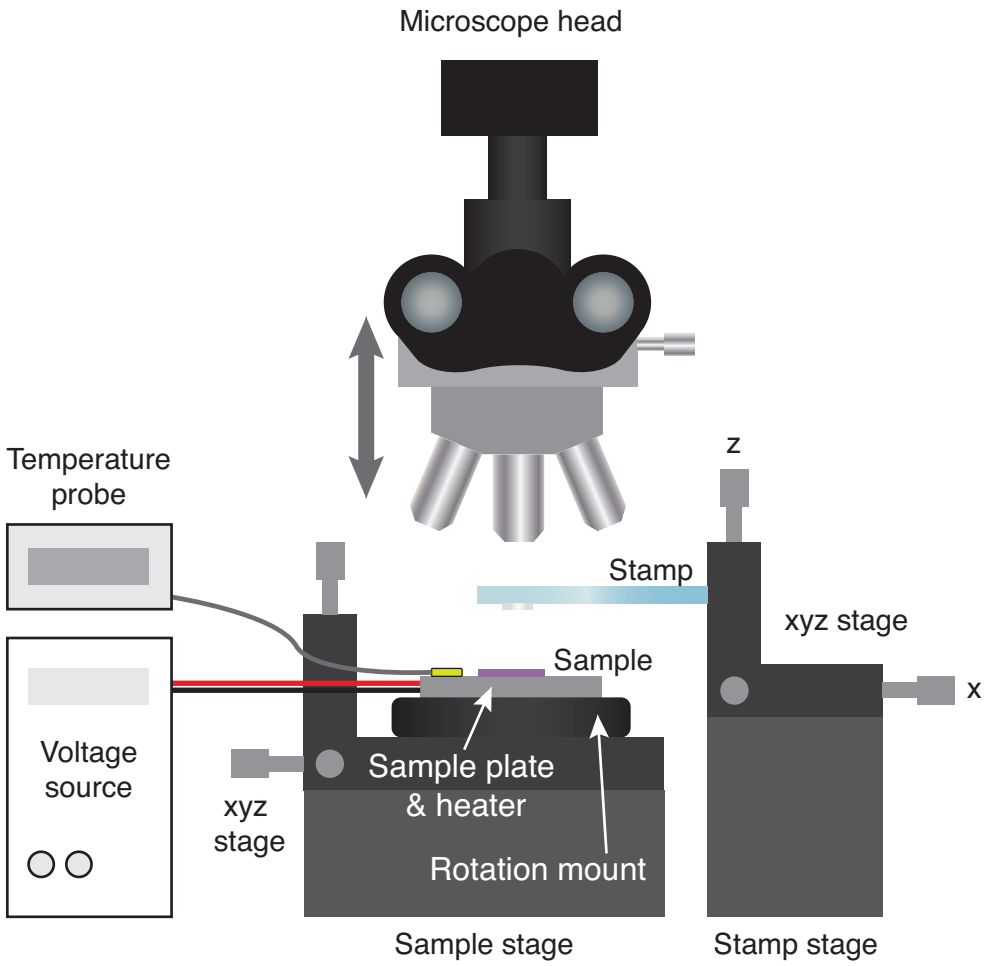

Figure 4.4: Schematic illustration of the transfer stage setup.

ducing a large quantity of samples. However, with this method, we cannot easily isolate the sample from the surrounding bulk flakes and more residue is deposited on the substrate. Therefore, the PET method is suitable for making samples that will be used for material characterization measurements.

Another method is the PC method, which is slower than the PET method but utilizes a small hemisphere stamp to precisely control the amount of bulk flakes we pick up during the process. Therefore, it produces monolayer samples that are clean and isolated from bulk pieces. This method is ideal for making samples that will be incorporated with micro-cavities or electrical contacts.

4.1.3.1 Transfer stage

Both the PET and PC methods use a 'transfer stage', which is a modified optical microscope with additional degrees of freedom. A schematic diagram of the transfer stage is shown in

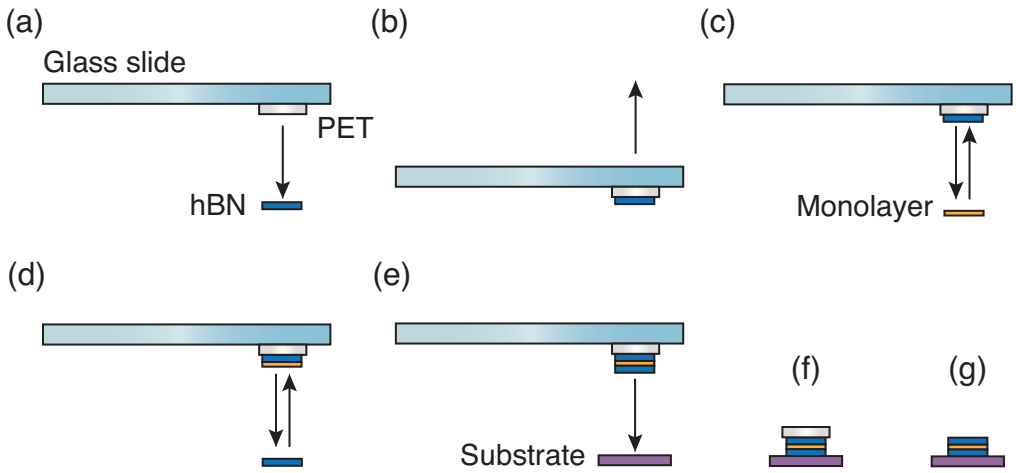

Figure 4.5: PET transfer procedure for encapsulating monolayers. (a) PET stamp is dropped down onto the top hBN, (b) Stamp is lifted up, picking up the hBN. (c) Monolayer is picked up. (d) Bottom hBN is picked up. (e) Sample is dropped down onto the final substrate. (f) After dropdown, the sample has PET on top. (g) PET is dissolved.

Figure 4.4. There are three main components: the microscope head, sample stage, and the stamp stage. The microscope head contains the optical components for the microscope and a camera that is connected to a computer. The objective lens turret moves in the z-direction, allowing us to focus the optical components during the transfer process without disturbing the sample or the stamp. The sample stage has a xyz stage and a rotational stage that can be used to move the sample. It also contains a sample heater and temperature probe. The sample is mounted on top of a sample plate. The stamp is mounted on a xyz stage.

4.1.3.2 PET method

A schematic illustration of the PET method is shown in Figure 4.5. PET is essentially a flexible sheet of plastic that becomes more adhesive at higher temperatures compared to at room temperature. We first cut the PET into a small piece (about 2 mm $\times$ 2 mm), remove the protective films, and secure it near one end of a glass slide by taping down the edges of the PET with double sided tape. We call this glass slide the 'PET stamp'. Next, we secure the top hBN sample onto the sample plate of the transfer stage using an extra-strength double-sided tape or a vacuum chuck. We then secure the PET stamp to the stamp holder and move the xyz stage to view the bottom surface of the PET (surface closest to the hBN sample). We pick out a clean spot on the PET and align its location with the hBN flake so that they are directly on top of each other but not touching. Then, we press down the PET stamp onto the monolayer until the entire surface of the PET covers the monolayer substrate. The heater temperature is raised to 50 °C and the PET is laminated for about 2

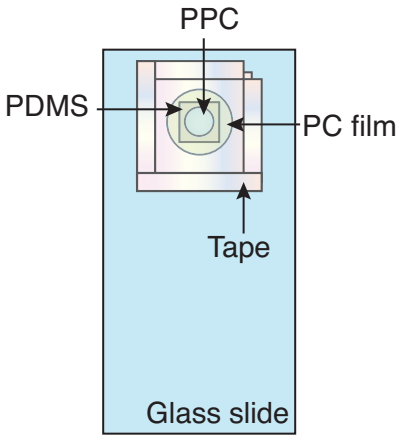

Figure 4.6: Components of the PC stamp.

minutes. Then, we lift up the stamp as slowly as possible using the z micro-manipulator. The top hBN layer sticks to the PET and is lifted off from the substrate.

Next, we remove the hBN substrate and load the monolayer sample onto the sample plate. Under the microscope, we align the top hBN and the monolayer so that they are directly on top of each other but not touching. The PET stamp is lowered onto the monolayer substrate, laminated, and lifted up using the aforementioned procedure. This procedure is repeated until the desired sample stack is complete.

Lastly, the sample is transferred onto a target final substrate. The PET stamp containing the sample stack is lowered and pressed onto the substrate and laminated at 100 °C for 3 to 5 minutes. The goal is to release the PET from the glass slide onto the target substrate. Then the stamp is slowly raised up and out of the way, leaving the PET on the substrate. Once the sample cools, it is soaked in dichloromethane (DCM) for a minimum of 2 hours to dissolve the PET away. Afterwards, the sample is rinsed in an isopropyl alcohol (IPA) bath for 5 minutes and then air-dried.

4.1.3.3 PC method

The basic principles of the PC method is similar to the PET method but the key difference is in the stamp. The PC stamp is dome-shaped which offers several advantages over the flat PET stamp. First, the contact area between the dome-shape stamp and the substrate is small and circular. This minimizes the excessive bulk flakes picked up during the transfer process and the contact area between the polymer and the substrate, keeping the substrate clean. Additionally, the dome-shaped polymer acts as a lens and makes it easier to view the 2D material flakes underneath the stamp during the transfer process.

An illustration of the PC stamp is shown in Figure 4.6. To make the stamp, we first

need to make the PC film. The PC solution is made by dissolving 6% of PC polymer (Alfa Aesar), by weight, in chloroform (i.e. PC/(PC + chloroform)). A magnetic stirrer can be used to speed up the dissolving process. When the solution is well mixed, we use a clean pipette to put a few drops of the solution onto a clean, premium glass slide (Fisher Scientific). Another clean glass slide is placed directly on top of the first one and gently slid apart to coat a thin layer of the PC solution onto both glass slides. Alternatively, we can coat the slides individually using a spin coater. The coated glass slides are then baked on a hot plate at 180 °C for 3 minutes. The remaining PC solution can be stored in an amber glass bottle with a tight fitting lid for up to few weeks, or until the chloroform evaporates and alters the consistency of the solution. The prepared PC film is cut into a 1 cm $\times$ 1 cm square using a clean razor blade in preparation for the stamp. It is important to ensure all of the PC squares are clean and free of dust or wrinkles.

Next, we prepare a polypropylene carbonate (PPC) solution by mixing 18% PPC polymer (Alfa Aesar) in anisole by weight (i.e. PPC/(PPC + anisole)). We use a magnetic stirrer to mix the solution and store it in an amber glass bottle until ready to use.

To make the base of the stamp, we first prepare the PDMS base by cutting a piece of thick, commercial PDMS (Gel-Pak X4 17 mils) into a 0.5 cm $\times$ 0.5 cm square. Then, we peel the clear polyester substrate from it and place the PDMS near one edge (length-wise) of a clean, premium glass slide. Then the polyethylene coversheet is removed from the PDMS. Using a clean razor blade, we further cut down the PDMS into a 1.5 mm $\times$ 1.5 mm square. Using a pipette, we put a drop of the PPC solution on top of the PDMS and then bake it at 110 °C for 3 minutes. This drop of PPC creates the dome-shape on the stamp.

Finally, the PC film is placed on top of the stamp base. A 1 inch (2.54 cm) wide Scotch Tape is cut into about 2 inches (5 cm) in length. The ends of the tape are folded over itself about 0.25 inches (0.6 cm) to make handling easier. Using a hole puncher or a razor blade, we create small circle (diameter of 3 - 4 mm) in the middle of the tape. We place the tape, sticky side down, onto the prepared PC film square, making sure the circle is centered on the square. Using a flat, soft tip tweezer, we carefully press down the tape to increase the adhesion of the tape with the PC, making sure not to touch the exposed PC film. The tape is slowly lifted up and peels off the PC from the glass slide. We place the tape, PC side down, directly on top of the PDMS/PPC stamp, sealing the edges with soft tip tweezers. The excess tape is removed with a razor blade and shaped into a square about 1.2 cm $\times$ 1.2 cm large. Next, we cut four thin strips of Scotch tape, about 0.5 cm wide and 2.5 cm long. We use the strips of tape to seal the edges of the stamp. If the stamp will be used inside of a glovebox, it is important to leave a small corner of it unsealed, to make sure the PC film does not wrinkle during the pump down and backfill cycles.

Next, we discuss the encapsulation and transfer procedure using the PC stamp. The basic idea of the transfer is identical to that of the PET method (Figure 4.5). Using the transfer stage, we slowly press down the PC stamp onto a clean area of the sample substrate to find the contact point. If the contact point is not circular or if the stamp is dirty or wrinkly, the stamp is discarded and a new stamp is used. We align the contact area near the sample that needs to be picked up and slowly press the stamp down to cover the sample. The heater temperature is raised to 50 °C if using hBN and 45 °C if using TMDC monolayer. We laminate the stamp for 1 minute and gently lift up the stamp to pick up the sample. This procedure is repeated until the sample stack is complete. To transfer the sample onto a target substrate, we find a clean area of the substrate and press the stamp down until most of the stamp is contacting the substrate. Then, we raise the heater temperature to 180 - 190 °C and wait until the entire stamp is contacting the substrate (about 3 - 4 minutes). Afterwards, the stamp is slowly lifted up until the PC starts to break and contract towards the center of the stamp. The stamp automatically releases due to the force of the contraction, and the PC film should be dropped down onto the substrate. The PC is then rinsed off in a chloroform bath for 5 minutes and then in an IPA bath for 3 minutes. Once the sample is dries it is ready for use.

Note that a similar method can be used to make a PPC stamp, by using a thin film of PPC instead of PC.

4.2 Heterobilayer sample preparation

Heterobilayer sample preparation shares some similarities with the monolayer sample preparation (section 4.1). In fact, the encapsulation, stacking, and transfer process is identical to the ones mentioned in section 4.1.3. As mentioned in section 2.2, large twist angle between two monolayers cause momentum valley mismatch in heterobilayers. Therefore, heterobilayer preparation requires additional steps to identify and align the crystal axes of the commensurate layers. In this section, we introduce the second harmonic generation spectroscopy for identifying crystal axes in TMDCs and discuss the procedure for rotationally aligning the heterobilayers.

4.2.1 Second harmonic generation spectroscopy

The SHG signal of a material is sensitive to its crystal symmetry and can therefore provide information about the orientation of the TMDC monolayers. Here, we present the theory behind SHG and discuss the experimental setup.

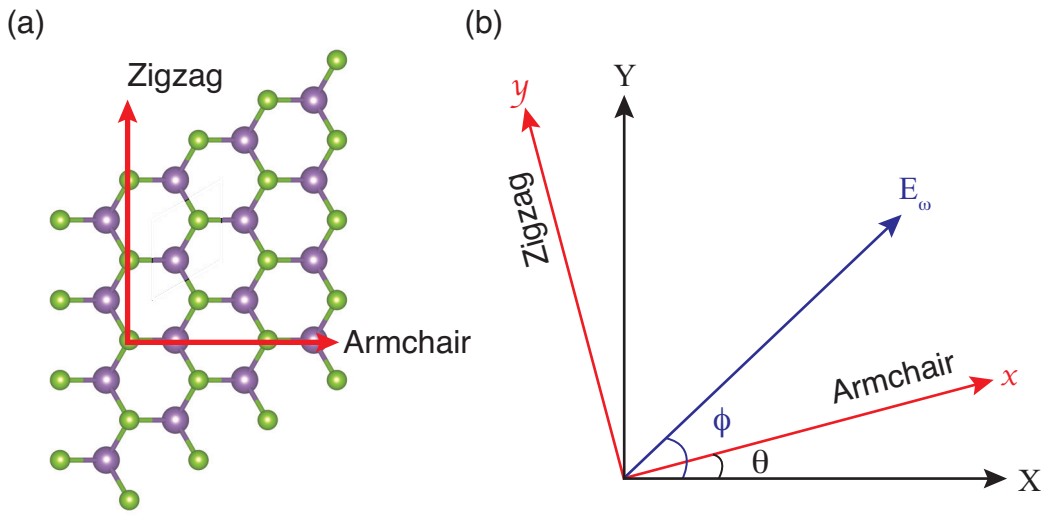

Figure 4.7: SHG coordinates. (a) Armchair and zigzag directions of 2D materials. (b) Coordinate system of the SHG

4.2.1.1 Theory

The derivation presented in this section is adapted from [134, 135]. First we define the lab coordinate system and define the armchair direction, the zigzag direction, the incident electromagnetic vector and the relative angles as shown in Figure 4.7. Polarization induced in a dielectric material by an optical electrical field can have nonlinear terms and can be expressed as a Taylor series expansion. The second term in this series describes the second order nonlinearity. In the frequency domain, the general second order term of the polarization is:

$$P^{(2)}(\omega) = \epsilon_0 \, \chi^{(2)}_{ijk} \, E_j(\omega_1) E_k(\omega_2), \tag{4.1}$$

where ϵ_0 is the vacuum permittivity, $\chi^{(2)}_{ijk}$ is the second order nonlinear optical susceptibility tensor, and $E_j(\omega_1)$ and $E_k(\omega_2)$ are electrical field components of two optical fields. SHG occurs when two incident fields with the same frequency gets converted into a field with twice that frequency:

$$P^{(2)}(2\omega) = \epsilon_0 \, \chi^{(2)}_{ijk} \, E_j(\omega) E_k(\omega). \tag{4.2}$$

The symmetry of the crystal determines the susceptibility tensor. Monolayer TMDCs have the following non-zero susceptibility tensor elements: $\chi^{(2)} = \chi^{(2)}_{xxx} = -\chi^{(2)}_{xyy} = \chi^{(2)}_{yyx} (= \chi^{(2)}_{yxy})$ determined by the D_{3h} point-group symmetry. In the matrix format, the SHG polar-

ization is:

$$\begin{pmatrix} P_x^{2\omega} \\ P_y^{2\omega} \\ P_z^{2\omega} \end{pmatrix} = \epsilon_0 \, \chi_{xxx}^{(2)} \begin{pmatrix} 1 & -1 & 0 & 0 & 0 & 0 \\ 0 & 0 & 0 & 0 & 0 & -1 \\ 0 & 0 & 0 & 0 & 0 & 0 \end{pmatrix} \begin{pmatrix} E_x^\omega E_x^\omega \\ E_y^\omega E_y^\omega \\ E_z^\omega E_z^\omega \\ 2E_y^\omega E_z^\omega \\ 2E_x^\omega E_z^\omega \\ 2E_x^\omega E_y^\omega \end{pmatrix}. \tag{4.3}$$

Note that this is the reduced form of the susceptibility where the coefficients d_{ijk} of the susceptibility follow: $d_{ijk} = d_{ikj}$. The x (y) direction is along the armchair (zigzag) direction of the monolayer crystal. Assuming a normally incident light, the incident wave has the form:

$$E_\omega = \cos(\phi)\boldsymbol{i} + \sin(\phi)\boldsymbol{j}, \tag{4.4}$$

where $\boldsymbol{i}$ and $\boldsymbol{j}$ are unit vectors along the lab coordinates X and Y, respectively. Applying the SHG theory, we obtain the total SHG intensity:

$$I_{\text{SHG}} = A\,[\cos^2(3\theta - 2\phi)\cos^2(\zeta) + \sin^2(3\theta - 2\phi)\sin^2(\zeta)], \tag{4.5}$$

where ζ is the angle of the analyzer (linear polarizer). When the analyzer angle is $\zeta = 0^\circ$ and $\zeta = 90^\circ$, the intensity is:

$$I_X = \cos^2(3\theta - 2\phi) \tag{4.6}$$

$$I_Y = \sin^2(3\theta - 2\phi). \tag{4.7}$$

As the sample is rotated, the SHG intensity detected after the analyzer sketches out a six fold flower pattern. If the polarization of incident light and the analyzer are parallel with one another, the intensity of the detected light is fitted using the function $I_{\text{SHG}} = \cos^2(3\theta - 2\phi)$, and as the sample is rotated, the polar plot of the intensity follows a six-fold flower pattern where the 'lobes' line up with the armchair direction of the monolayer crystal.

4.2.1.2 Experimental setup

There are several different configurations of the SHG setup. To collect the angle-dependent SHG intensity, either the sample or the incident light can be rotated. Practically, rotating

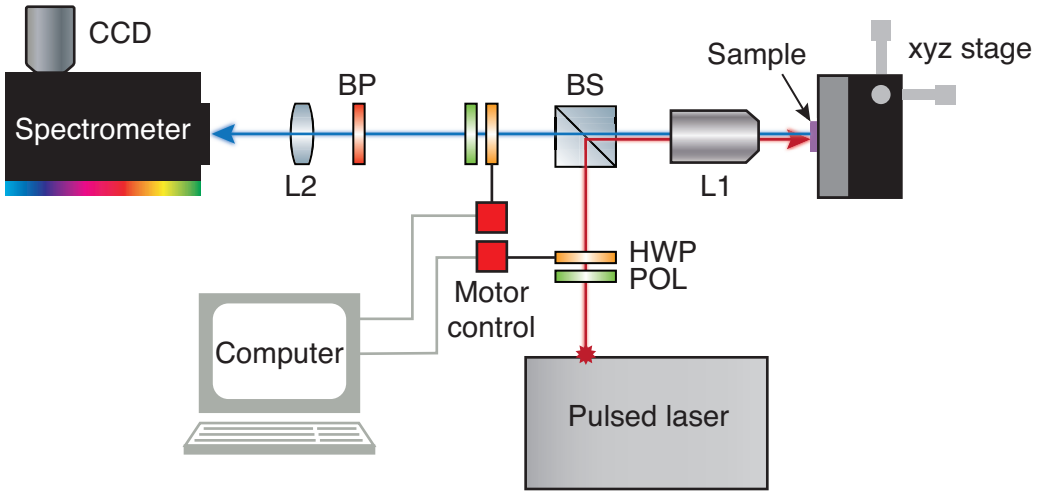

Figure 4.8: SHG experimental setup. POL is a polarizer, HWP is a half waveplate, BS is a beamsplitter, L1 is an objective lens, BP is a bandpass filter, and L2 is the imaging lens.

the sample poses some challenges because the sample could shift laterally during the rotation unless it is placed precisely near the center axis of the rotational stage. Therefore, it is often more convenient to use a motorized half waveplate (HWP) to rotate both the incident light and the analyzer simultaneously. The SHG setup can have the transmission geometry or the reflection geometry. Transmission geometry can be better for measuring a symmetric 6-fold flower pattern as it requires fewer optical components that could introduce polarization aberrations. However, due to the space and resource constraints, we used a reflection geometry, which still works well when aligned properly.

A schematic diagram of the SHG measurement setup is shown in Figure 4.8. Vertically oriented Glan-Taylor polarizers are in the incident path (Thorlabs GT10-B) and in the collection path (Thorlabs GT10-A). HWPs are located in the incident (Thorlabs AHWP05M-980) and collection (Thorlabs AHWP05M-600) paths and are used to rotated the incident laser light and the SHG signal. The first HWP rotates the incident light by 2θ, where θ is the angle of the HWP with respect to the incident polarizer. The second HWP rotates the SHG signal back to vertical orientation and the light passes through the collection polarizer. Both HWPs are mounted on a motorized precision rotation mount (Thorlabs KPRM1E) and controlled using a software program to ensure they rotate simultaneously. The incident light is a 800 nm pulsed laser light from a Ti:sapphire laser mode-locked at 80 MHz. The SHG signal wavelength is 400 nm, and we collect it using a variable bandpass filter (Semrock TBP01-438/16) set to 400 nm.

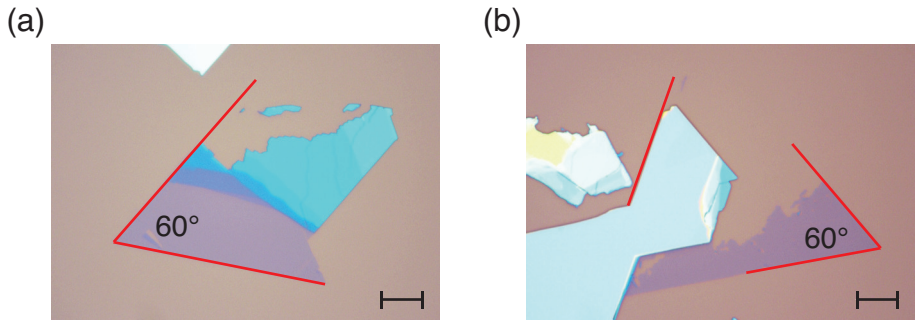

Figure 4.9: Crystal axis identification using optical microscope images. (a) and (b) are images of exfoliated WSe_2 flakes. The red lines are 60 degrees with respect to one another. The scale bar is 10 μm.

4.2.2 Rotational alignment and transfer

Once we determine the crystal axis orientation using the SHG measurement, we form the heterobilayer using rotational alignment and transfer techniques. First step is to design the sample and carefully plan out each step of the stacking and transfer processes. To do this, we use Microsoft Powerpoint or Adobe Illustrator to trace the outline of each layer from its microscope image. Then, we position and overlay the outlines to form the final device layout, making sure that the crystal axes of the two monolayers are parallel to each other.

It should be noted that in most cases, it is possible to determine the crystal axis of the monolayer by examining its optical image, even without performing SHG measurements. Most monolayer flakes have two straight edges that are 60 degrees from each other. Since the crystals naturally want to tear along the armchair direction, when we spot two or more straight edges that are multiples of 60 degrees from each other, there is an extremely high likelihood that the edges are aligned along the armchair direction. Figure 4.9 shows images of the crystal axes determined by microscope images.

Once the design is complete, we use either the PET or PC transfer methods detailed in section 4.1.3 to stack the layers according to the design. When rotationally aligning the two monolayers during the transfer process, we use a rotation mount on the sample stage to change the twist angles. It is often helpful to use the tracing tool on the microscope software to verify that the flakes have the same orientation as in the designed file. The final transfer to the target substrate is identical to the ones used for monolayer encapsulation.

4.3 Microcavity fabrication

There are a myriad of available microcavity designs, but in this thesis we focus on three main methods, namely the transferrable DBR cavity, the photonic grating cavity, and the tunable open cavity. These cavities have been used to demonstrate strong coupling and photon lasing in TMDCs and each have their own advantages and limitations. The transferrable DBR cavity can produce a high-Q cavity and is robust against degradation. However, this method requires a clean sample and calibration of the cavity detuning. The photonic grating cavity has a simple design which makes it easy to fabricate. However, the Q-factor is lower and the grating mode is sensitive to debris and bulk flakes deposited during the transfer process. The cavity length of the open cavity can be tuned during the measurement process. However, it involves a delicate sample mounting procedure and bulky equipment. In this section, we discuss the fabrication and setup procedures for all three of these cavities.

4.3.1 Transferrable DBR microcavity fabrication

In this thesis, we use a DBR stack comprising 9 pairs of 40 nm ZnS/78 nm MgF_2 films and careful control of the fabrication parameters to ensure a clean, uniform film with high reflectivity. It is then exfoliated from the glass substrate using a PDMS handle, and can be cut into small pieces of desired areas of cavity coverage (Figure 4.10(a-c)). The measured and simulated DBR reflection spectra are shown in Figure 4.11.

To assemble the full cavity, we use a bottom DBR comprised of 16 pairs of SiO_2 and titanium dioxide (TiO_2) with a 750 nm center wavelength. The hBN encapsulated $MoSe_2$ was transferred on top of the bottom DBR using a dry transfer technique (Figure 4.10(d)). PMMA with a molecular weight of 950K, diluted in 2% anisole (A2) was spun on top of the sample to control the cavity length (Figure 4.10(e)). Then, the top DBR was transferred on top of the encapsulated sample stack (Figure 4.10(f)). The PDMS handle was lifted off, leaving behind the DBR on top of the sample stack (Figure 4.10(g) and 4.10(h)).

4.3.2 Photonic grating cavity fabrication

The photonic grating cavity is a SiN slab with a sub-wavelength grating bars. All of our gratings were fabricated at the Lurie Nanofabrication Facility. A schematic of the fabrication procedure is shown in Figure 4.12. The SiN slab is grown on top of a SiO_2 buffer layer, which is on top of a Si wafer. The SiO_2 buffer layer protects the grating from the Si absorption. The slab can be grown using a low-pressure chemical vapor deposition technique either in the cleanroom or through a commercial vendor (LioniX).

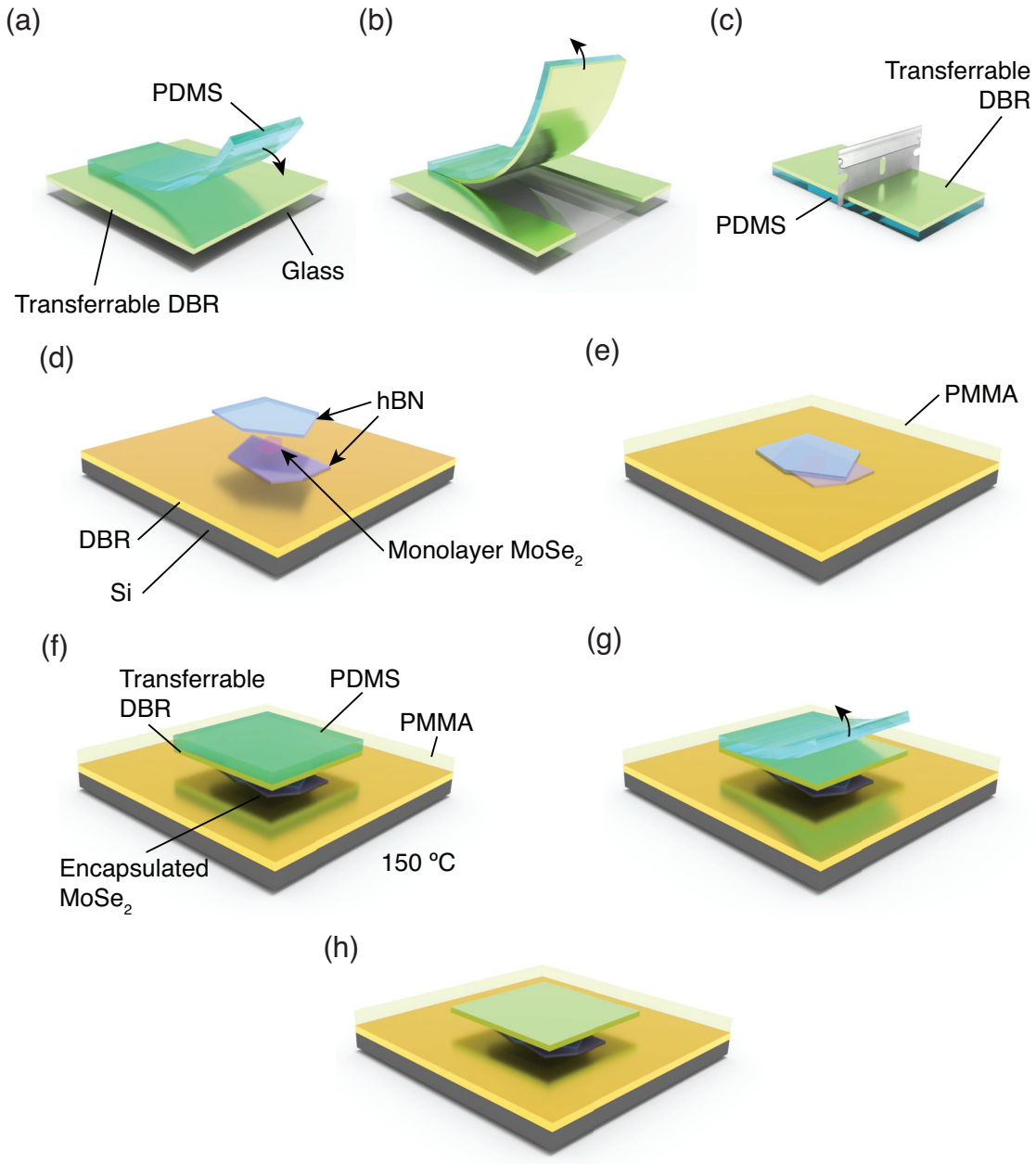

Figure 4.10: Transferrable DBR cavity fabrication process. (a-c) ZnS/MgF_2 DBR exfoliation procedure. (a) PDMS sheet is brought into contact with the transferrable top DBR on a glass substrate. (b) The PDMS sheet is lifted to peel off a segment of the top DBR. (c) The peeled off top DBR is cut into a small piece. (d-h) Sample fabrication procedure. (d) hBN Encapsulated $MoSe_2$ sample is stacked on top of the bottom DBR. (e) PMMA is spin-coated on top of the encapsulated $MoSe_2$ sample. (f) A small piece of top DBR is placed on top of the encapsulated $MoSe_2$ sample and heated to 150 °C. (g) The PDMS layer is peeled off and the top DBR adheres to the PMMA. (h) The completed sample.

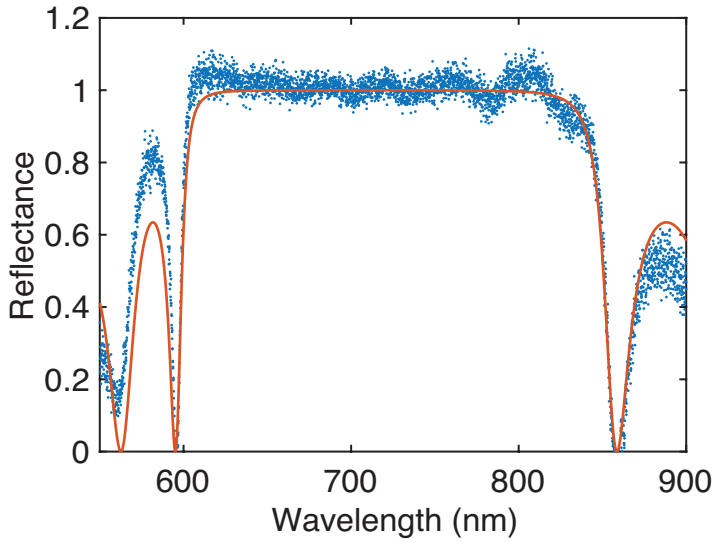

Figure 4.11: Transferrable DBR reflection spectrum. Transfer matrix simulated (red solid line) and measured (blue dots) reflection spectrum of the ZnS/MgF_2 transferrable DBR.

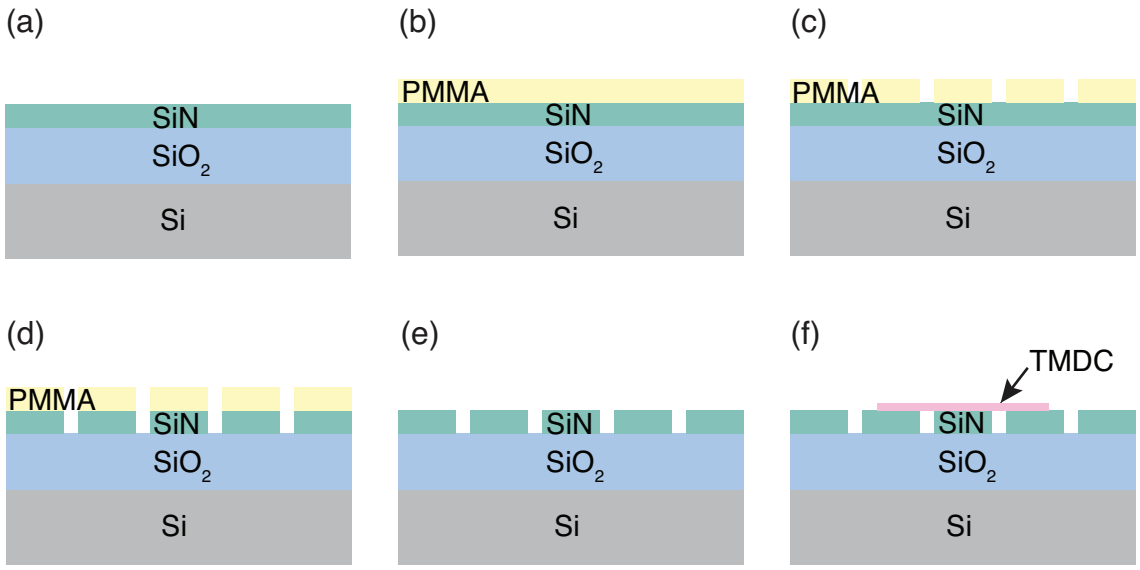

Figure 4.12: Photonic grating fabrication procedure. (a) SiN slab on a SiO_2 and Si substrate. (b) PMMA is spin coated on top of the SiN slab. (c) PMMA is patterned by EBL. (d) SiN is etched using RIE. (e) PMMA is cleaned off by oxygen plasma cleaning. (f) TMDC sample is transferred on top of the grating.

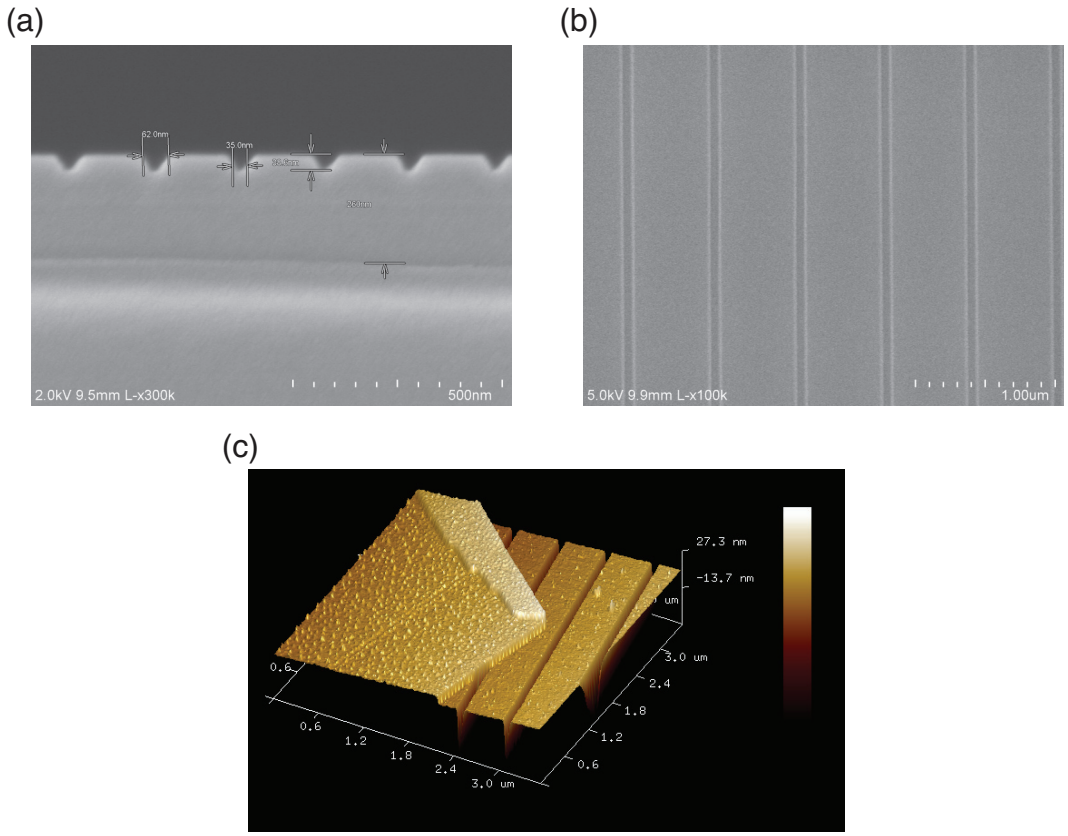

Figure 4.13: Photonic grating SEM and AFM images. (a) Cross-section SEM image of the grating. (b) Top-down SEM image of the grating. (c) AFM image of the grating profile. hBN layer is on top of the grating.

To pattern the grating, we use EBL. First, we design the grating using a software called KLayout. Then, we prepare the SiN substrate by cutting it into a piece about 2 cm $\times$ 2 cm large. If the substrate is dirty, it is cleaned using oxygen plasma or an acetone bath followed by an IPA rinse. The PMMA A4 resist is coated onto the substrate using a spin coater at 4000 rpm for 45 seconds. The resulting PMMA thickness is around 200 nm. We bake the substrate at 180 °C for 3 minutes. Next, we pattern the resist using EBL (JBX-6300FS), according to the design file. Afterwards, we develop the exposed resist by soaking the sample a 3:1 ratio of IPA to methyl isobutyl ketone (MIBK) for 90 seconds followed by an IPA soak for 60 seconds.

Next, we etch the exposed parts of SiN using RIE, which uses plasma gas to etch away the exposed parts of the sample wafer. After etching, we clean the PMMA resist off using oxygen plasma cleaning. The grating etching depth and speed are determined by the the RIE parameters and the feature size of the grating. If the etching rate is too fast, the grating can be over-etched or have rough side walls, which lowers the cavity Q-factor. Therefore, it

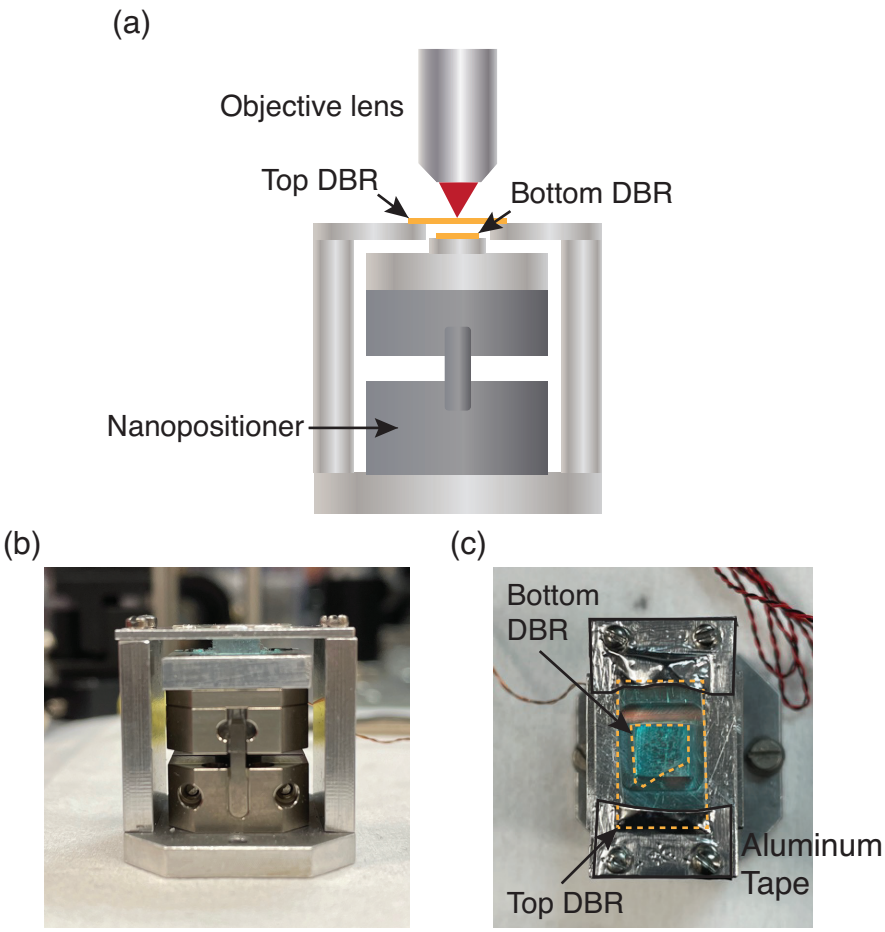

Figure 4.14: Open cavity setup. (a) Schematic of the open cavity. (b) Side-view image of the open cavity setup. (c) Top-view image of the open cavity setup. The dashed line outlines the top and bottom DBRs, and the solid line outlines the aluminum tape.

is important to fine-tune and optimize the parameters. The grating depth can be measured two different ways: by imaging the cross section using SEM, or by AFM (Figure 4.13). Using these metrology tools in addition to the reflection measurement, we can characterize the grating and iterate the fabrication recipe, as needed.

4.3.3 Tunable open cavity setup

The tunable open cavity setup consists of a fixed top DBR and a tunable bottom DBR mounted on a linear nanopositioner. Here, we present the open cavity setup and present preliminary, unpublished data demonstrating strong coupling of monolayer $MoSe_2$.

A schematic illustration of the open cavity setup is shown in Figure 4.14. The nanopositioner is the Attocube ANPz51/LT, which has a sub nanometer resolution. The top DBR must have a transparent substrate and is mounted on a fixed metal frame. In order to achieve

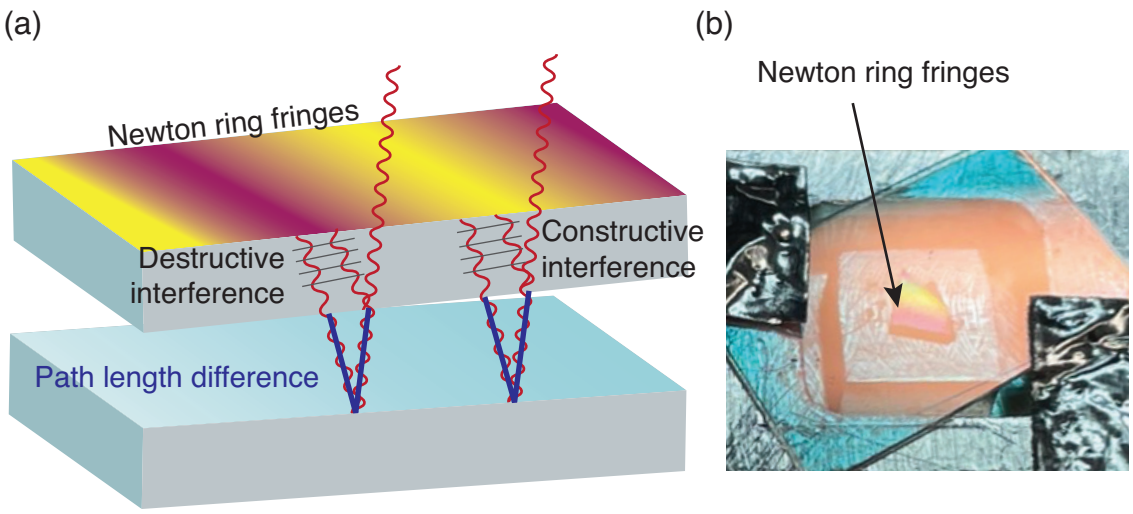

Figure 4.15: Newton rings in the open cavity. (a) Schematic of Newton rings between two DBR mirrors. There is a slight tilt between the two mirrors. Constructive interference creates bright fringes and destructive interference creates dark fringes. (b) Image of Newton rings fringes.

small cavity length and a high Q-factor, the two mirrors must be perfectly parallel to each other. In experiments, it can be challenging to align the two mirrors to be parallel because there are tilts introduced by various components of the sample stage. A motorized tilt stage can help alleviate this issue, but this can be very costly. To figure out how to align the mirrors, we attempted several different mirror mounting methods. The goal was to find a way to secure the top mirror just enough so it would stay in place during measurements yet flexible enough to change its tilt when the bottom mirror pushes against it. After testing different adhesive materials, such as silver paint, wide and narrow aluminum tapes, clear nail polish and wide and narrow Kapton tapes, we determined that thick aluminum tape resulted in the smallest cavity length. An image of the cavity is shown in Figure 4.14(b) and 4.14(c).

The DBR mounting procedure is as follows: first, the bottom DBR is cleaned with acetone and IPA in an ultrasonic bath to remove as much dust and particles from the DBR as possible because they can increase the cavity length. Then, the bottom DBR is secured onto the bottom sample stage using silver paint. Then, the top DBR is placed onto the top sample plate, DBR side down. The nanopositioner stage is raised slowly until the bottom DBR contacts the top and fringes are visible. These fringes are Newton rings caused by constructive and destructive interference of light in the tilted mirror (Figure 4.15). Next, we find try to minimize the number of fringes by tuning the nanpositioner or nudging the top DBR to change its tilt. When we roughly determine the top DBR configuration that results

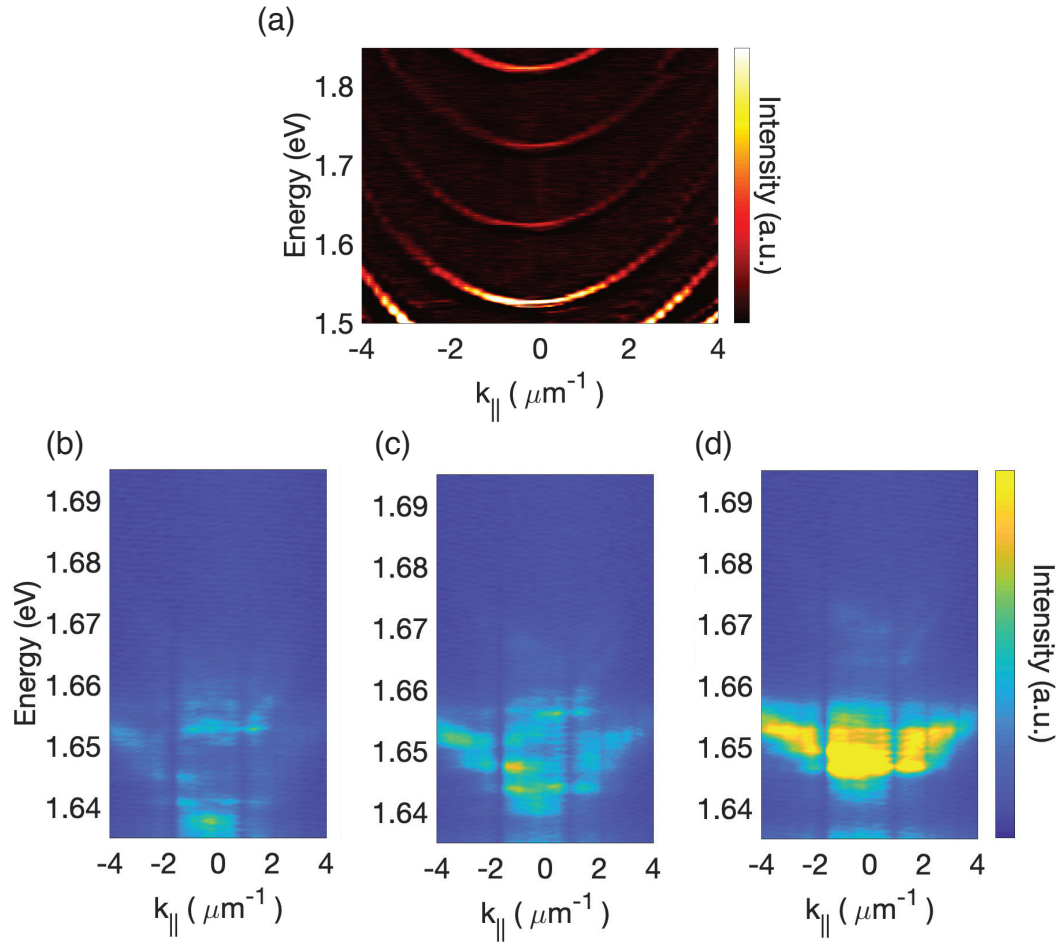

Figure 4.16: Open cavity reflection and PL spectra. (a) Angle-resolved reflection spectrum of the open cavity modes. (b-d) Angle-resolved PL spectra of the open cavity coupled with an encapsulated $MoSe_2$ at different detunings. (b) Negative detuning, (c) near-zero detuning, and (d) positive detuning.

in a minimum number of fringes, we lower the nanopositioner and use a wide aluminum tape (about 1 cm wide) to tape down the mirror and create small 'pockets' on other side of the DBR where the tape does not touch it. This gives the mirror some wiggle room to move around slightly to become parallel to the bottom mirror.

Then, we perform a room temperature angle-resolved reflection measurement (see section 4.4 for details) to characterize the cavity. To estimate the cavity length, we measure the mode spacing near the center of the DBR stop band. For Fabry-Perot etelons with normally incident light (incident angle $\theta = 0$) and cavity length d, the following condition applies

for two adjacent modes with wavelengths λ_1 and λ_2:

$$\begin{aligned} 2d &= m\lambda_1 \\ 2d &= (m+1)\lambda_2, \text{ where } m = 1, 2, 3, \cdots . \end{aligned} \tag{4.8}$$

Therefore, the cavity length can be written as:

$$d = \frac{\lambda_1 \lambda_2}{2(\lambda_1 - \lambda_2)}. \tag{4.9}$$

The minimum cavity length we measured is around 2.15 μm, both at room temperature and at cryogenic temperature. The variation of cavity length across the DBR is around 1 μm. For low-temperature measurements, we use the Attocube attodry 1000 cryostat, which has a vertical sample mount and a top-down optical access port, which makes open cavity measurements easier. Figure 4.16(a) shows the cavity reflection spectrum.

To fabricate polariton devices using open cavity, we use the PC transfer technique (section 4.1.3) to transfer an encapsulated monolayer onto the bottom DBR because the PC technique produces clean samples with minimal residue, which is important for minimizing the cavity length. Figure 4.16(b-d) shows low-temperature PL spectra of an encapsulated monolayer $MoSe_2$ polariton device measured at different cavity detunings.

4.4 Optical measurements

Optical spectroscopy is the primary method of characterizing and investigating excitons, cavity modes, and exciton-polaritons. In this section, we present the spectroscopy techniques used for this thesis work.

4.4.1 Real-space and angle-resolved spectroscopy

PL and reflection measurements are used to characterize the emission and absorption properties TMDC devices. For quick characterization, we perform real-space (or angle-integrated) spectroscopy. For cavity or exciton-polariton characterizations, we need to measure the dispersion relation using angle-resolved spectroscopy. Real-space imaging gets its name because the image that is created on the spectrometer is a magnified version of the sample emission in real-space. Emission from one spot on the sample, regardless of its emission angle, gets focused on the same spot of the spectrometer. Angle-resolved imaging on the other hand, focuses all of the light emitted from the same angle onto a single spot. This is also known as Fourier-space imaging (or k-space imaging). A schematic illustration of

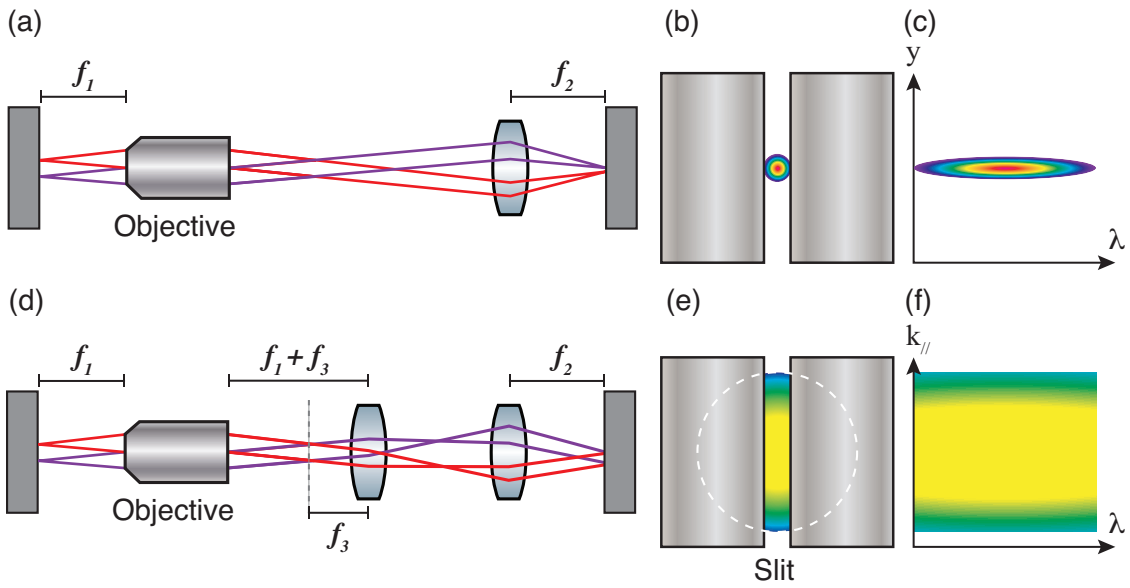

Figure 4.17: Principles of real-space and Fourier-space spectroscopy. Schematic of the (a) real-space and (d) Fourier-space imaging setups. (b) Real-space and (e) Fourier-space images on the slit of the spectrometer. (c) Real-space and (f) Fourier-space spectra on the spectrometer.

real-space and Fourier-space imaging is shown in Figure 4.17. In real-space imaging, light is focused on the sample plane by an objective lens, and the reflected/emitted light forms a Fourier image (or the far-field image) on the back focal plane of the objective lens. The imaging lens re-focuses the light back to the real-space image. In Fourier-space image, a lens with focal length f is placed a distance f from the back focal plane of the objective lens. Therefore, the Fourier image is measured by the spectrometer. To gain spectral resolution from the image, the spectrometer slit is closed and the resulting strip of image is dispersed by a grating onto a charge-coupled device (CCD).

A diagram of the optical setup used in this thesis is shown in Figure 4.18. For PL measurements, we use a laser light source, either a Ti:Sapphire cw (Spectra-Physics Tsunami) or pulsed (MSquared Solstis) lasers, or diode lasers (532 nm or 633 nm). For reflection measurements, we use a fiber-coupled broadband white light source (Thorlabs SLS201L), or a fiber-coupled supercontinuum laser (NKT photonics SuperK EXTREME). The spot size of the white light source is around 10 μm and the supercontinuum laser is around 2 μm. If the sample area is smaller than 10 μm $\times$ 10 μm, we can use a supercontinuum laser or spatial filtering. Spatial filtering uses a pinhole placed on the real-space confocal plane of two lenses to only pass through certain spatial frequency components of light. Low-temperature measurements are performed using a closed-cycle cryostat (Montana Instruments Fusion 2). For quick imaging of the sample during measurement, we use a

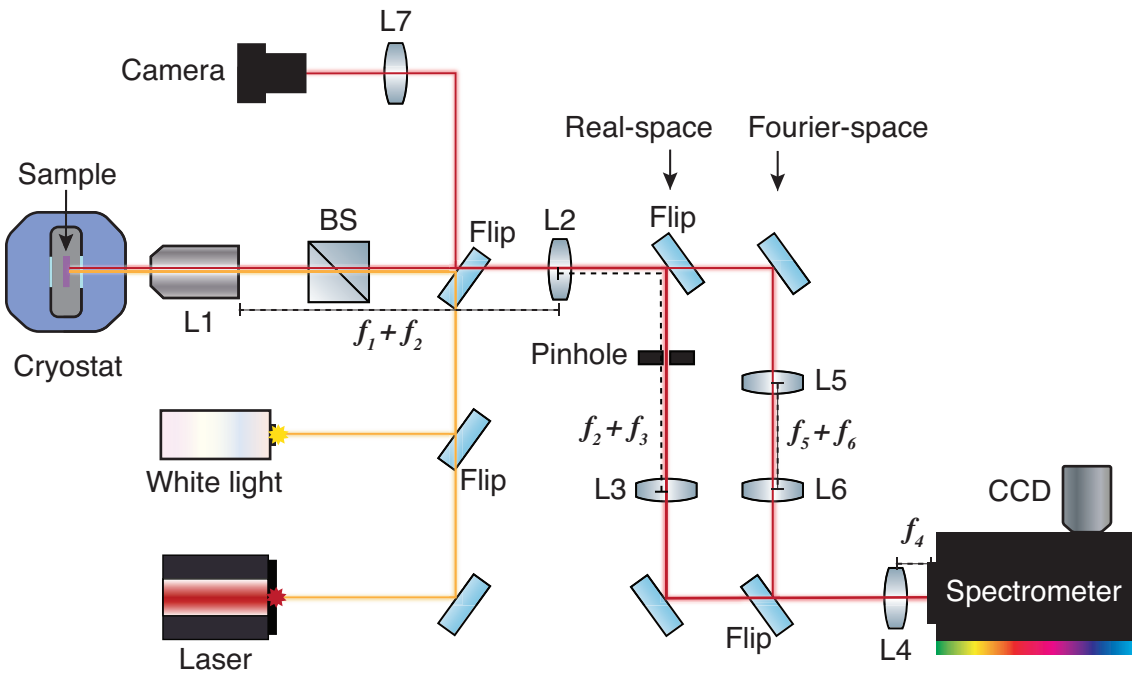

Figure 4.18: Real-space and Fourier-space spectroscopy experimental setup. L1 is the objective lens, L2 and L3 are confocal lenses, L2, L5, and L6 are Fourier-space relay lenses, L4 is the imaging lens for the spectrometer, and L7 is the imaging lens for the imaging camera. f denotes the focal lengths of the lenses.

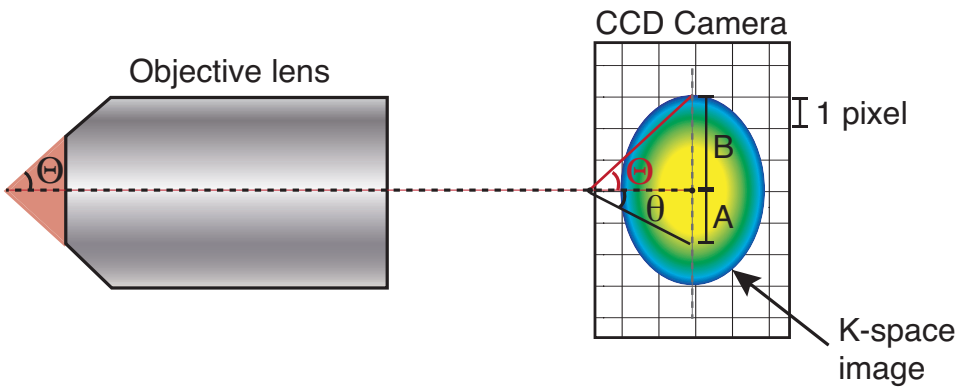

Figure 4.19: Fourier-space imaging geometry.

white light source and expand the spot size to get a wider field of view. The real-space image is sent to a complementary metal-oxide semiconductor (CMOS) camera (Thorlabs DCC1545M). A motorized mirror flip mounts are used to switch from real-space and angle-resolved measurements. The angle-resolved measurement setup has two pathways: one that retains the orientation of the Fourier image and one that rotates it 90°. This setup is used for measuring photonic gratings, which are anisotropic and have different optical modes along the direction of the grating bars versus perpendicular to the grating bars. The final imaging lens is mounted on a motorized linear stage for spatial scanning of the sample. When performing PL measurements, scattered laser light is filtered out using a longpass filter. The spectrometer (Princeton Instruments SP-2500i) has a grating turret and a visible wavelength CCD camera (Princeton Instruments PIXIS256). For typical measurements we use the 600 g/mm grating and for measurements that require good spectral resolution we use the 1200g/mm.

For angle-resolved measurements, the maximum collection angle Θ depends on the numerical aperture (NA) of the objective lens. The NA is:

$$\text{NA} = n \sin \Theta, \tag{4.10}$$

where n is the index of refraction of the space between the objective lens and the sample, which is typically air ($n = 1$). To calculate the angle (θ) of a specific location (y) along the y-axis of the CCD, we consider the geometry shown in Figure 4.19:

$$\frac{\tan\theta}{\tan\Theta} = \frac{A}{B} \tag{4.11}$$

$$\theta = \tan^{-1}\left[\tan\left(\Theta\,\frac{A}{B}\right)\right], \tag{4.12}$$

where A is the distance between the center of the k-space image and y, and B is the radius of the k-space image circle. The in-place wave vector at a given wavelength (λ) is:

$$k_{\parallel} = \frac{2\pi}{\lambda} \sin\theta. \tag{4.13}$$

4.4.2 Time-resolved spectroscopy

Time-resolved spectroscopy gives information about the carrier relaxation dynamics. To perform time-resolved measurements, we send the PL emission into a streak camera (Hamamatsu C5680), which disperses the light using a grating. The emitted light is directed to a photocathode, which excites electrons that propagates towards a phosphor screen. Along the way, a time-varying voltage is applied in the direction perpendicular to the direction of electron propagation. This causes a time-varying deflection (or 'sweeping') of the electrons. The deflected electrons arrive at the phosphor screen, which converts them back into photons. The electron sweeping is synchronized with the excitation laser pulse, which triggers the beginning of the sweeping at the same frequency as the laser pulses. The resulting image of the CCD camera has a time axis along the vertical direction and a space axis along the horizontal direction. Temporal resolution of the streak camera is on the order of a few picoseconds.

4.4.3 Coherence measurements

Lasers have two types of coherence: temporal and spatial. Temporal coherence is a measure of how correlated the phase of light is at different points in time. It measures how monochromatic the light source is. Spatial coherence describes the degree of correlation between light at one location and another location. The first order correlation function between two field amplitudes $\boldsymbol{E}^{+}(\boldsymbol{r}, t)$ and $\boldsymbol{E}(-\boldsymbol{r}, t+\tau)$ can be written as:

$$g^{(1)}(\boldsymbol{r}, -\boldsymbol{r}; \tau) = \frac{\langle \boldsymbol{E}^{+}(\boldsymbol{r}, t)\ \boldsymbol{E}(-\boldsymbol{r}, t+\tau)\rangle}{\sqrt{\langle |E(\boldsymbol{r}, t)|^2\rangle}\ \sqrt{\langle |E(-\boldsymbol{r}, t+\tau)|^2\rangle}} \tag{4.14}$$

To measure the coherence properties, we use a Michelson interferometer setup. A schematic of the setup in shown in Figure 4.20. First, the light is split into two equal paths using a 50:50 beam splitter. At the end of each arm of the interferometer, there is a retroreflector or a mirror. The light from each arm is overlapped and the resulting interference pattern is imaged onto a CCD camera.

For temporal coherence measurements, both arms have a retroreflector. One of the retroreflectors is mounted on a motorized linear stage. The 'time zero' is when both arms

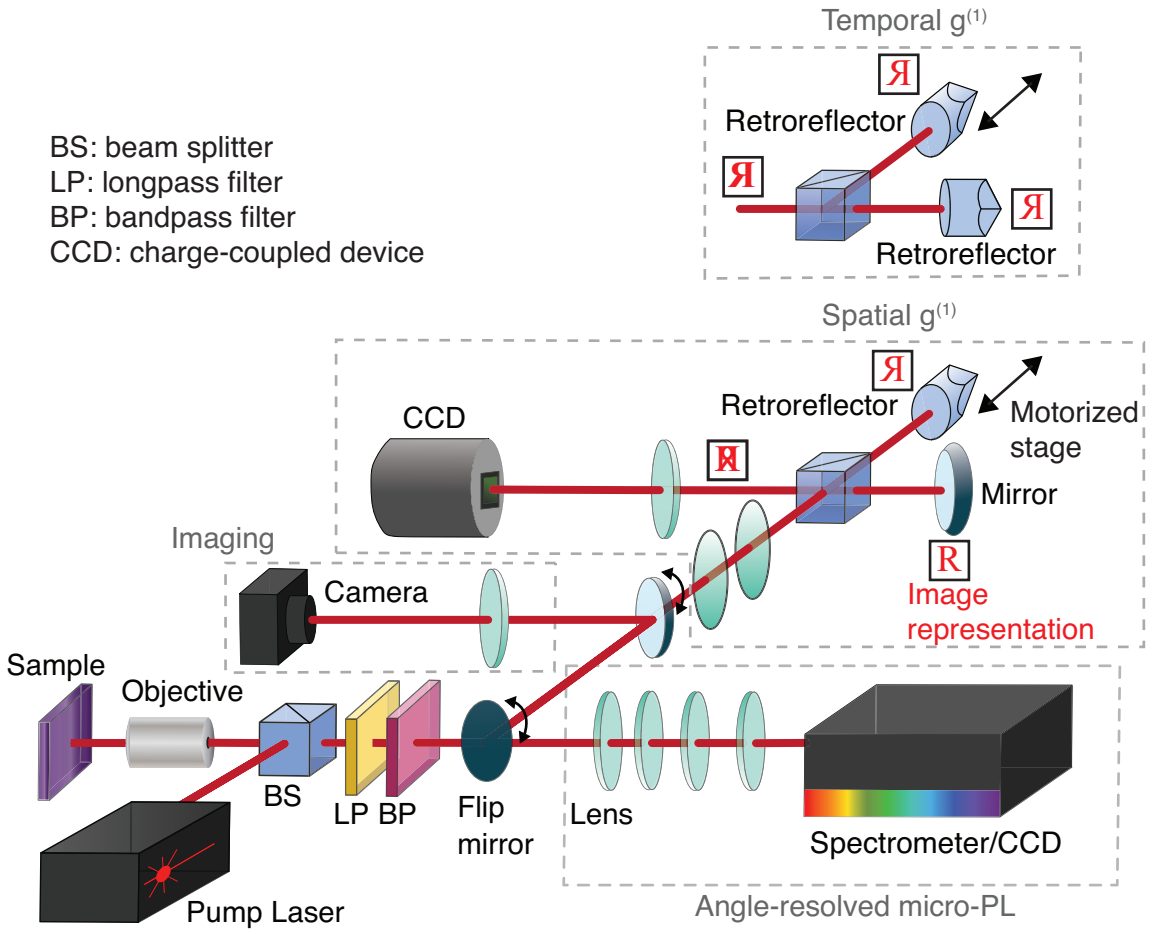

Figure 4.20: Coherence measurement experimental setup.

of the interferometers have the same optical path lengths. To find time zero, we use a reference laser light which has a long coherence time and thus makes the process easier. We scan the motorized linear stage until we start seeing interference friges on the CCD camera. As the two beams from each arm becomes more aligned, the distance between the fringe patterns increases. We move the retroreflector until the distance between the fringes is maximized. Since the reference laser likely has a long coherence time, it could be difficult to visually determine the exact time zero location. Therefore, once we obtain an approximate location of the time zero using a laser, we use the sample PL emission to find the exact time zero.

Once we determine the time zero location, we scan the motorized stage in small increments and collect the interference fringes on the CCD. Moving the retroreflector back by distance L results in a time delay of $\tau = 2L/c$, where c is the speed of light. The coherence time (τ_c) is a value used to quantify the degree of first order temporal phase coherence of the emission. Visibility of interference fringes imaged at CCD can be fitted to obtain $g^{(1)}(\tau)$. By varying τ, we can map out $g^{(1)}(\tau)$ vs. τ. The intensity measured on the CCD is related to $g^{(1)}(\tau)$ in the following way:

$$I^{\text{int}}(x,\tau) = I_1(x) + I_2(x) + 2|g^{(1)}(\tau)|\sqrt{I_1(x)I_2(x)}\cos\left(\frac{2\pi\theta}{\lambda_0} + \phi\right) \tag{4.15}$$

where $I_1(x)$ and $I_2(x)$ are Gaussian intensity profile of the two interfering beams, θ is the angle between the beams, λ_0 is the center wavelength of the laser emission and ϕ is the phase difference. By fitting the interference fringes at each τ, plotting $g^{(1)}(\tau)$ vs. τ and fitting a Gaussian function to it, we can obtain the coherence time τ_c from the Gaussian linewidth.

For spatial coherence measurements, we replace one of the retroreflectors with a planar mirror. For alignment, it is easier to replace the one that is not mounted on the motorized stage. The mirror changes the orientation of the image, which is now centrosymmetrically inverted with respect to the image reflected by the retroreflector. As we scan the motorized stage, the phase difference between the two beams change and the intensity of the image on the CCD undergoes a sinusoidal modulation. This can be fitted with a sinusoidal function to obtain the spatial coherence $g^{(1)}(\boldsymbol{r}, -\boldsymbol{r})$. The intensity of the interference pattern on the CCD can be written as:

$$I^{\text{int}}(\boldsymbol{r}) = I(\boldsymbol{r}) + I(-\boldsymbol{r}) + 2\sqrt{I(\boldsymbol{r})I(-\boldsymbol{r})}\, g^{(1)}(\boldsymbol{r}, -\boldsymbol{r})\, \sin\left(\frac{2\pi}{\lambda_0}(z - z_0)\right). \tag{4.16}$$

$I(\boldsymbol{r})$ and $I(-\boldsymbol{r})$ are intensities from the mirror and retroreflector arms, respectively, and

are measured by blocking one of the arms of the interferometer. z is the position of the retroreflector. $g^{(1)}(\boldsymbol{r}, -\boldsymbol{r})$ is the first order spatial coherence for two positions separated by $2r$, and is proportional to the visibility of the interference fringe. To obtain the visibility or $g^{(1)}(\boldsymbol{r}, -\boldsymbol{r})$, we scan the position z and record the sinusoidal oscillation of $I^{\text{int}}(\boldsymbol{r})$ vs. z at each $\boldsymbol{r}$.

4.5 Electrical devices

Having electrical contacts on TMDC devices adds an extra knob that can be tuned to explore new physics and engineer practical devices. In this section, we discuss the electrical contact fabrication procedures and measurement setup.

4.5.1 Electrical contact fabrication

There are three main methods of electrical contact fabrication that we will discuss in this thesis. The first method uses EBL to directly pattern the contacts. The second method uses photolithography to pattern the contacts in bulk and the sample is transferred on top of the contacts. The third method uses stencil masks to deposit large area contacts. The EBL method is good for making precise contacts but can be time consuming and costly. The photolithography method is fast and cost-efficient but requires careful planning and design of the 2D material sample stack to fit onto the pre-patterned contacts. A schematic illustration of the EBL and photolithography methods are shown in Figure 4.21. The physical mask method is very fast but could expose the 2D materials to more processing steps and is difficult to use for more complicated sample structures. Therefore, we only used this method for initial testing devices.

4.5.1.1 Electron-beam lithography method

For the EBL method, we first need to pattern alignment markers onto a substrate. We make a design file of the markers using KLayout. We use a 4 inch wafer of 90 nm thick SiO_2 for all of our electrical devices. The SPR220 photoresist is spun onto the substrate at 3000 rpm and baked for 90 seconds at 115°C. The resulting resist thickness is around 3 μm. Then, we use direct write lithography (Heidelberg μPG 501) to pattern the photoresist and develop the resist using the AZ726 developer. Next, we use an electron beam evaporator (Angstrom Engineering Evovac) to deposit 5 nm of titanium followed by 200 nm of gold. Last, we lift off the photoresist in an acetone bath overnight (8+ hours) and rinse the substrate with IPA.

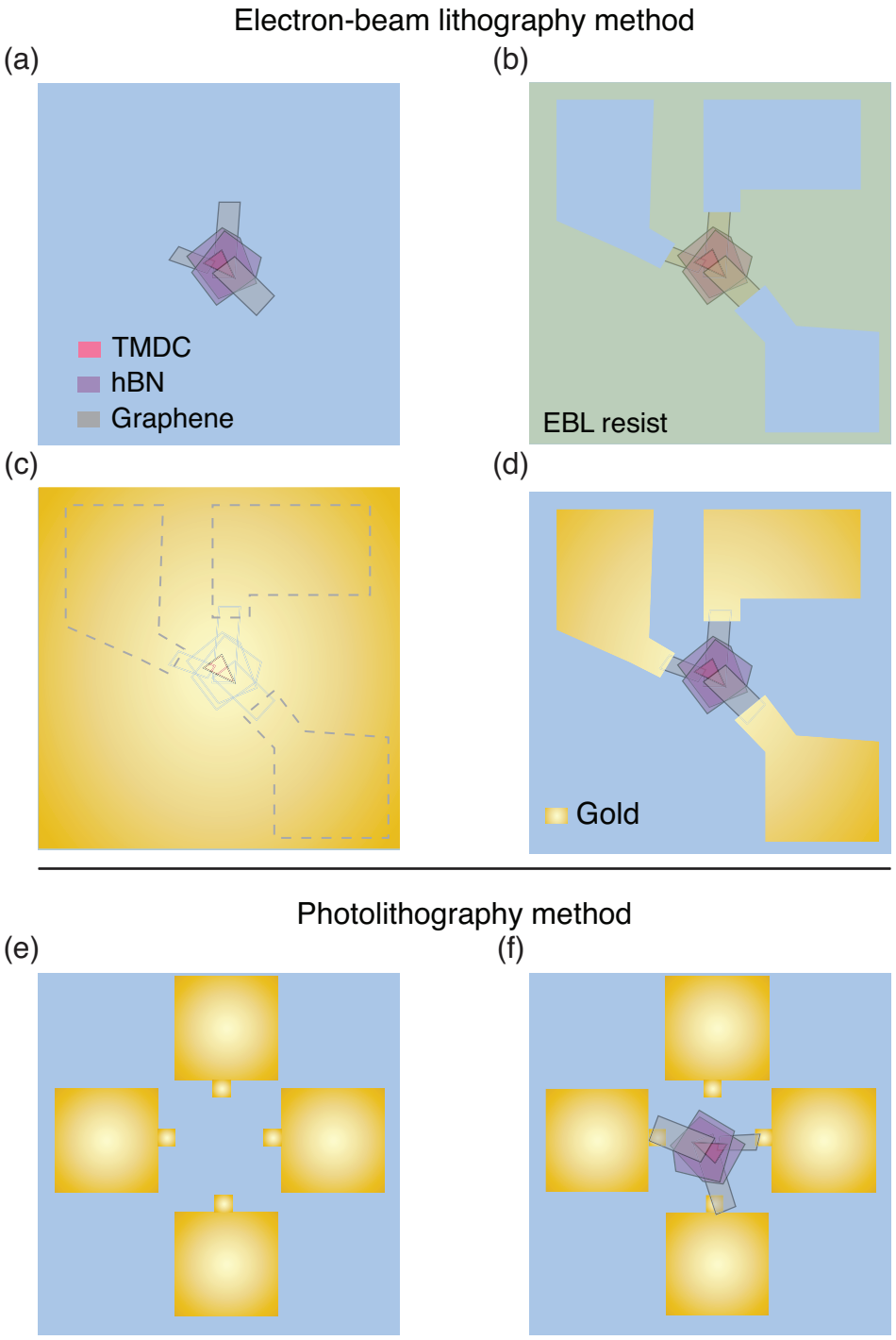

Figure 4.21: Electrical contact fabrication methods. (a) Transferred sample stack. (b) EBL patterned contacts. (c) Gold deposition. (d) Final sample. (e) Pre-patterned contacts. (f) Sample stack is transferred on top of the contacts.

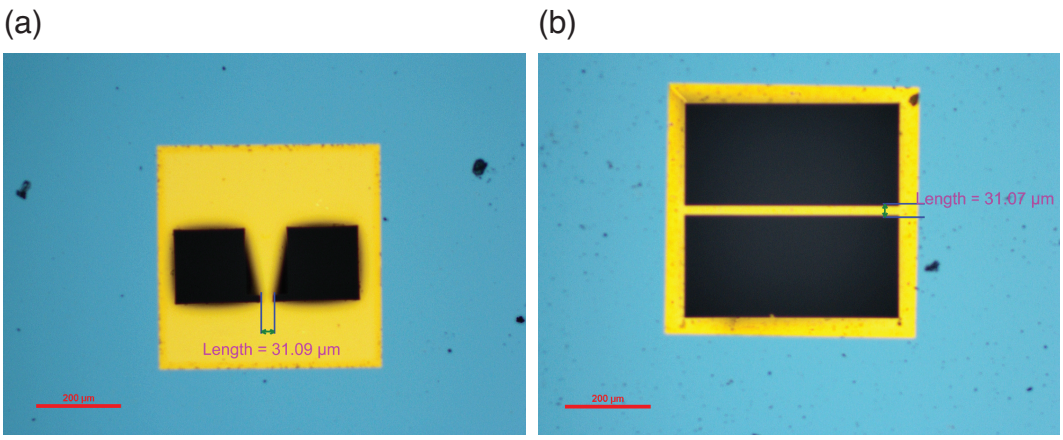

Figure 4.22: Image of stencil masks used to make electrical contacts. (a) and (b) show different configurations.

Now, we exfoliate, design, and transfer a sample stack onto the marked substrate. Few-layer graphene flakes are often used to contact the monolayers and the gold contacts are wired to the graphene. This avoids the PL quenching that can be caused by the gold contacts. Then, we design the gold contacts using KLayout. Using the alignment marker design file and an optical image of the sample stack, we first scale the image appropriately such that the marker sizes and pitch on the image match those in the design file. Then we draw the contacts and set the reference alignment markers. To pattern the contacts, we first spin the PMMA A4 resist onto the sample substrate using a spin coater at 4000 rpm for 45 seconds. We bake the substrate at 180 °C for 3 minutes. We use the SEM mode on the EBL machine to locate and align to the reference markers. Then we pattern the contacts. Afterwards, we develop the exposed resist by soaking the sample a 3:1 ratio of IPA to MIBK for 90 seconds followed by an IPA soak for 60 seconds. The metal layers (5 nm Ti and 200 - 300 nm of gold) are deposited and the photoresist is lifted in an acetone bath and IPA rinse.

4.5.1.2 Photolithography method

The procedure for creating the pre-patterned contacts is identical to that used to create alignment markers for EBL contacts. But instead of alignment markers, we draw a 5-contact pattern. The thickness of the gold layer is only 30 nm because thicker contacts can break the relatively thin 2D materials. We transfer the 2D material stack onto the pre-patterned contacts using the PC transfer method described in section 4.1.3, paying special attention not to short the contacts.

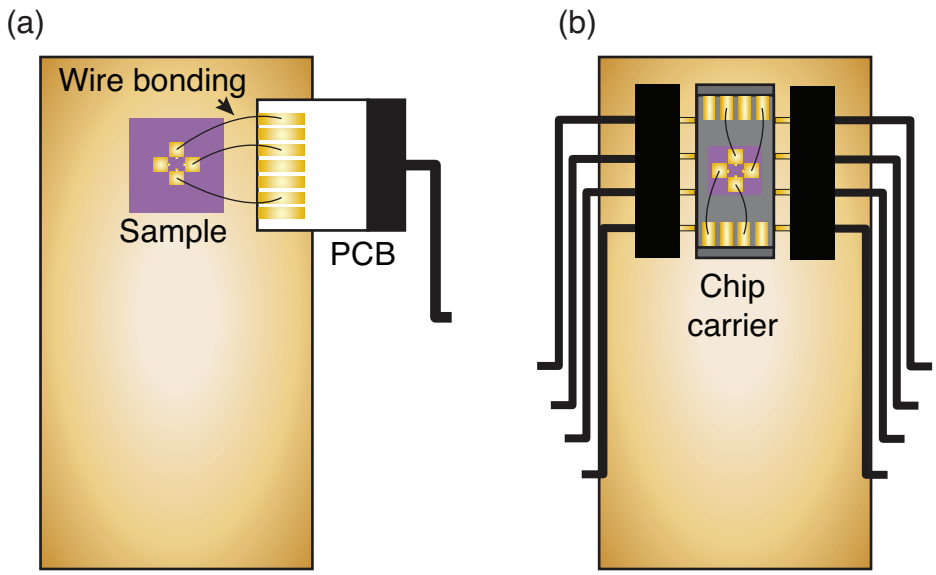

Figure 4.23: Electrical sample carrier designs. (a) The sample is directly mounted onto the cryostat coldfinger. (b) The sample is mounted on a chip carrier, which is connected to a pin socket.

4.5.1.3 Stencil mask method

First, a mask is created using standard photolithography and wet etching techniques. An image of the mask is shown in Figure 4.22. The stencil mask is mounted onto a vacuum chuck and aligned to the 2D material sample using the transfer stage microscope. The mask is then secured into place using a metal clip. Gold contacts are deposited using an electron beam evaporator.

4.5.2 Electrical sample measurement

To measure the electrical samples, we must wire bond the contacts to a sample carrier. There are two different sample carrier designs, as shown in Figure 4.23. The first design mounts the sample directly onto the cryostat coldfinger and wire bonds it to a print circuit board (PCB). This was our initial design, and is the simplest configuration. The second design uses a chip carrier and is more optimized for sample exchanges.

The sample carrier is then mounted to the cryostat and the wiring is connected to the cryostat electrical connectors. Since the 2D material samples are thin and very sensitive to electrostatic discharge, it is crucial to keep the electrical contacts grounded when not in use. Therefore, we built a electrical breakout box that switches from the grounded to floating states. Voltage is applied to the contacts using an external source meter (Keithley 2634B).

CHAPTER 5

High-Q Microcavity Exciton-Polaritons in TMDCs

Semiconductor microcavities with a high quality-factor are an important component for forming exciton-polaritons. Van der Waals semiconducting two-dimensional materials have been established as an interesting platform for studying polaritons, as they provide strong light-matter interactions and are versatile for nanophotonic applications. While previous studies have demonstrated polaritons in a variety of cavity structures, reliably engineering high quality cavities for two-dimensional materials while maintaining the material optical quality remains a challenge. This study demonstrates a high-Q distributed Bragg reflector microcavity that has an ultra-thin, high reflectance top mirror that is non-destructively transferred onto the two-dimensional material previously attached to the bottom mirror. Our process produces cavities with Q-factor greater than 2000, and up to 11000, establishing a reliable method of fabricating high-Q cavities for van der Waals materials. The relevant publication can be found in Ref. [1].

5.1 Introduction

Optical microcavities are a powerful a tool for exploring cavity quantum electrodynamics (QED) phenomena, controlling quantum information systems, and engineering photonic devices. They tightly confine light in at least one dimension, and thus can strongly modify the interactions between light and matter within the cavity. When the light-matter coupling in the cavity becomes stronger than the loss and decoherence of the cavity or the medium, the cavity effect is no longer perturbative, and new light-matter hybrid eigenmodes, polaritons, are formed [136, 14, 137].

A challenge in the use of microcavities is to non-destructively integrate the active media that introduces minimal defects and impurities. The challenge is especially pronounced

for reaching the strong coupling regime. With conventional materials, such as group III-V and II-IV semiconductors, polariton systems often require monolithically grown structures consisting of tall stacks of DBRs and embedded quantum well layers, all closely latticed-matched. These devices are bulky and demanding to fabricate. Polaritons have been achieved in only a handful of materials, mostly operating at low temperatures.

In recent years, 2D materials, such as TMDCs, have emerged as a new type of optical media with many unique properties including room temperature stable excitons and polaritons [138, 139, 140, 141, 142]. Contrary to conventional materials, TMDCs can be integrated with a variety of substrates and cavity configurations, albeit heterogeneous integration is required. Among them, a closed planar Fabry-Perót cavity continues to have the advantage as a robust structure with relatively simple cavity modes that are easy to model and measure. Typically, the TMDCs are transferred to the bottom half of the cavity and then enclosed by a top mirror. The top mirror can be created by direct deposition over the TMDC [138, 143], which requires high processing temperatures and chemical reactions, potentially introducing strain, impurity and defects to the TMDC and affecting its optical quality. A second method is to use an open cavity system [139, 144], where the top mirror is mounted separately and then brought close to the sample by a piezo controlled stage. Such open cavities allow tuning of the cavity length, but it involves complex experimental setup and bulky equipment. A third method is to break off a piece of a SiO_2/TiO_2 DBR from its substrate and then directly place it on the TMDC [145, 146]. Yet, since the DBR breaks off randomly, it can be very difficult to find a sufficiently large and clean piece, which also limits its integration with high-quality sample with hBN encapsulation.

In this work, we present a method to reliably create high-Q microcavities for 2D materials using a transferrable DBR. We show that the DBR, made of ZnS and magnesium fluoride MgF_2, can be readily exfoliated and transferred mechanically to reliably create high quality microcavities for 2D materials. Typical Q-factors are well above 2000 with the highest reaching 11,000. These 2D-material microcavities are resistant against degradation and allow modification of the cavity detuning by changing the effective cavity length. Strong coupling is observed by measuring the anti-crossing of the upper and lower polariton modes in angle-resolved micro-PL and reflectance spectra. These results establish a reproducible, high-Q 2D material exciton polariton system for observing many body physics phenomena and developing a polariton laser with 2D materials. The method is also applicable to other materials that require heterogeneously integrated cavities.

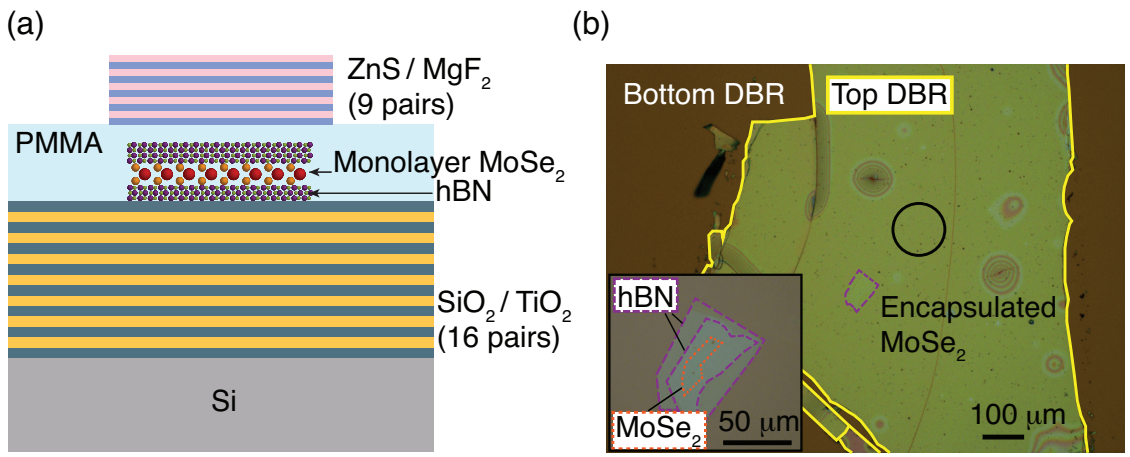

Figure 5.1: Transferrable DBR cavity structure. (a) Schematic illustration of the cavity device. (b) Optical image of the sample. The yellow solid line outlines the transferrable top DBR. The purple dashed line outlines the encapsulated $MoSe_2$ sample. The black circle indicates a clean bare cavity region for reflection characterization measurements shown in Figure 5.2. Inset: closeup image of the encapsulated $MoSe_2$ sample. The purple dashed lines outline the hBN layers. The orange dotted line outlines the monolayer $MoSe_2$.

5.2 Fabrication of 2D Material Microcavity with a Transferrable DBR

A schematic of the 2D material microcavity is shown in Figure 5.1(a). It consists of a bottom DBR, a top DBR, and an encapsulated monolayer placed at the cavity field maximum. Each of the three parts are fabricated and characterized independently, then assembled via exfoliation and dry transfer as illustrated in Figure 4.10, enabling fast and reliable sample production.

The key to making such a cavity is to have a reproducible, high reflectance top-DBR that can be dry transferred onto the 2D material sample stack. This is achieved with a ZnS/MgF_2 DBR [147, 148] fabricated via vacuum thermal evaporation (VTE) on a glass substrate. The VTE process results in a relatively weak van der Waals bonding between the DBR and the glass substrate, allowing it to be readily exfoliated. Moreover, ZnS and MgF_2 have both a high index contrast, 2.4 and 1.4 respectively, and low absorption in the visible to near-infrared range. Therefore a broadband and high reflectance mirror can be formed with only a few pairs of alternating quarter-wavelength thick layers of ZnS and MgF_2, with a total thickness of less than a micron. The thinness of the DBR also facilitates exfoliation.

The cavity fabrication procedure is described in Chapter 4 section 4.3.1. The cavity resonance can be controlled via the hBN and PMMA thickness during the fabrication as discussed further in section 5.3. Figure 5.1(b) is a top-down optical image of a complete

cavity device.

5.3 Cavity quality factor, resonance control and reproducibility

Two of the most important properties of a cavity are its quality factor and resonance energy. To characterize these properties, we perform angle-resolved reflection measurement using a supercontinuum white light source.

The quality factor depends mainly on the mirror reflectivity and absorption and scattering loss in the DBR and cavity layers. Taking the example shown in Figure 5.1(b), we first focus on the bare cavity without the 2D material stack, as marked by the black circle. Its angle-resolved reflection spectrum and an example line cut are shown in Figure 5.2(a) and 5.2(c). The line cut is fit by a Lorentzian line shape with a linewidth of 0.37 ± 0.15 meV, corresponding to a Q = 4900 ± 2000. We then measure the region with both top and bottom hBN layers but not enclosing the monolayer of $MoSe_2$. As shown in Figure 5.2(b) and 5.2(c), the introduction of hBN leads to a red-shift of the cavity resonance energy, and lowers the Q-factor due to increased inhomogeneity in the sample.

To test the reliability of our fabrication methods, we performed a systematic characterization of the Q-factors and cavity resonance energies of 26 samples created with different PMMA spin speeds, as summarized in Figure 5.3(a) and 5.3(b). We can reliably reach a Q-factor greater than 2000 for all 26 samples, ranging between 2100 – 11000, with a median of 3700, comparable to the highest reported for 2D material cavities. There is no statistically significant dependence of the Q-factor on the PMMA spin speed within our sample set.

The cavity resonance energy in our device can be controlled by the combined top and bottom hBN and PMMA thicknesses. The hBN thickness can be precisely determined in the exfoliation step. Then the desired PMMA thickness can be controlled by the PMMA spin speed. As shown Figure 5.3(b), higher PMMA spin speed leads to a thinner PMMA thickness and thereby a higher cavity resonance energy. For the 26 samples, a spin speed of 1500 rpm to 3500 rpm results in about 100 meV tuning in the resonance energy. Generally better reproducibility is obtained at higher spin speeds due to improved uniformity of the PMMA film thickness. For our devices, 2000 rpm is the optimal spin speed for maximum reproducibility, with the standard deviation of cavity resonance energy being 11.2 meV.

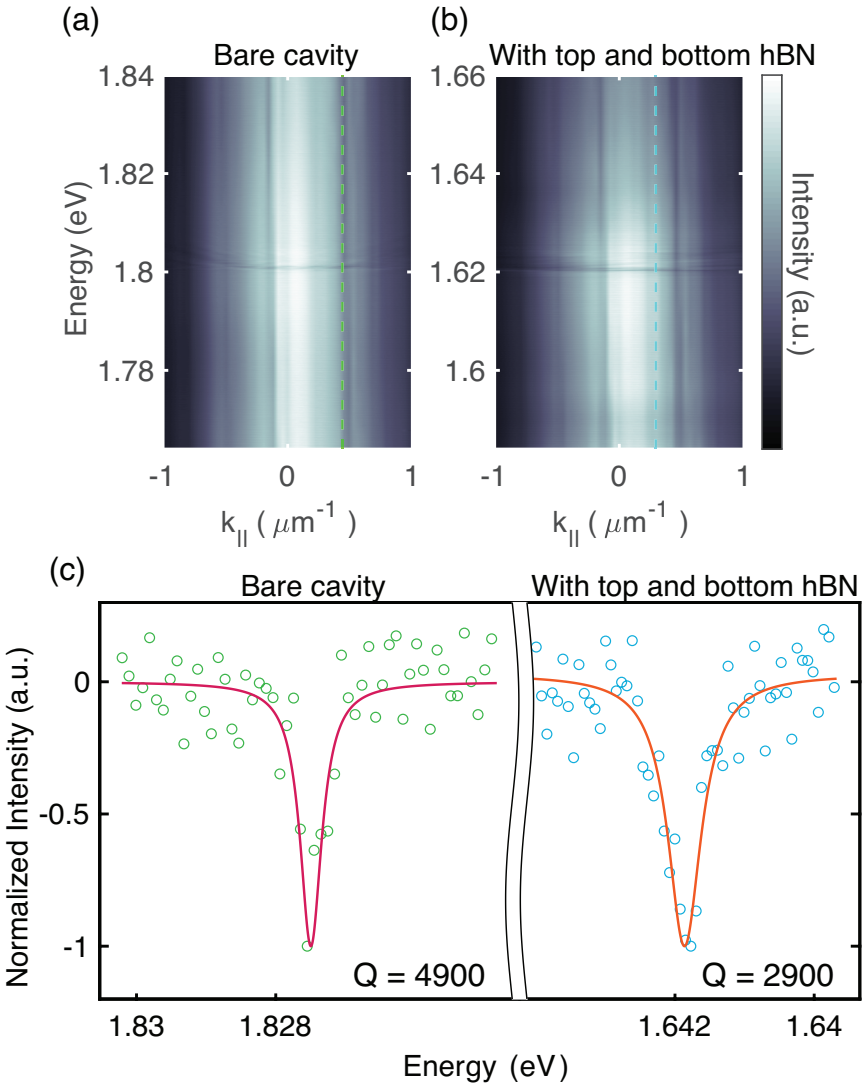

Figure 5.2: Transferrable DBR cavity characterization. (a) Angle-resolved reflection spectrum of the bare cavity region of the sample. Dashed green line marks the k value of the line-cut plot shown in Figure 5.2(c). (b) Angle-resolved reflection spectrum of the cavity with top and bottom hBN. Dashed blue line marks the k value of the line-cut plot shown in Figure 5.2(c).

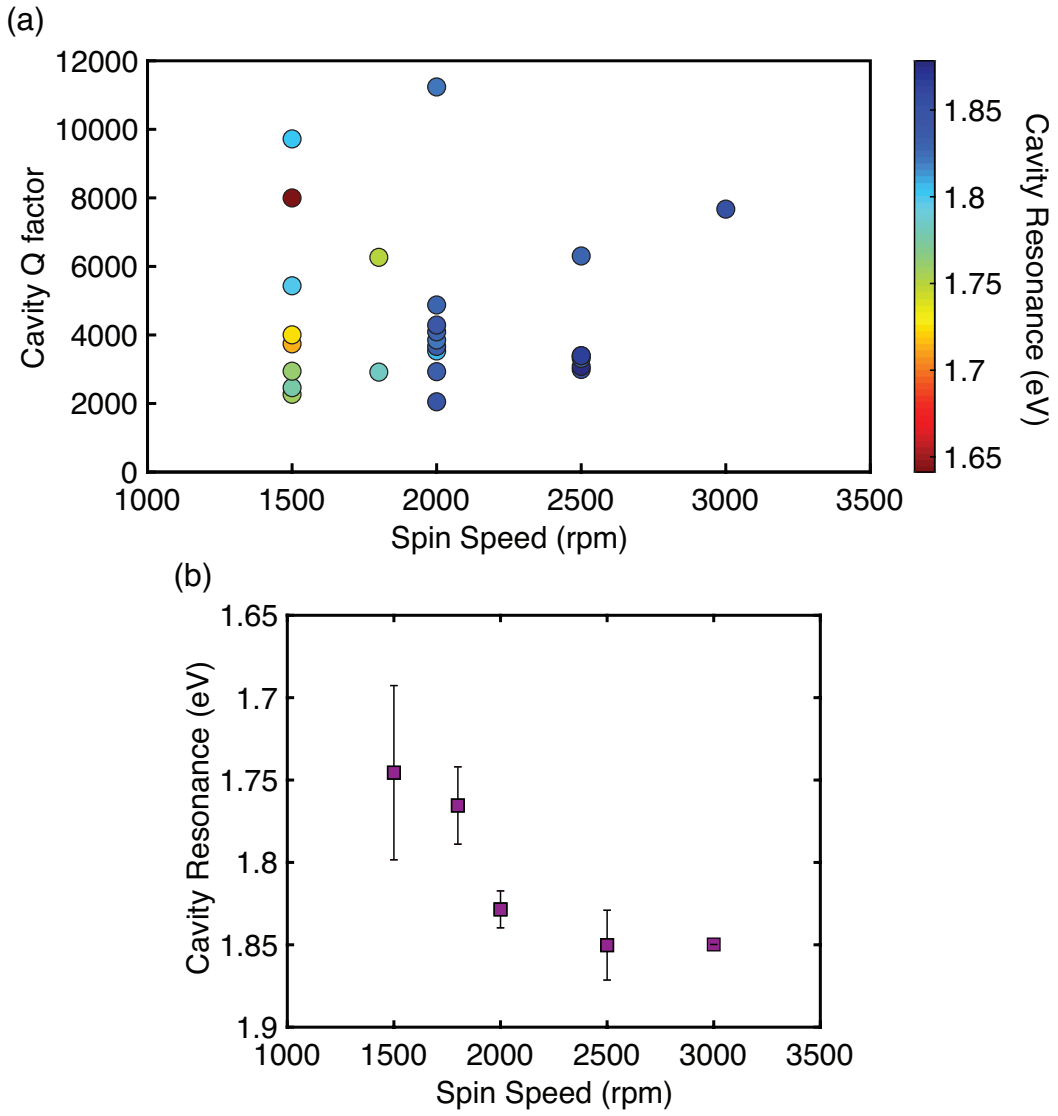

Figure 5.3: Systematic transferrable DBR cavity characterization. (a) A range of achievable cavity Q-factors and resonances with different PMMA spin speeds. The color bar indicates the cavity resonance energy. (b) Cavity resonance wavelength versus PMMA spin speed. The error bars correspond to the standard deviation of the cavity resonance energy.

5.4 Strong coupling with a transferrable DBR and monolayer $MoSe_2$

Our cavities feature high-Q, small mode-volume, and controllable, precise matching between the exciton and cavity resonances. These properties are especially important for achieving strong coupling and performing exciton-polariton studies.

In the weak coupling regime, the hBN-$MoSe_2$-hBN cavity mainly modifies the exciton emission rate. To reach the strong coupling regime, the exciton-photon energy exchange rate needs to be enhanced, by cavity confinement of near-resonant photon modes to overcome the exciton and photon decay or decoherence rates. When the strong coupling regime is established, coherent superposition of exciton and photon states leads to two new eigenstates, the lower and upper polaritons, with anti-crossing of the two separate resonances. The minimum separation, known as the vacuum Rabi splitting $E_{\text{UP}} - E_{\text{LP}} = 2\hbar\Omega$, corresponds to where the exciton and photon are in resonance. The condition of strong coupling is therefore:

$$2\hbar\Omega > \gamma_{\text{cav}} + \gamma_{\text{exc}}, \tag{5.1}$$

where γ_{cav} (γ_{exc}) is the full width half maximum linewidth of the cavity (exciton).

For our device, we measure the cavity resonance and linewidth via angle-resolved reflectance at the region of the sample with top and bottom hBN but without the monolayer, and we measure the exciton energy and PL linewidth before capping the sample stack with the top DBR. In the example shown in Figure 5.4, the cavity resonance energy at $k = 0$ is 1.646 eV and the exciton energy is 1.651 eV. The linewidths are $\gamma_{\text{cav}} = 0.6$ meV, which corresponds to Q = 2700, and $\gamma_{\text{exc}} = 6.5$ meV.

We characterize the $MoSe_2$ exciton-polaritons using both angle-resolved reflectance (Figure 5.4(a) and 5.4(b)) and micro-PL (Figure 5.4(c) and 5.4(d)) at 5K. Figure 5.4(a) shows the angle-resolved reflection and its corresponding linecut in Figure 5.4(b). The upper and lower polariton dispersions are visible by the reflection dips in the spectrum. The reflection and PL energies of the upper and lower polariton dispersions match. By fitting a Gaussian line shape to the PL data, we extracted the upper and lower polariton energies and the trion energy. To determine the vacuum Rabi splitting $2\hbar\Omega$, we fit the polariton energies with:

$$E_{\text{LP,UP}} = \frac{1}{2}\left[E_{\text{exc}} + E_{\text{cav}} \pm \sqrt{4\hbar^2\Omega^2 + (E_{\text{exc}} + E_{\text{cav}})^2}\right] \tag{5.2}$$

with Ω as a fitting parameter. We obtain $2\hbar\Omega = 34$ meV, which satisfies the strong coupling condition (Equation 5.1): 17.2 meV $> (0.6 + 6.5)$ meV.

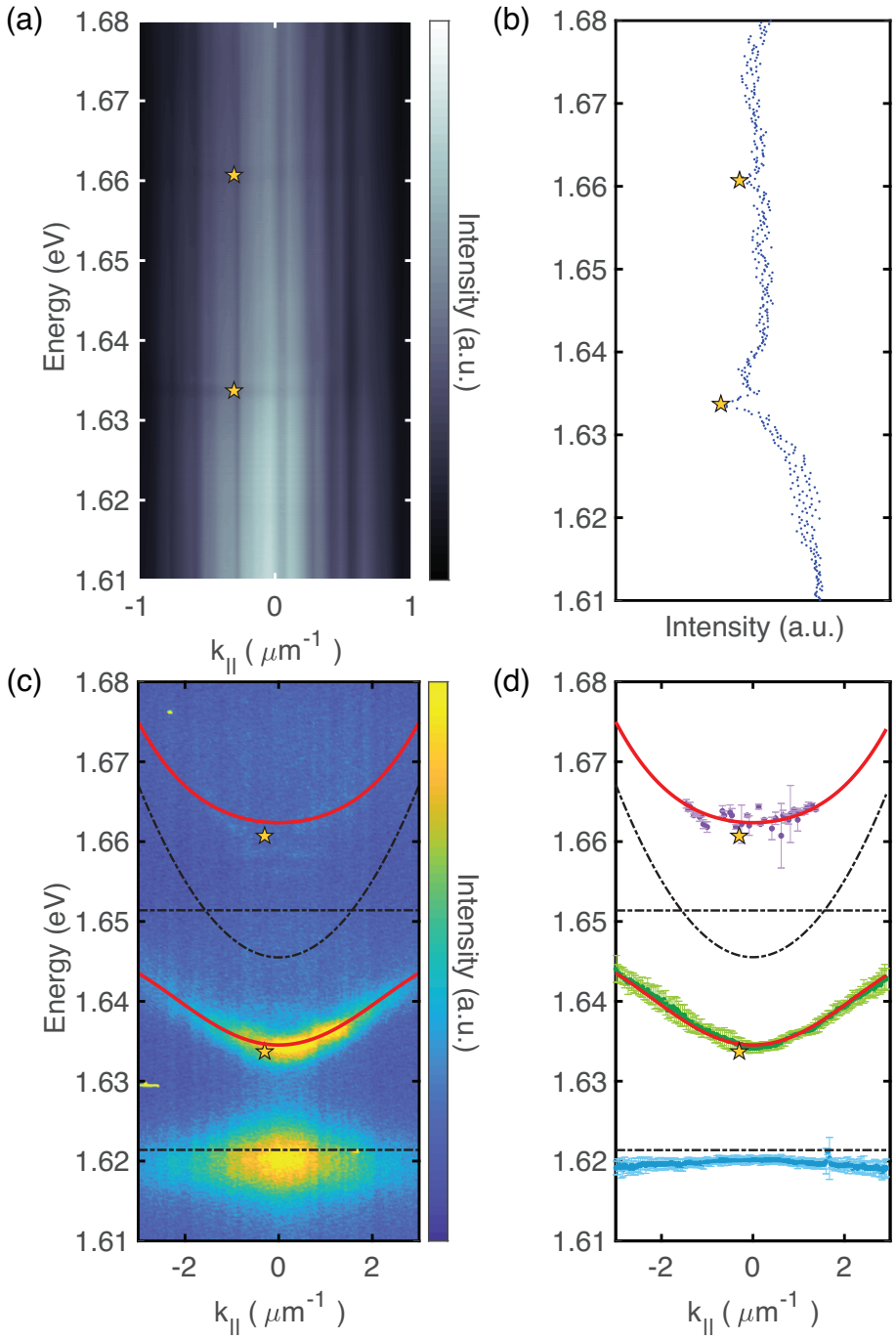

Figure 5.4: Spectral properties of the monolayer $MoSe_2$ polariton device. (a) Angle-resolved reflection spectrum. The orange star indicates the location of the dip in the reflection spectrum at a given value of k. (b) Line-cut of Figure 5.4(a) at $k = 0.3$. (c) Angle-resolved micro-PL spectra. The black dot-dashed lines show the bare cavity dispersion, $MoSe_2$ exciton emission and trion emission energies. The red solid lines show fitted upper and lower polariton modes. (d) Polariton energy versus in-plane wavenumber $k_{||}$. The error bars on the energy data are 95% confidence intervals of the Gaussian fit. The error bars for the lower polariton and trion energies have been multiplied by a factor of 6 for increased visibility.

5.5 Conclusion

In summary, we have developed a flexible and reliable method to create high-Q DBR microcavities for van der Waals materials and have demonstrated strong coupling in the cavity with an hBN-encapsulated monolayer of $MoSe_2$. The high-reflectance top DBR, fabricated via VTE on glass with high index contrast materials, can be readily exfoliated from the glass substrate and transferred. The cavity resonance can be controlled by hBN thickness and PMMA spin speeds. The cavity structure is one of the highest-Q DBR cavity made for monolayer 2D materials, which will facilitate future studies of nonlinear and many-body polariton phenomena.

CHAPTER 6

Photon Lasing in TMDC Heterobilayers

Two-dimensional semiconductors have emerged as a new class of materials for nanophotonics owing to their strong exciton–photon interaction [6, 26] and their ability to be engineered and integrated into devices [149]. Taking advantage of these properties, we engineer an efficient lasing medium based on direct-bandgap interlayer excitons in rotationally aligned atomically thin heterostructures [150]. Lasing is measured from a transition-metal dichalcogenide heterobilayer (WSe_2–$MoSe_2$) integrated in a silicon nitride grating resonator. An abrupt increase in the spatial coherence of the emission was observed across the lasing threshold. The work establishes interlayer excitons in two-dimensional heterostructures as a gain medium with spatially coherent lasing emission and potential for heterogeneous integration. With electrically tunable exciton–photon interaction strengths [151] and long-range dipolar interactions, these interlayer excitons promise applications as low-power, ultrafast lasers and modulators and a way to study many-body quantum phenomena [18]. The relevant publication can be found in Ref. [2].

6.1 Introduction

Semiconductor lasers are ubiquitous in today's technology because they are compact, cover a wide range of wavelengths, and allow efficient electrical pumping and fast electrical modulation. They are predominantly based on traditional III-V quantum wells. To achieve lower power consumption, more compact size, and a higher degree of integration with silicon, there has been tremendous effort to develop alternative gain materials and structures, such as nanowire lasers [152], spasers [153], and photonic crystal lasers [154]. However, tunability, electrical pumping and heterogeneous integration remain as common challenges.

Recently, monolayer TMDCs have emerged as a new class of material for semiconductor lasers, as they are atomically thin and feature strong exciton emission [26, 6]. Whereas lattice mismatch limits the choice of substrates for 3D semiconductors, 2D TMDCs do

not have dangling bonds, and can be directly integrated with different substrates [149]. Previous studies have used two criteria to assess lasing in monolayer TMDCs: nonlinear intensity dependence, and linewidth reduction as a function of pump power [155, 156, 157, 158, 159, 160]. However, the photon flux appears to be below the stimulated emission threshold [161]. Spatial coherence – an important property for characterizing lasers – has not been studied. Hence it is difficult to exclude localized excitons, such as point defects, as the source of the observed nonlinear power dependence. Moreover, with only a monolayer as the gain medium, tunability is limited and vertical p–n junctions are not possible without contacting with other doped semiconductors.

In contrast, heterostructures open the door to the engineering of band structures and exciton states. Spatially indirect excitons in heterostructures have been intensively studied [162, 151], for they feature an electrically tunable static dipole with long-range dipole interactions, promising rich many-body quantum phenomena [18]. However, the reduced oscillator strength of spatially indirect excitons typically renders them dark and hard to access.

Here we show that in rotationally aligned 2D WSe_2-$MoSe_2$ heterobilayers integrated on a SiN cavity (Figure 6.1), interlayer excitons form an efficient gain medium, supporting lasing with extended spatial coherence at a low population inversion density. As illustrated in Figure 6.1(b), by forming a direct bandgap between the two monolayers [150] that are less than one nanometre apart, the interlayer excitons retain a sufficiently large oscillator strength. With type-II band alignment, the heterobilayer forms a three-level system that allows efficient pumping through the intralayer exciton resonances followed by rapid electron transfer to a lower-energy empty conduction band [163, 150] (Figure 6.1(c)). As a result, population inversion is readily achieved at the reduced bandgap while avoiding fast intralayer radiative loss of the carriers. Moreover, unlike some of the cavities used for monolayer exciton lasers, the cavity mode in our device fully covers the heterobilayer, allowing gain over the full area of the bilayer, and supporting extended spatial coherence (Figure 6.1(a)). We observe lasing accompanied by an abrupt increase in the spatial coherence length as the photon occupancy exceeds unity. The emission intensity increases nonlinearly more than 100-fold across the threshold, and then continues to increase linearly with pump power (without saturation) up to the highest power used. Our results establish interlayer excitons in engineered TMDC heterobilayers as an efficient lasing medium, which, compared to excitons in monolayer TMDCs, feature electrically tunable long-range dipole interaction and oscillator strength [151], robust valley polarization [84], and a type-II band alignment well-suited for electrical injection via an atomically thin bilayer p–n junction [20, 21].

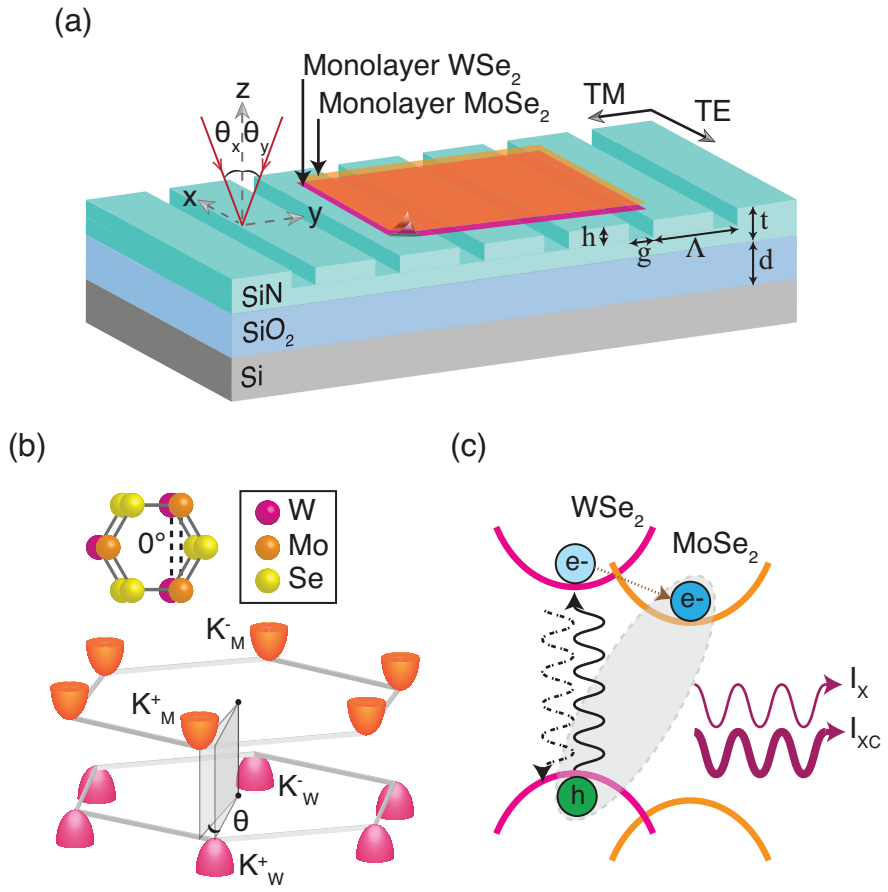

Figure 6.1: Illustration of the heterobilayer/grating cavity laser system. (a) Schematic of the laser device consisting of a heterobilayer on a grating cavity. The along-bar (cross-bar) direction and polarization are defined as x (y) and TE (TM) respectively. Grating cavity design parameters are the following: total SiN thickness (t), SiO_2 thickness (d), grating thickness (h), grating period (Λ), gap width (g). We define θ_x (θ_y) as the azimuthal angle of the light beam along the x-z (y-z) plane with respect to the z-axis, as indicated by the red arrows. (b) Illustration of the rotationally aligned heterobilayer with twist angle $\theta = 0°$ (top), and the correspondingly a direct bandgap at the K-valleys (bottom). (c) Band alignment and carrier dynamics of the heterobilayer. The heterobilayer has a type-II band alignment, forming a three-level system for the injected carriers. Intralayer excitons are excited by a pump laser in the WSe_2 layer (solid wavy line). Some electrons transfer to the lower $MoSe_2$ conduction band on a fast (10 - 100 fs) time-scale (dotted line), while others recombine as intralayer excitons with lifetimes of 1-10 ps (dash-dotted wavy line). Without the cavity, the inter-layer excitons (dashed line) recombine with a lifetime on the order of 1 ns (I_X), and, with cavity enhancement, on the order of 100 ps (I_{XC}).

6.2 Methods: sample fabrication and optical measurements

6.2.1 Sample fabrication

To fabricate the grating cavity, we first grew a SiN film with a SiO_2 buffer on an Si substrate using low-pressure chemical vapour deposition, then patterned it using electron beam lithography and created the grating bars by plasma dry etching (Chapter 4 section 4.3.2). The grating parameters indicated in Fig. 1a are as follows: $d = 1,475$ nm, $t = 113$ nm, $h = 100$ nm, $\Lambda = 615$ nm and $g = 50$ nm. The individual WSe_2 and $MoSe_2$ monolayers were mechanically exfoliated onto a SiO_2 substrate using PDMS polymer (Chapter 4 section 4.1.1). The exfoliated monolayers were stacked into a heterostructure using a high-accuracy rotational alignment method (Chapter 4 section 4.2.2). First, the $MoSe_2$ was picked up with a PDMS/PPC stamp under an optical microscope. Second, the crystal axes of $MoSe_2$ and WSe_2were rotationally aligned to be 0° or 60° before stacking. Third, the stacked heterostructure was dropped down onto the PPC. Last, the polymer residue was dissolved, and the sample was annealed at 350 °C for a total of 7 hours.

6.2.2 Heterobilayer twist angle

We can verify the twist angle of the heterobilayer aligned under the optical microscope by angle-dependent SHG measurements (Chapter 4 section 4.2.1). Figure 6.2 shows an optical microscope image of two different samples and the corresponding angle-dependent SHG measurements. By fitting the SHG pattern with a $\cos^2(3\theta)$ function, where θ is the angle between the armchair direction of the monolayer and the polarization direction of the beam, we can obtain the twist angle. We did not measure the SHG for the heterobilayer before putting it on the grating, but from experience, we have found that the straight edges of exfoliated monolayers reliably correspond to the armchair axis of the crystal (Chapter 4 section 4.2.2). Therefore, we aligned the two straight flake edges under the optical microscope.

6.2.3 Time-resolved PL

To measure the decay time of the TM emission we used a Hamamatsu streak camera system. The emission was polarization-selected for the TM direction and sent to the streak camera. As shown in Figure 6.3, a line-cut of the streak camera spectrum was fitted with a bi-exponential function to determine the lifetime. The fitted lifetime is around 2 ns.

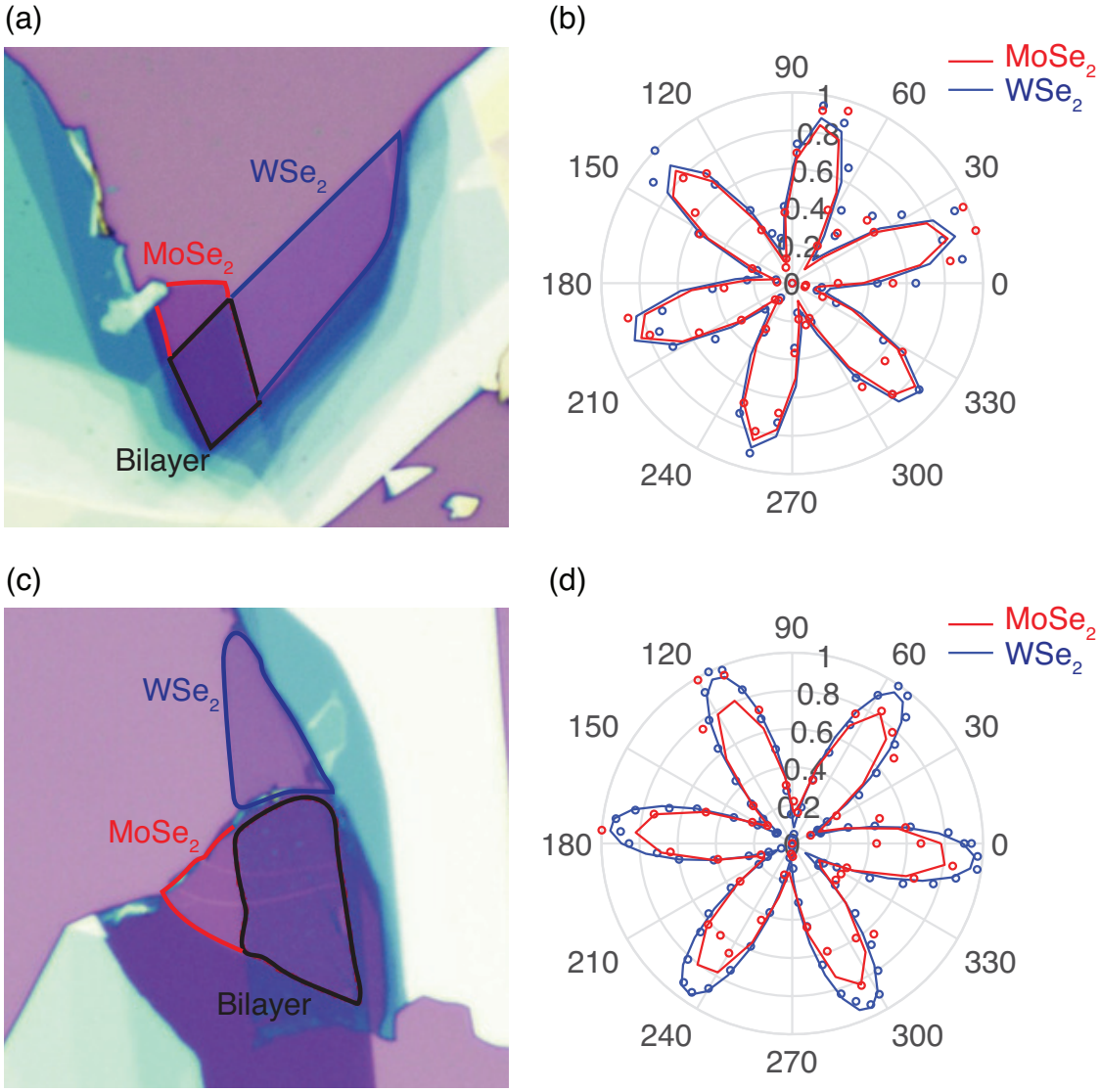

Figure 6.2: Heterobilayer twist angle. (a) Optical image and (b; open circles) angle-resolved SHG measurements of WSe_2-$MoSe_2$ heterobilayers. (c-d) As (a-b) but for a different sample. The field of view of the optical images is around 60 μm. Solid lines in (b), (d) are fits by a $\cos^2(3\theta)$ function, which give relative twist angles of $0.22° \pm 1.78°$ for (b), and $0.34° \pm 1.5°$ for (d).

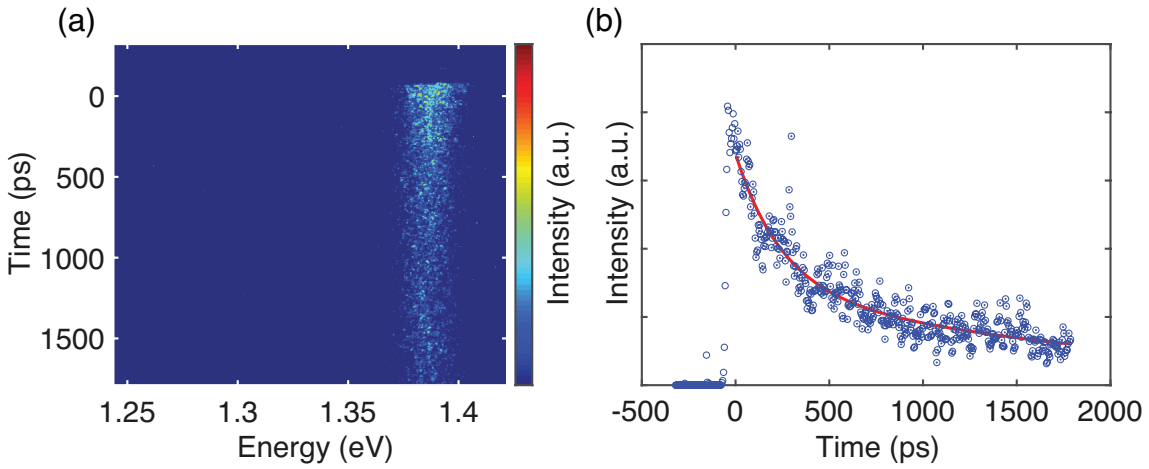

Figure 6.3: Interlayer exciton lifetime. (a) Time-resolved PL spectrum for TM emission. (b) Line-cut of a near 1.38 eV. Red line is a bi-exponential fit to the data, with a fitted lifetime of 2 ns.

6.2.4 PL mapping of the heterobilayer device

The spatially resolved PL mapping of the heterobilayer device is shown in Figure 6.4. For this measurement, we use a 633-nm cw laser and selected TE polarization for excitation. The sample is mounted on an Attocube ANC 300 piezo stage and scanned as needed. Spectral band-pass filters are used to select the emission from bilayer, WSe_2 and $MoSe_2$ regions.

6.2.5 Optical measurements of lasing characteristics

Chapter 4 section 4.4 describes the optical setup used for the angle-resolved PL reflection (section 4.4.1) and the coherence measurements (section 4.4.3) of the heterobilayer laser device. The sample was cooled to 5 K using a Montana Instruments Fusion 2 cryostat. Fourier-space imaging was used to measure angle-resolved reflection and micro-PL of the device. For reflection, a tungsten halogen lamp was used. For micro-PL, a pulsed Ti:sapphire laser (80 MHz repetition rate, 150 fs pulse width) near-resonant with the WSe_2 A-exciton (1.7 eV) was used to excite the sample. The emission was collected using a 0.42 NA objective lens, passed through a long-pass filter to filter out the excitation laser and a linear polarizer to selectively measure TE and TM modes, and sent to a Princeton Instruments spectrometer with a measured spectral resolution of 0.3 nm. The entrance slit of the spectrometer is aligned along the y direction. The slit width of 100 μm corresponds to a range $|k_y| < 0.13\ \mu\text{m}^{-1}$. The NA of the collection optics corresponds to a range of $|k_x| < 2\ \mu\text{m}^{-1}$. Spatial coherence measurement was performed using a retro-reflector

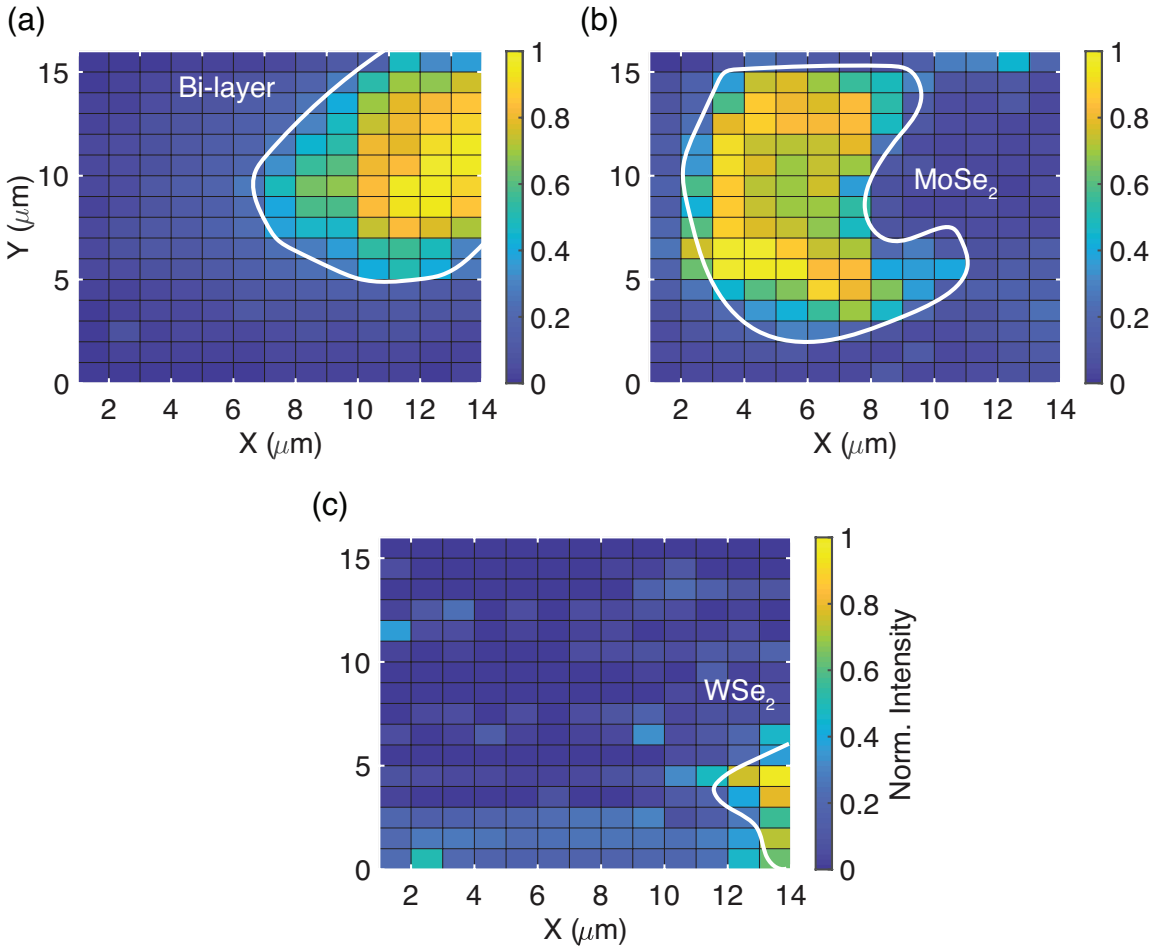

Figure 6.4: PL spatial mapping of lasing device. The normalized intensity of PL from the device is shown as a function of position. Spectral filters centered around their respective exciton peak energies were applied for each image. The white contours mark the regions of (a) heterobilayer, (b) $MoSe_2$, and (c) WSe_2.

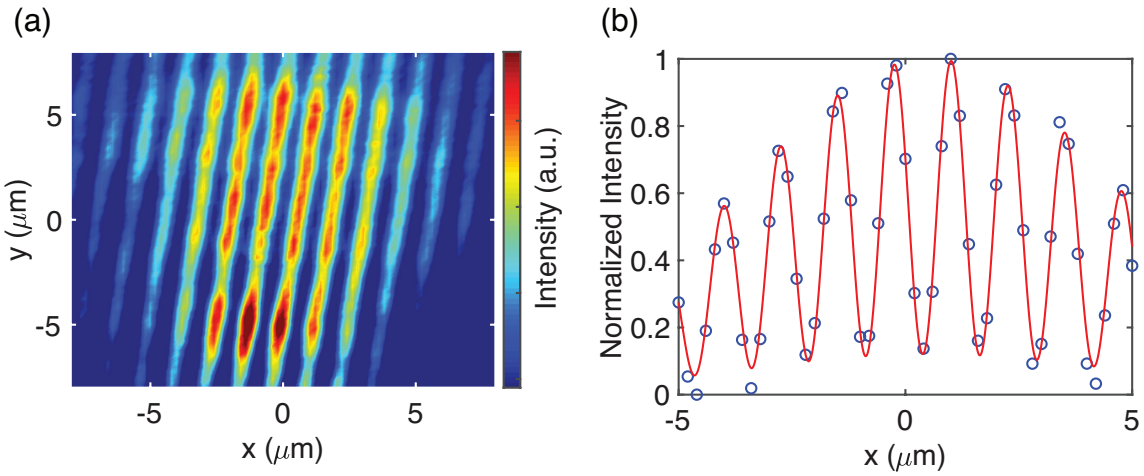

Figure 6.5: Temporal coherence of the lasing device. Shown are temporal coherence interference fringes at $g^{(1)}(\tau = 0)$ measured using a two-retro-reflector Michelson interferometer under cw excitation above threshold. (a) Interferogram image at τ = 0. (b) Horizontal line-cut of a around y = 1.5 μm. The red line is a fit to the Gaussian pump beam profile modulated by a cosine function. Here $g^{(1)}(\tau = 0) = 0.78$.

Michelson interferometer setup as shown in Figure 4.20. Emission rid of scattered pump laser light was sent to a 50:50 beam splitter which divided the light into two paths, the mirror path and the retroreflector path. In order to change the time difference (τ) between the two paths, the retroreflector is mounted on a stepper motor which can have a step size as small as 50 nm (about 0.167 fs). The interference pattern was collected by a Princeton Instruments eXcelon CCD.

The emission from our ultra-compact device is necessarily weak and the detector efficiency at 1.35 eV is poor, hence it is difficult to simultaneously achieve good time and spatial overlap of the interference signal with the asymmetric interferometer. With a symmetric interferometer built with two retro-reflectors, the alignment is much less sensitive to slight changes in the incident beam; therefore we are able to achieve good alignment of the signal path by using an axillary alignment laser and obtain visibility for $g^{(1)}(\tau = 0)$ close to 0.8 (Figure 6.5).

6.2.6 Photon number

Photon occupancy per pulse ($I_p(k \approx 0)$) was estimated from the total count rate on the detector, n_c. The total integration time for angle-resolved spectra was 90 s. The two values are related by: $I_p = \eta\rho f n_c(k \approx 0)$. Here $\eta \approx 10^{-7}$ is the total detection efficiency of the setup, which is independently calibrated by replacing the sample with a laser-coupled single-mode fiber, $\rho \approx 1$ is the number of k-space modes within the integrated region, and

$f = 80$ MHz is the repetition rate of the pump laser.

6.2.7 Transparency condition

The transparency condition is defined as the number of carriers required for the energy difference between the quasi-Fermi levels in the conduction ($E_{F,c}$) and valence ($E_{F,v}$) bands to equal the lasing energy ($E_{F,c} + E_{F,v} = 0$). The quasi-Fermi levels are determined by the electron density:

$$N_e = N_c \int_0^\infty \frac{1}{1 + \exp(\epsilon_c - \epsilon_{F,c})} d\epsilon_c. \tag{6.1}$$

Here, $\epsilon_c = E_c/k_BT$ and $\epsilon_{F,c} = E_{F,c}/k_BT$, E_c is the conduction band edge, k_B is the Boltzmann constant and T is temperature. N_c is the effective density of states in two dimensions for electrons with an effective mass m_e^*:

$$N_c = \frac{m_e^* k_B T}{\hbar^2 \pi}. \tag{6.2}$$

Solving equation 6.1 for $\epsilon_{F,c}$ we obtain:

$$\epsilon_{F,c} = \ln\left[\exp\left(\frac{N_e}{N_c}\right) - 1\right]. \tag{6.3}$$

The equation for valence band Fermi energy and hole carrier density can be written in a similar way. Assuming $n = N_e = N_h$ and using the effective masses of K valley electron and holes given in Ref. [164], we solve for the carrier density that satisfies the transparency condition and obtain $n_{tr} = 8 \times 10^{10}$ cm^{-2}, which is in good agreement with the threshold carrier density $n_{th} = 5.7 \times 10^{10}$ cm^{-2}.

6.2.8 Simplified rate equation model of the laser

We use the following rate equations to describe the time evolution of interlayer exciton density N and the photon density S in the lasing mode:

$$\frac{dN}{dt} = \frac{\eta P}{\hbar \omega V_a} - \frac{(1-\beta_0)N}{\tau_{sp}} - a\nu_g(N - N_{tr})S \tag{6.4}$$

$$\frac{dS}{dt} = \Gamma \frac{F\beta_0 N}{\tau_{sp}} - \Gamma a \nu_g (N - N_{tr})S - \frac{S}{\tau_p} \tag{6.5}$$

Parameters in the equation are listed in Table 6.1. In the heterobilayer system, electron and hole transfer takes place on the subpicosecond timescale, much shorter than the interlayer

Parameter	Definition	Value
F	Purcell factor	2.25
Γ	Confinement factor	0.0208
V_a	Carrier injection volume	$1.4 \times 10^{-3} \mu\text{m}^{-3}$
τ_{sp}	Spontaneous emission lifetime	2 ns
τ_p	Photon lifetime	0.3 ps
η	Absorption efficiency	20 %
N_{tr}	Transparency density	8×10^{-10} cm^{-2}
β_0	Spontaneous emission factor	0.046
a	Absorption cross section	1.9×10^{-14} cm^{-2}
ν_g	Group velocity	1.5×10^{8} m/s

Table 6.1: Rate equation model parameters.

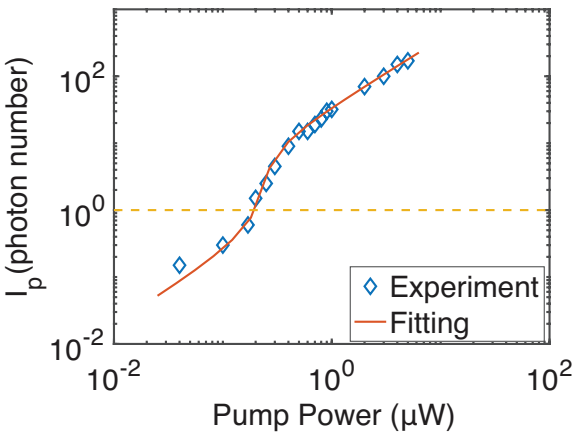

Figure 6.6: Rate equation fitting of power-dependent emission. The log–log plot of photon occupancy versus pump power . The diamonds represent measured data shown in Figure 6.10(b), and the solid line is a rate-equation fitting. Details of the rate equation simulation is described in section 6.2.8.

exciton lifetime. Therefore, we consider a pulsed pump P that creates an initial carrier population of $N(t = 0) \propto P$. The photon number I_p is proportional to the photon density, and $I_p = 1$ at threshold. The simulated curve of I_p versus pump power matched the experiment well, as shown in Figure 6.6.

6.3 Results: spectral and coherence properties of the WSe_2 - $MoSe_2$ heterobilayer laser

6.3.1 Device characterization

The lasing device comprises a rotationally aligned WSe_2–$MoSe_2$ heterobilayer placed on a SiN grating resonator, as illustrated in Figure 6.1(a). To form bright interlayer excitons, we accurately align the crystal axes of the WSe_2 and $MoSe_2$ monolayers to within 1° of relative rotation, as verified by SHG measurements (Figure 6.2). Consequently, the band extrema at the K valleys of the two monolayers align in momentum space to form a direct bandgap (Figure 6.1(b)). With type-II band alignment, carriers can be injected into the heterobilayers efficiently via the intralayer exciton resonance, followed by rapid electron transfer to the empty conduction band of $MoSe_2$ on a timescale of [163, 84] 10 - 100 fs (Figure 6.1(c)). As a result, band inversion can be established at the smaller, interlayer bandgap. Once separated into the two monolayers, radiative recombination is reduced, rendering long interlayer exciton lifetimes of the order of 1 ns (Figure 6.3). PL measurements of the heterobilayer show that interlayer exciton emission is much stronger than intralayer emission (Figure 6.7(b)), confirming efficient charge transfer and sufficient build-up of the interlayer-exciton population. Spatially resolved PL shows uniform emission from the interlayer (intralayer) excitons in the bilayer (monolayer) regions (Figure 6.4).

The grating cavity provides optical feedback when photons are coupled to its resonances. The cavity modes are sensitive to the propagation and the polarization directions of the electric field. We define the propagation (polarization) direction along the grating bar as x (TE) and across the bar as y (TM), as illustrated in Figure 6.1(a). We tune the grating period Λ, thickness h and fill factor g to obtain a high Q-factor for the TE mode and match it to the exciton resonance at zero in-plane wavenumber, $k = 0$. The heterobilayer lies directly on the grating where the evanescent field remains strong [142]. The TM cavity modes are far blue-detuned from the excitons; therefore, the TM exciton modes are not affected by the cavity (Figure 6.8).

We confirm the TE-cavity modes by measuring the empty-cavity dispersion with angle-resolved reflectance spectroscopy; the results agree well with the simulation by rigorous

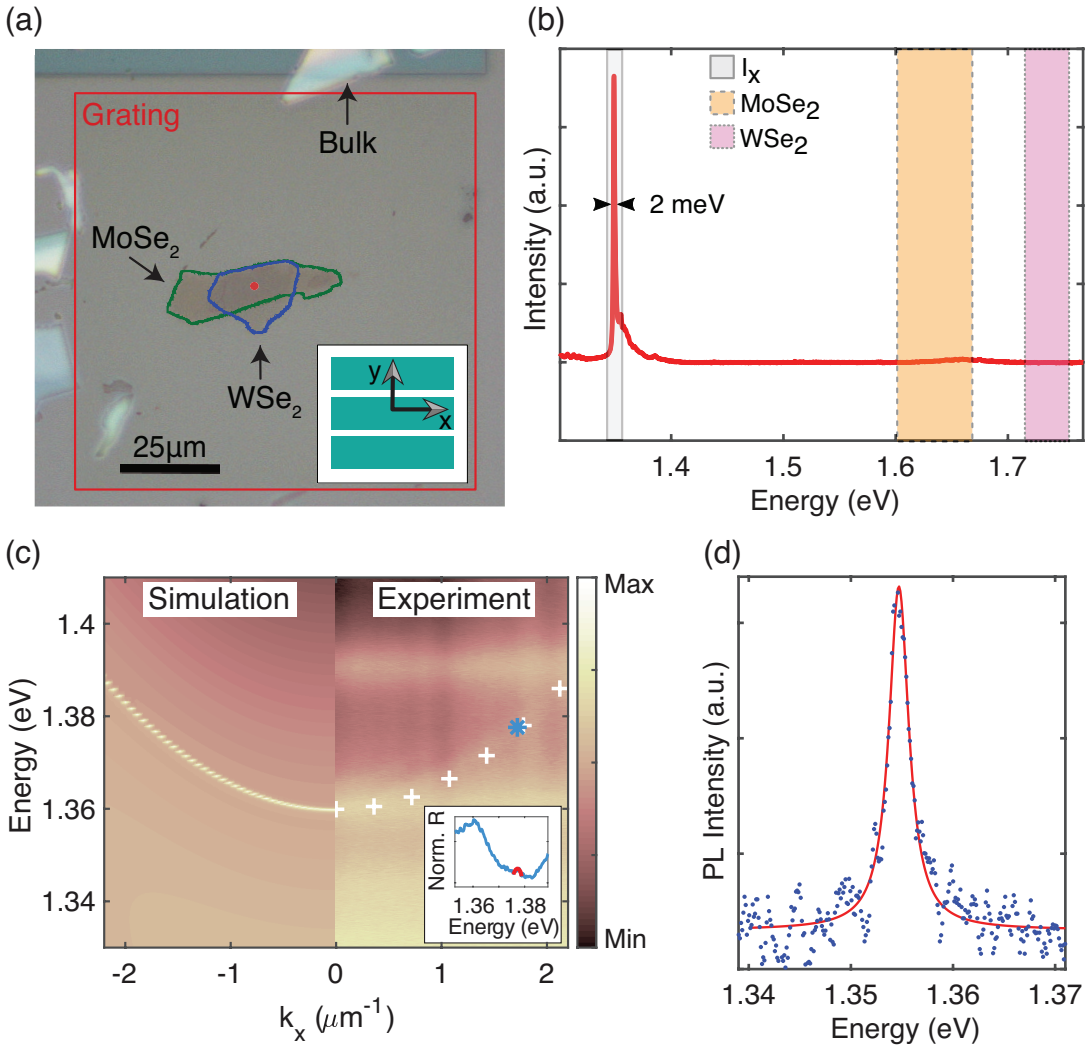

Figure 6.7: Properties of the heterobilayer and grating cavity. (a) An optical microscope image of the $WSe_2/MoSe_2$ heterobilayer integrated on a grating cavity. The red square outlines the grating region, and the red circle indicates the laser spot size. Inset: direction of the grating bars. (b) PL spectrum from the heterobilayer. The sample was pumped with a 633-nm laser at power of 20 μW. The shaded boxes highlight the spectral range of interlayer (I_X), $MoSe_2$ and WSe_2 exciton emission. (c) TE-polarized along-bar, angle-resolved, simulated (left and overlaid crosses in the right) and measured (right) reflectance spectra. Inset: line-cut of the normalized reflectance spectrum around $k_x \approx 1.7$ μm^{-1} (blue trace); The red line is a fit to the cavity mode. The star symbol marks the peak of the fitted cavity mode. (d) PL spectrum (blue dots) near $k_x \approx 0$. The pump was on resonance with WSe_2 at a pump power of 0.1 μW. Red line is a Lorentzian fit, with a fitted linewidth of 2.4 meV.

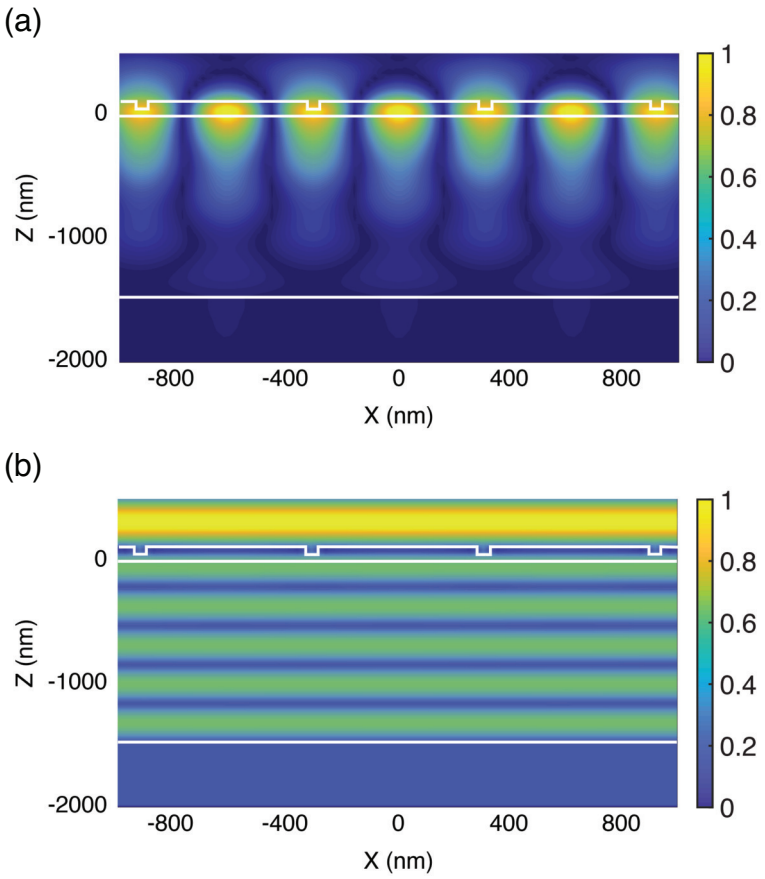

Figure 6.8: Electric field profiles of the grating cavity. Shown are simulated normalized electric field profiles as a function of position near the center of a grating cavity with lateral dimensions of 100 μm × 100 μm. (a) TE-polarized light at the cavity resonance at $k = 0$, showing strong field enhancement in the grating layer including at its surface where the heterobilayer is placed. (b) TM-polarized light at the same wavelength as (a) showing negligible cavity effects. White lines outline different layers of the grating cavity. The corresponding Purcell factor is calculated to be around 2.4.

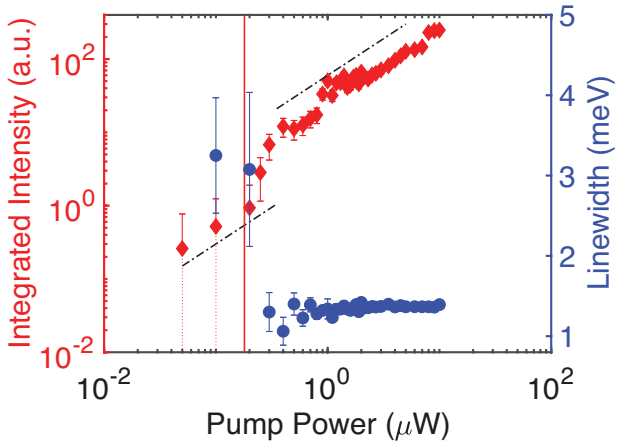

Figure 6.9: Power-dependence measurement reproducibility. The photon occupancy (red) and linewidth (blue) of TE emission from the heterobilayer versus input pump power, similar to that shown in Figure 6.10(b) but measured on a different day to show the reproducibility of the device. The error bars on the photon occupancy data include the shot noise and detector read noise. The error bars on the linewidth data correspond to the 95% confidence interval of the Lorentzian fit.

coupled wave analysis (RCWA), as shown in Figure 6.7(c). The TE mode Q-factor from the simulation is around 2,000. However, the actual cavity Q-factor is presumably lower, owing to fabrication imperfections. From the reflectance spectra of the empty cavity, we estimate a Q-factor of between 500 and 680 (Figure 6.7(c) inset), but the exact value is difficult to determine owing to low contrast and white-light noise. The PL spectral linewidth from the device corresponds to a Q-factor of around 630 (Figure 6.7(d)).

6.3.2 Spectral properties

The heterobilayer allows efficient optical pumping through the intralayer exciton resonances, which are far above the resonances of the interlayer excitons or the cavity. With the pump laser at 1.7 eV, the PL from the cavity mode at $k \approx 0$ and energy $E \approx 1.35$ eV brightens rapidly as the pump power increases, as seen in the along-bar angle-resolved PL (Figure 6.10(a)).

Integrating over $k_x = \pm 0.7$ μm^{-1} and $E = 1.352$ to 1.359 eV, we obtain the photon occupancy $I_p(k \approx 0)$ after accounting for the independently measured collection efficiency of the optical path (section 6.2.6). As $I_p(k \approx 0)$ approaches one, $I_p(k \approx 0)$ shows clearly a superlinear increase with pump power, consistent with the onset of stimulated emission into the cavity mode (Figure 6.10(b)). The power-dependent PL measurement is reproducible, as shown by a measurement performed on a different day (Figure 6.9).

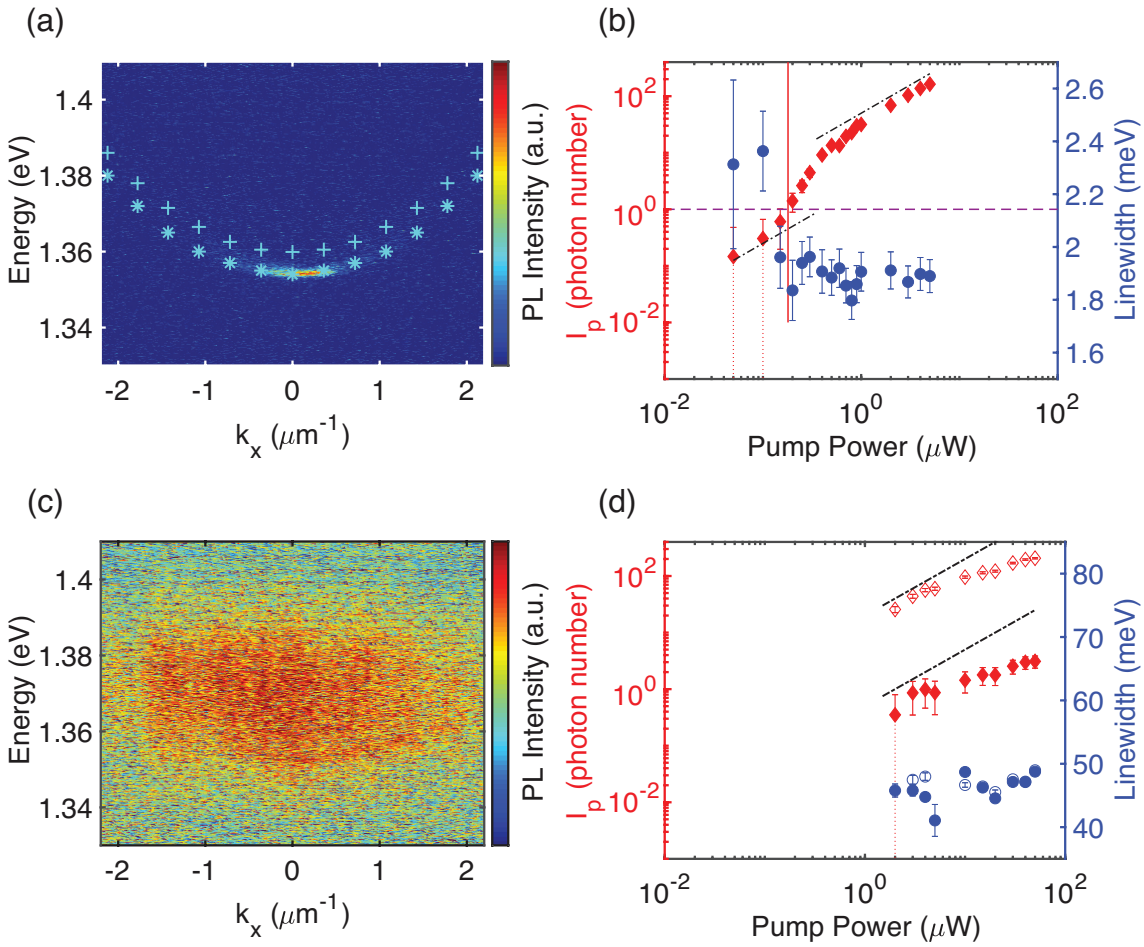

Figure 6.10: Spectral properties of the interlayer exciton laser. (a) Angle-resolved micro-PL spectra for the along-bar TE direction at $P = 0.6\mu$W with overlaid simulated empty cavity (crosses) and cavity with bilayer (stars) dispersions. (b) The photon occupancy (red) and linewidth (blue) of the TE emission versus input pump power. The emission intensity is integrated over $|k_x| < 0.7\ \mu\text{m}^{-1}$, $|k_y| < 0.13\ \mu\text{m}^{-1}$, and $E = 1.352 - 1.359$ eV. The dot-dashed line indicates linear dependence, the vertical red line marks P_{th}, and the horizontal purple line indicates $I_p = 1$. (c) Angle-resolved micro-PL spectra for the along-bar TM direction at $P = 10\ \mu$W. (d) The pump power dependence of the TM emission photon occupancy (red) and linewidth (blue), integrated over $|k_x| < 2\ \mu\text{m}^{-1}$, $E = 1.340 - 1.400$ eV (open symbols) and $|k_x| < 0.7\ \mu\text{m}^{-1}$, $E = 1.352 - 1.359$ eV (filled symbols). Integration over $|k_y|$ is 0.13 μm^{-1}. The error bars on the photon occupancy data include the shot noise and detector read noise. The error bars on the linewidth data correspond to the 95% confidence interval of the Lorentzian fit.

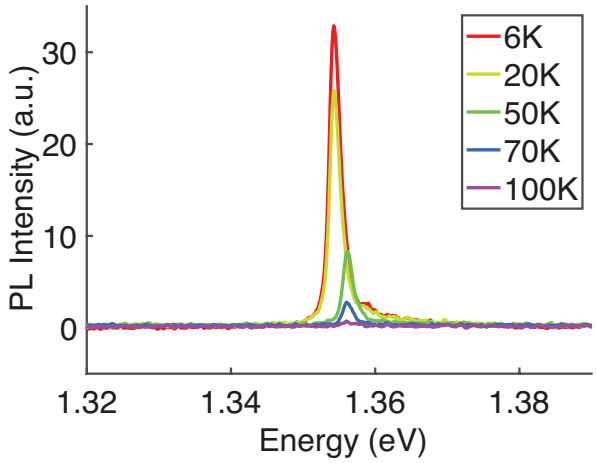

Figure 6.11: Temperature-dependent real space PL spectra of the lasing device.

The pump power at the threshold of $I_p(k \approx 0) = 1$ is $P_{th} = 0.18$ μW. Considering the typical absorption efficiency (20%) of monolayer WSe_2, we obtain the threshold carrier density $n_{th} = 5.7 \times 10^{10}$ cm^{-2}, in good agreement with the density required for the transparency condition $n_{tr} \approx 8 \times 10^{10}$ cm^{-2} (section 6.2.7). Far above threshold, the output intensity becomes linear with pump power and does not saturate up to $P = 28P_{th}$, the highest power used for TE measurements. The nonlinear increase of the intensity is reproduced by a simplified rate equation model, as described in section 6.2.8 (Figure 6.6).

Accompanying the superlinear increase in the emission intensity at threshold, the linewidth of the emission drops sharply, as shown in Figure 6.10(b), signifying the increase of temporal coherence. The linewidth at excitation powers below ~ 0.05 μW may be broader, but our detectors are not sufficiently sensitive to detect the emission. The saturation and slight increase of linewidth with increasing power above threshold may be due to interactions among the carriers and spatial mode competition [165]. The sharp lasing emission decreases in intensity as we increase temperature, but persists up to 70 K, suggesting that lasing may survive at 70 K or higher (Figure 6.11).

In stark contrast with the TE emission, TM-polarized emission is not coupled to the cavity mode and does not show threshold behavior. The emission becomes detectable only at high pump powers. An example is shown in Figure 6.10(c) for $P = 10\mu$W. The emission spreads uniformly in k over the numerical aperture of our collection optics and over a broad energy range of about 70 meV. With increasing pump power, the total integrated emission intensity increases sublinearly with pump power (Figure 6.10(d)) and is a few times weaker than that of the TE intensity. When integrated over the same small ranges of k and E near the lasing mode, the TE and TM output intensities differ by several orders of magnitude (filled diamonds in Figure 6.10(b) and 6.10(d)). In other words, while the TM emission is

suppressed and remains broadly distributed in k and E, the TE emission is concentrated in ranges of energy and k that are one to two orders of magnitude smaller, as a result of stimulated emission.

6.3.3 Coherence properties

To confirm the extended coherence expected of a laser with a 2D gain medium, we study the first-order spatial coherence function $g^{(1)}(\boldsymbol{r}_1, \boldsymbol{r}_2)$ defined as follows:

$$g^{(1)}(\mathbf{r}_1, \mathbf{r}_2) = \frac{G^{(1)}(\mathbf{r}_1, \mathbf{r}_2)}{\sqrt{G^{(1)}(\mathbf{r}_1, \mathbf{r}_1) G^{(1)}(\mathbf{r}_2, \mathbf{r}_2)}}. \tag{6.6}$$

Here $G^{(1)}$ is the first-order correlation function and corresponds to:

$$G^{(1)}(\mathbf{r}_1, \mathbf{r}_2) = \mathrm{Tr}\{\rho E^{(-)}(\mathbf{r}_1) E^{(+)}(\mathbf{r}_2)\} \tag{6.7}$$

where Tr indicates the trace, ρ is the density matrix operator, and $E^{(+)}$ and $E^{(-)}$ are field creation and annihilation operators, respectively.

Although spatial coherence properties have been extensively studied in semiconductor photon lasers, exciton–polariton lasers [166] and plasmon lasers [167], coherence of TMDC lasers have not been studied thus far, making it difficult to rule out localized excitons as a source of lasing. However, the large spatial area of the grating resonator, and the large photon flux above threshold, allow us to investigate the spatial coherence of the interlayer exciton emission. First-order spatial coherence measurements were performed using a continuous wave excitation laser and a retroreflector Michelson interferometer setup [168], where an image of the sample interferes with a centro-symmetrically inverted version of itself at the output with an intensity distribution $I^{\mathrm{int}}(\boldsymbol{r})$ (Figure 6.12(a)). Because of a small angle difference between the two beams, interference fringes are formed (Figure 6.12(b)) that correspond to slightly varying path length differences $2\pi z_0(\boldsymbol{r})/\lambda_0$ at different positions r across the images; z_0 is the initial position of the retroreflector.

Varying the path length of the interferometer, $I^{\mathrm{int}}(\boldsymbol{r})$ of each r oscillates, with the contrast of the oscillation proportional to the first-order spatial coherence, $g^{(1)}(\boldsymbol{r}, -\boldsymbol{r})$ (Figure 6.12(c)). We thus obtain spatial maps of $g^{(1)}(\boldsymbol{r}, -\boldsymbol{r})$. Below threshold, the emission is too weak for $g^{(1)}(\boldsymbol{r}, -\boldsymbol{r})$ measurements. Near threshold, the map is rather noisy without a clear pattern of $g^{(1)}(\boldsymbol{r}, -\boldsymbol{r})$ versus r (Figure 6.13(a), top panel). Above threshold, a clear pattern emerges, showing a high $g^{(1)}(\boldsymbol{r}, -\boldsymbol{r})$ near $r \approx 0$ that decays with increasing r and extends above the background fluctuations to about twice the laser spot size (Figure 6.13(b),

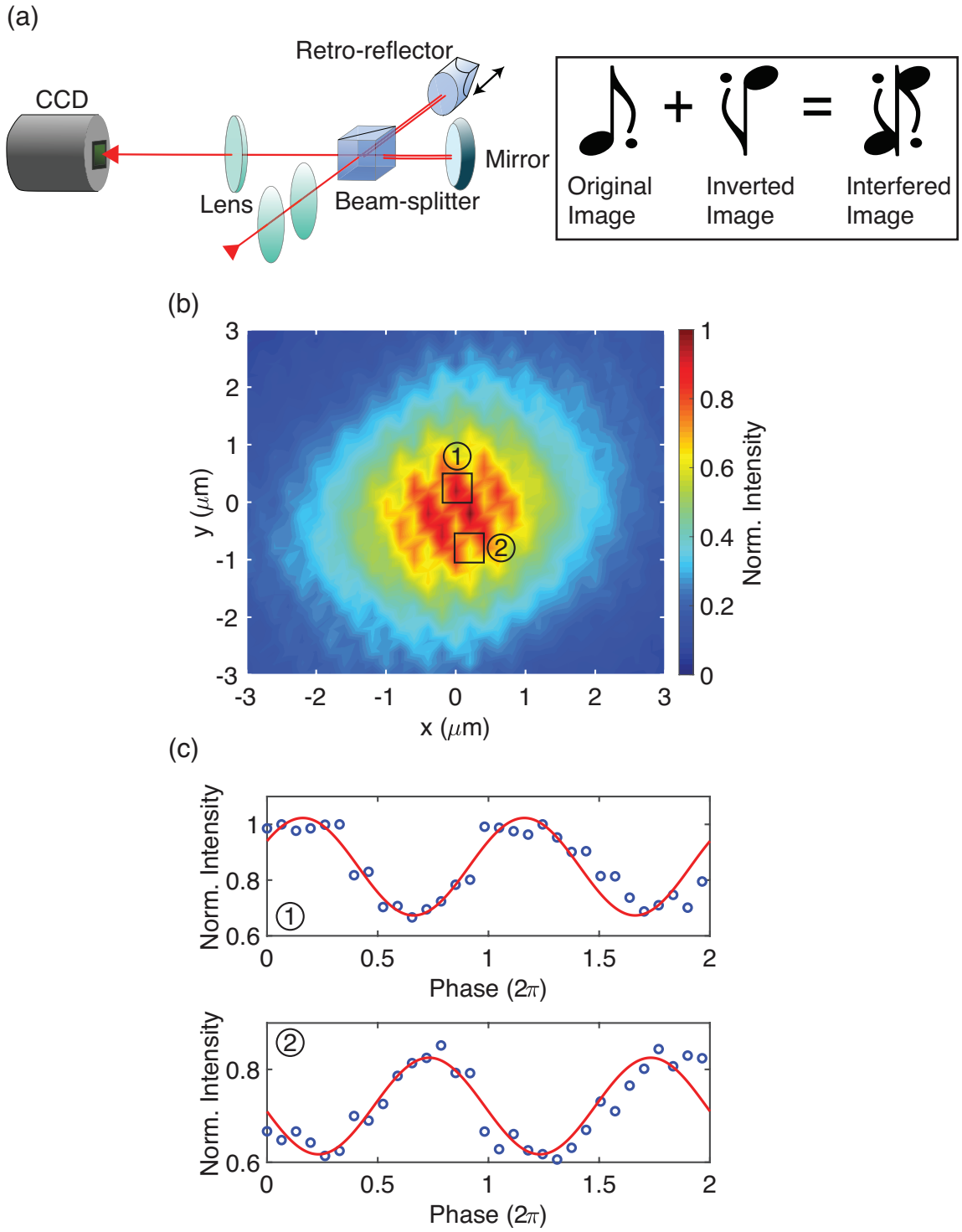

Figure 6.12: Michelson interferometer setup. (a) Left, schematic of the Michelson interferometer setup. Right, illustration of centro-symmetrically interfered images. (b) Typical interference pattern above P_{th} (20 μW). (c) Intensity plots of single pixels (labeled as squares 1 and 2 in (b)) as the retro-reflector position is scanned over a phase of 4π.

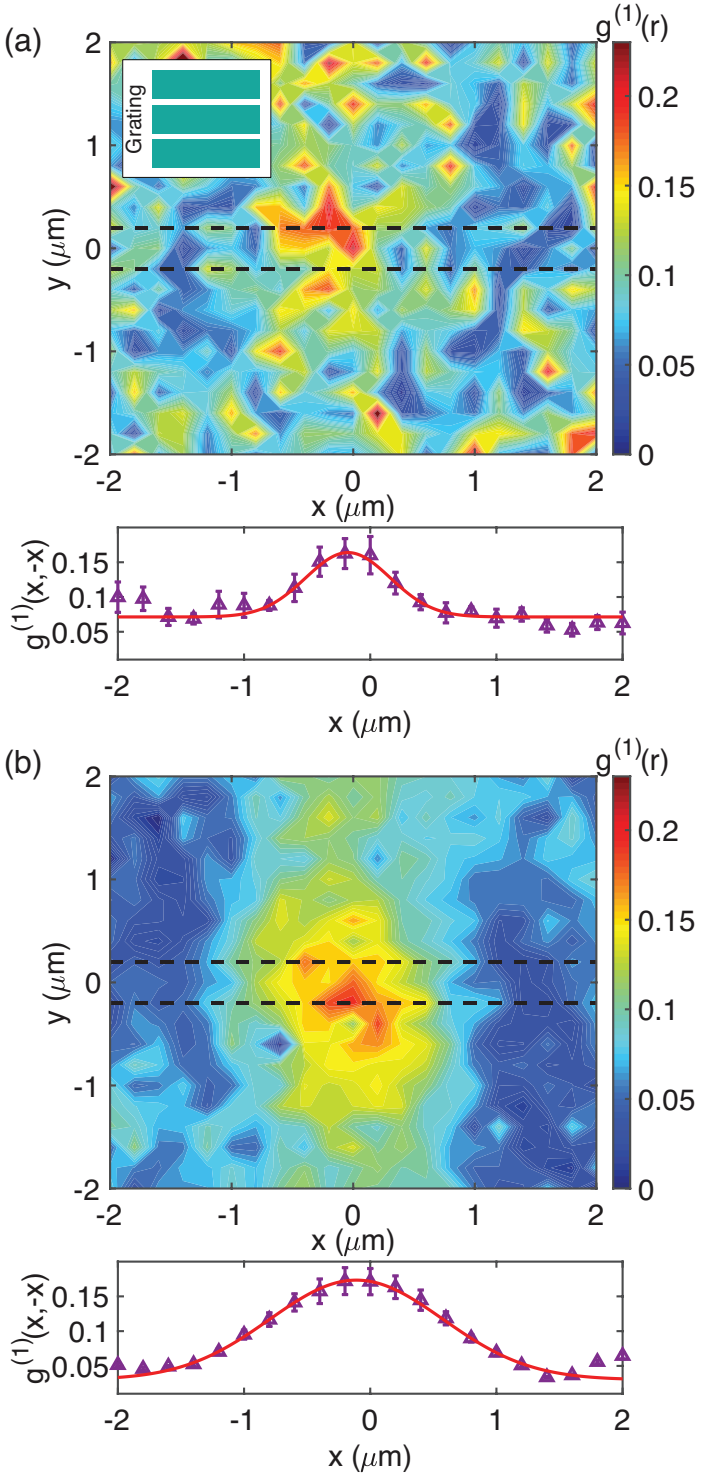

Figure 6.13: First-order coherence of the interlayer exciton laser. (a-b) Top, maps of $g^{(1)}(\boldsymbol{r}, -\boldsymbol{r})$ (a) near P_{th} (0.3 μW) and (b) above P_{th} (10 μW). Bottom, horizontal line-cuts of $g^{(1)}(\boldsymbol{r}, -\boldsymbol{r})$ integrated between the dashed lines in the maps above. The red line is the Gaussian fit used to extract the coherence length λ_c. The error bars correspond to the 95% confidence intervals of the sinusoidal fit, such as the ones shown in Figure 6.12(c). Inset in (a): illustration of the grating bar direction.

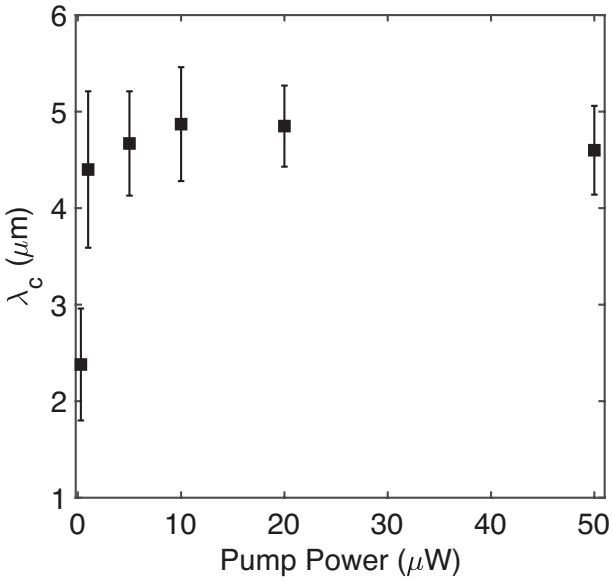

Figure 6.14: First-order coherence power dependence of the interlayer exciton laser. The coherence length λ_c versus the pump power. The error bars correspond to the 95% confidence interval of the Gaussian fit, such as the ones shown in Figures 6.13(a) and 6.13(b).

top panel).

To study the functional dependence of $g^{(1)}(\boldsymbol{r}, -\boldsymbol{r})$, we average over $y = \pm 0.2\mu$m and obtain $g^{(1)}(x, -x)$. As shown in the bottom panels of Figure 6.13(a) and 6.13(b), the decay of $g^{(1)}(x, -x)$ with x is clearly slower above threshold than below threshold. The plot of $g^{(1)}(x, -x)$ versus x is fitted well by a Gaussian function with the standard deviation σ as a fitting parameter. From the fits, we obtain the coherence length $\lambda_c = \sqrt{2\pi}\sigma$. As seen in Figure 6.14, λ_c increases abruptly across the threshold, from 2.38 μm near threshold to about 5 μm above threshold, confirming the formation of extended spatial coherence in the laser. Above threshold, the λ_c value remains largely unchanged, possibly limited by the laser spot size and carrier diffusion length. The λ_c value decreases slightly at the highest powers, possibly because of competition of multiple spatial modes in the absence of lateral confinement potentials. We note that the measured $g^{(1)}(x, -x)$ is much lower than the actual value, owing to difficulty in achieving good alignment.

6.4 Conclusion

We have demonstrated a 2D WSe_2-$MoSe_2$ heterobilayer laser on a grating cavity. A nonlinear increase in the output intensity and narrowing of the emission linewidth are measured as the photon number in the lasing mode reaches the order of unity. The carrier density at

threshold matches that for the transparency condition. The full coverage of gain medium by the cavity field enables a relatively large photon flux above threshold and a measurement of the extended spatial coherence of the device originating from the 2D gain medium. An abrupt increase of the spatial coherence to around 5 μm above threshold is measured, confirming that the lasing emission originates from an extended 2D gain medium – the interlayer excitons.

The injected carrier density at threshold is within an order of magnitude of the estimated transparency condition, suggesting band inversion between the $MoSe_2$ conduction band and the WSe_2 valence band as the gain mechanism. The type-II band alignment, resulting in charge separation and longer exciton lifetimes, may have facilitated the establishment of a population inversion. In addition, for heterobilayers, moiré lattices are expected [113, 19, 114, 115, 169]. By analogy to quantum dot lasers [170], localization of the interlayer excitons in a moiré lattice may lead to increased phase space density in the lasing mode for the same carrier density, as well as reduced non-radiative loss of the trapped interlayer excitons, enhancing the performance of heterobilayer lasers.

Future studies may clarify the role of moiré lattices in heterobilayer lasers. The present heterobilayer laser could be improved by reducing the inhomogeneous broadening of the gain medium via encapsulation with hexagonal boron nitride, improving the cavity Q, and reducing mode competition with lateral confinement of the cavity modes. Also, different combinations of van der Waals materials in the heterobilayer could be used to create interlayer exciton lasers of different wavelengths. Using cavities with lateral rotational invariance would allow a valley-polarized interlayer exciton laser to be realized. Finally, electrical tuning of the oscillator strength might allow fast modulation of the laser, and electrical injection could be implemented via atomically thin, bilayer p–n junctions [20, 21]. Adiabatic electrical tuning [171] might be used to explore coherent indirect exciton gases.

CHAPTER 7

Electrical and Structural Control of TMDC Monolayers and Heterobilayers

The versatility of 2D materials comes from the ability to change and control their properties using electrical field or band structure engineering. In this chapter, we present a collection of preliminary work on electrical gate tuning and bandgap engineering of TMDCs. We will discuss the gate-depenendent optical properties of monolayer and heterobilayer samples and introduce WS_2/$MoSe_2$ hybrid excitons.

7.1 Monolayer $MoSe_2$ gate control of exciton species

In monolayer TMDCs, introduction of charges can form stable lower energy trion states. Using gate contacts that change the doping density of the monolayer, we can control the relative emission intensities of the exciton and trion [102]. Here, we demonstrate gate-dependent changes in the relative PL emission intensities between exciton and trion in monolayer $MoSe_2$.

Figure 7.1(a) shows a schematic of the gated monolayer $MoSe_2$ device. Monolayer $MoSe_2$ was transferred onto a SiO_2 substrate using a dry transfer technique (Chapter 4 section 4.1.3). A stencil mask was aligned to the monolayer using a transfer stage and secured onto the substrate using a metal clip. 5 nm thick titanium adhesion layer and 200 nm thick gold layer were deposited onto the exposed regions on the sample. For the back gate contact, we deposited gold onto a small corner of the sample, and used silver paint to electrically connect the gold contact to the Si layer. The contacts were wire bonded to a PCB and connected to a source meter. An image of the final sample is shown in Figure 7.1(b).

We characterized the device at 5 K by performing a gate-dependent PL measurement. As shown in Figure 7.1(c) and 7.1(d), the sample is negatively doped at 0 V, as shown

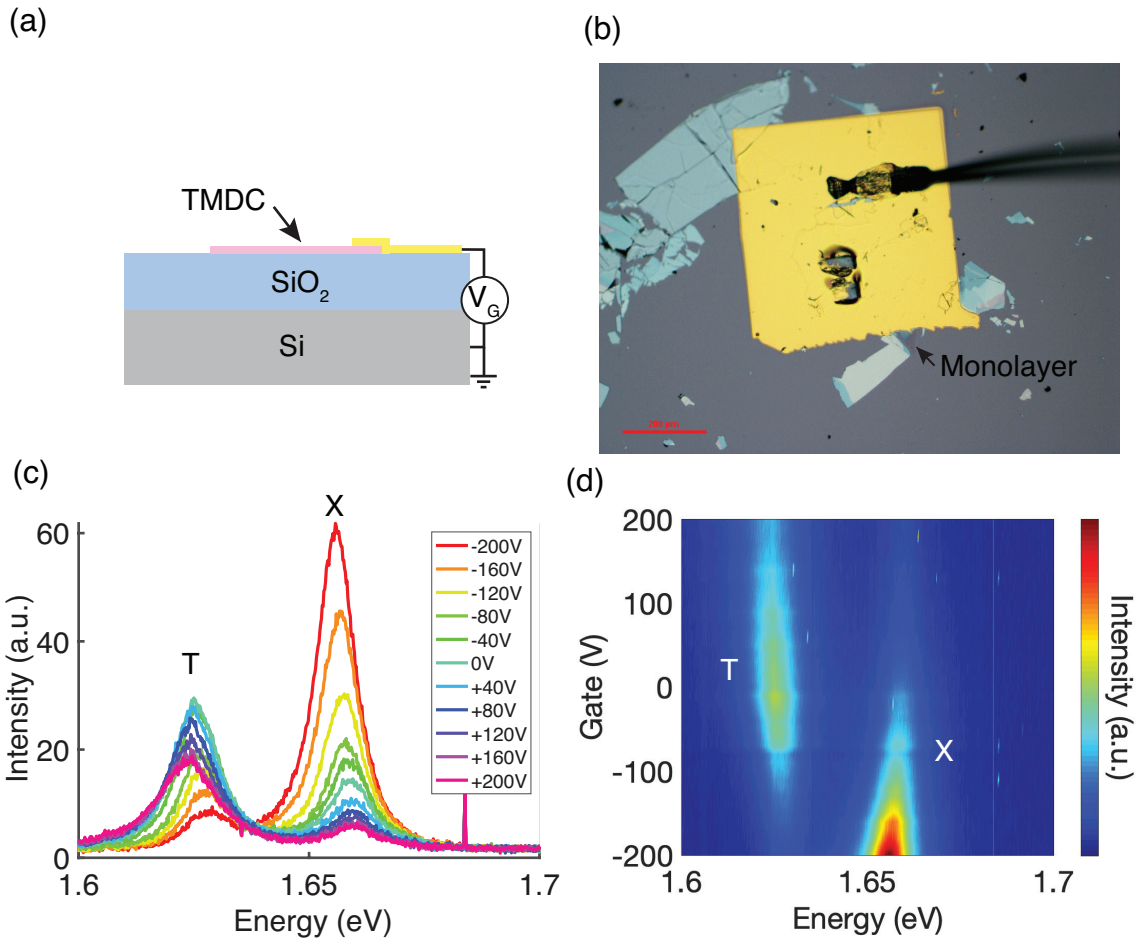

Figure 7.1: Electrical gating of $MoSe_2$. (a) Schematic of the gated monolayer $MoSe_2$. (b) Optical image of the sample. Gate-dependent PL spectra represented in (c) 1D and (d) 2D. X labels the exciton emission and T labels the trion emission.

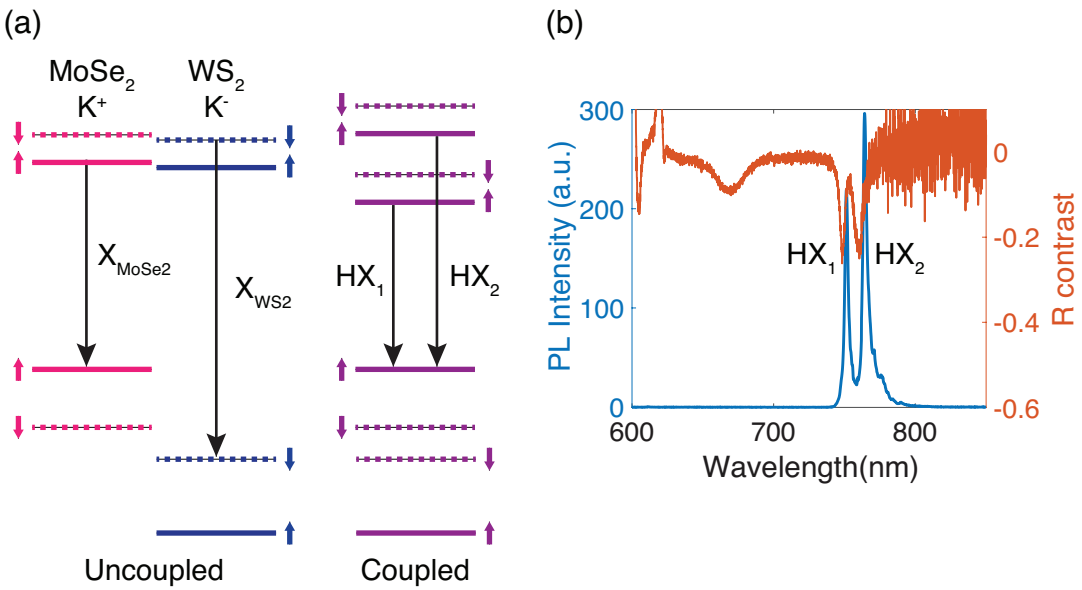

Figure 7.2: $WS_2/MoSe_2$ hybridized excitons. (a) Band alignment of the uncoupled and coupled heterobilayer. X_{MoSe2} (X_{WS2}) is the $MoSe_2$ (WS_2) A exciton transition. HX_1 and HX_2 are the hybridized exciton transitions. (b) PL and reflection spectra of the hybridized exciton.

by the dominant trion emission peak. At negative gate voltages, exciton emission is more dominant and the sample is close to charge neutral. These results demonstrate the *in situ* controllability of the exciton species using gate contacts.

7.2 $WS_2/MoSe_2$ hybridized excitons

The diversity of available TMDC materials and their bandgaps (Figure 2.9) in addition to the ease of forming heterostructures allow us to mix-and-match materials and change the electronic and optical properties. In particular, $WS_2/MoSe_2$ heterobilayer is unique because the conduction bands of the two materials are closely aligned in energy. This results in tunneling of the electrons between the conduction bands, which leads to coupling and hybridization of the intralayer and interlayer exciton states [172]. The hybridized excitons inherit strong oscillator strength from intralayer excitons and large interaction strength and gate tunability from interlayer excitons.

Figure 7.2 shows a band alignment diagram of the hybridized $WS_2/MoSe_2$ exciton states and the PL and reflection contrast measurements. In this example, HX_1 is the intralayer-like exciton and HX_2 is the interlayer-like exciton. PL measurement alone is insufficient to determine whether hybridized exciton states are formed because the trion emission is indistinguishable from the hybridized exciton emission and there could also

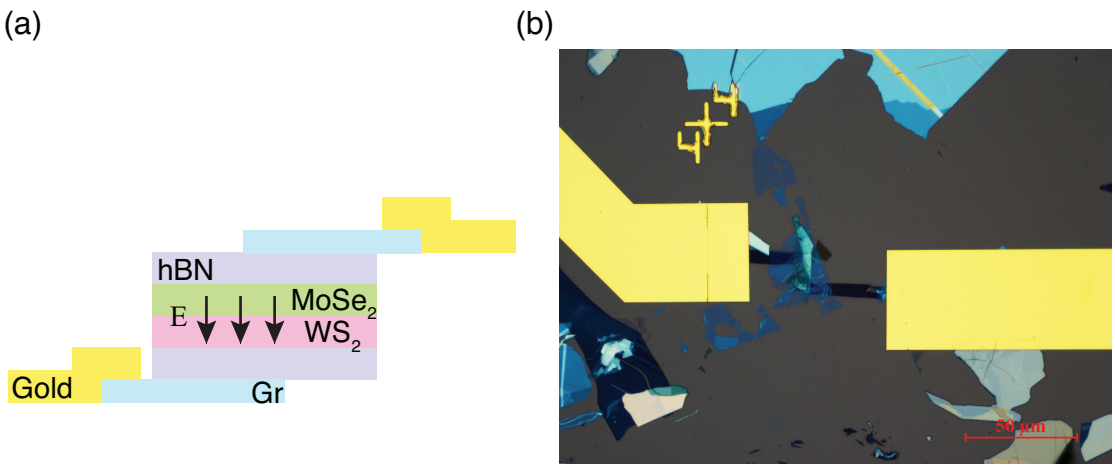

Figure 7.3: $WS_2/MoSe_2$ gated device. (a) Schematic illustration of the top and bottom-gated heterobilayer. E is the electricl field across the heterobilayer. (b) Optical microscope image of the device. The scale bar is 50 μm.

be defect-related emission. However, trion has a smaller oscillator strength than the hybridized excitons and does not produce a strong absorption signal in the reflection contrast measurements. Thus, two distinct signals in the reflection contrast near the $MoSe_2$ exciton resonance energy signals the formation of hybridized excitons (Figure 7.2(b)).

7.2.1 Electrical control

The conduction bands are closely aligned in $WS_2/MoSe_2$ heterobilayer and applying an external electric field will induce a Stark shift of the conduction and valence bands to change the excitonic states to switch from interlayer-like to intralayer-like exctions [111, 173]. This can be useful for controlling the light-matter and many-body interactions in 2D photonic devices.

Here, we demonstrate some preliminary results on electrically controlled $WS_2/MoSe_2$ devices. The sample consists of a hBN encapsulated, rotationally aligned $WS_2/MoSe_2$ heterobilayer with a few-layer graphene top and bottom contacts. The graphene contacts are connected to a gold contact pad patterned using EBL (Chapter 4 section 4.5). Figure 7.3 shows the schematic diagram and the optical image of the device.

As external electric field is applied to the device, the interlayer exciton energy levels shift proportionally to the magnitude of the electric field, whereas the intralayer exciton energy stays the same. When the conduction bands of WS_2 and $MoSe_2$ are near resonant, the hybridization of the energy levels manifests as anti-crossings of the interlayer and intralayer exciton energies. Figure 7.4 shows the voltage-dependent reflection contrast measurements. Note that the linewidths of the reflection dips are large, possibly due to

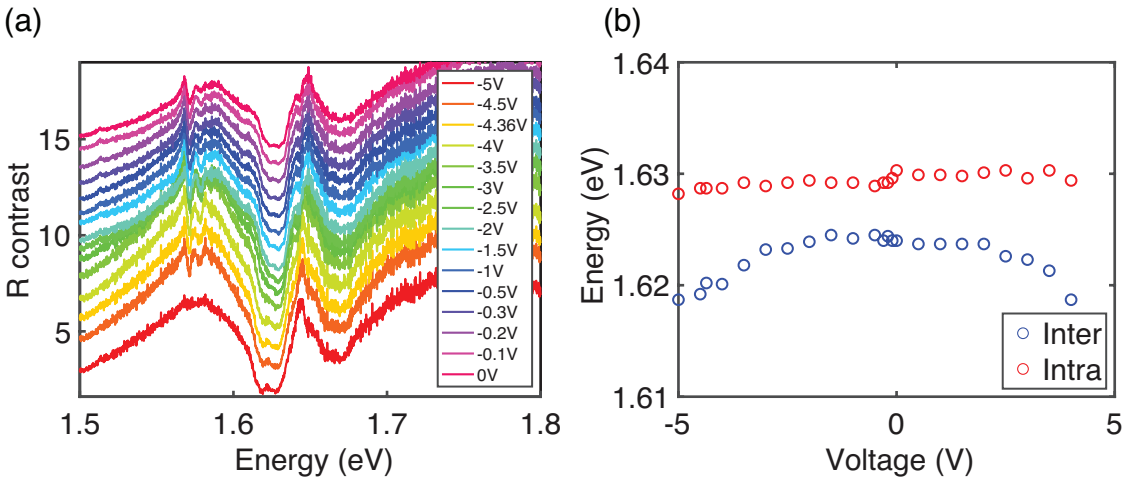

Figure 7.4: $WS_2/MoSe_2$ gate-dependent reflection contrast measurement. (a) Reflection contrast spectra at different gate voltages. (b) Gate-dependent interlayer and intralayer exciton energies.

the inhomogeneity introduced during the fabrication procedure. More work is required to optimize the fabrication and testing procedures to produce a sample with higher optical quality.

7.2.2 Cavity control

Another way of modifying and controlling the $WS_2/MoSe_2$ hybridized excitons is to use a cavity. The formation of moiré excitons in the heterobilayer combined with the cavity confinement can result in moiré exciton-polaritons confined in all three dimensions with strong nonlinearity [174]. Using the transferrable DBR cavity with a high Q-factor could enable sufficient thermalization of exciton-polaritons to allow condensation. Here, we present the preliminary result that demonstrates cavity coupling of $WS_2/MoSe_2$. It is critical to have a clean sample with very few impurities or bulk 2D material flakes. We used the PC transfer method (Chapter 4 section 4.1.3) to deposit a hBN encapsulated $WS_2/MoSe_2$ heterobilayer onto the SiO_2/TiO_2 bottom DBR. After performing PL and reflection contrast measurements to characterize the sample, we transferred the ZnS/MgF_2 transferrable DBR on top (Chapter 4 section 4.3.1). The dispersion of the $WS_2/MoSe_2$ hybridized excitons coupled

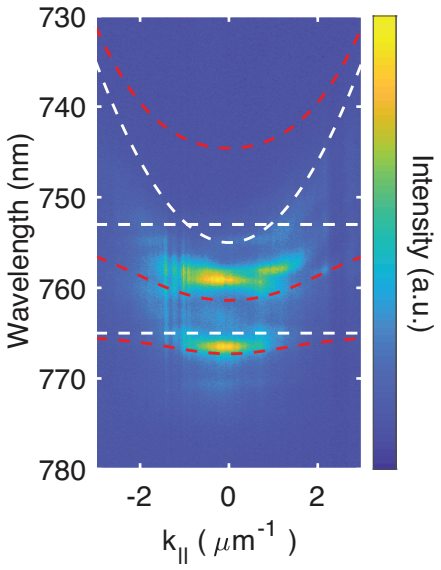

Figure 7.5: Angle-resolved PL spectrum of WS_2/$MoSe_2$ coupled to a transferrable DBR cavity. Dashed white lines are the cavity and exciton dispersions and the dashed red lines are the upper, middle, and lower polariton dispersions.

to a cavity can be modeled by a coupled oscillator model with a Hamiltoninan:

$$H = \begin{bmatrix} E_{HX1} & 0 & \Omega_1 \\ 0 & E_{HX1} & \Omega_2 \\ \Omega_1 & \Omega_2 & E_c \end{bmatrix}. \tag{7.1}$$

Here, $E_{HX1,2}$ are hybridized exction resonances, E_c is the cavity resonance energy, and $\Omega_{1,2}$ are coupling strengths. This results in a upper, middle and lower polariton dispersions. Figure 7.5 shows the angle-resolved PL spectrum of the cavity-coupled WS_2/$MoSe_2$. Detailed material characterization, modeling, and measurements are required to correctly identify the different states.

7.3 Conclusion

We have demonstrated several ways of controlling the properties of TMDC monolayers and heterobilayers. Doping monolayer $MoSe_2$ can be used to switch the excitonic state from neutral excitons to trions and vice versa. Electrial gating of heterobilayer WS_2/$MoSe_2$ can tune the energies of the hybridized excitons, and cavities can be used to form exciton-polariton states. Building off of these preliminary results, we can further demonstrate con-

trollable 2D photonics.

CHAPTER 8

Conclusion and Outlook

8.1 Summary

Atomically-thin 2D semiconductor materials serve as a promising platform for the next generation of photonic devices that are more compact and efficient than existing technology. Specifically, this thesis focused on developing techniques for fabricating high quality TMDC samples, engineering new types of cavities, and performing optical measurements to characterize the photonic devices. We demonstrate novel strong coupling and photon lasing devices with TMDC monolayers and heterobilayers.

First, we developed a new method of creating high-Q microcavities for TMDC materials. Reliably producing high-Q DBR cavities for TMDCs is challenging, and previously has not been demonstrated for fully hBN encapsulated TMDCs. We demonstrate a high-Q DBR cavity with a transferrable, high-reflectance top DBR. Systematic cavity characterization measurements show that our method reliably produces DBR cavities with Q-factors greater than 2,000 and up to 10,000. Reflection and PL measurements show strong coupling with a fully hBN encapsulated monolayer $MoSe_2$.

We also demonstrated a novel semiconductor photon laser with a WSe_2-$MoSe_2$ heterobilayer. This is one of the first demonstration of lasing in TMDC heterobilayers. To verify lasing, we measured a nonlinear increase of the emission intensity as a function of pump power, accompanied by a linewidth narrowing at the threshold power. The lasing device shows a sudden increase in the spatial coherence length at threshold power, indicating the formation of extended spatial coherence.

8.2 Future work

Exciton-polariton condensation occurs when many polaritons occupy the same quantum state. Due to their light effective mass, exciton-polariton condensation can have a critical

temperature up to four orders of magnitude higher than that of atomic BECs, theoretically allowing condensation at room temperature. From a practical aspect, exciton-polaritons can provide highly coherent and monochromatic light with a very low lasing threshold, making them energy efficient. Exciton-polariton condensation has been explored extensively in GaAs but still remains elusive in the TMDC system.

This thesis lays the groundwork for exploring exciton-polariton condensation in TMDCs, but more work is needed to realize condensation, and better yet, room temperature condensation. The high-Q transferrable DBR cavity exciton-polariton could be an ideal platform, and careful power dependence measurements under various pumping conditions could reveal more information about the nonlinearity of the polariton emission.

Another possibility is to utilize the moiré lattice confinement potential to enhance the nonlinearity of the exciton-polaritons and encourage condensation. In Chapter 7, we show preliminary work on using a WS_2/$MoSe_2$ hybridized excitons to utilize the strong oscillator strength of the hybrid excitons and the formation of a moiré superlattice. Systematic optical studies and careful optimization of fabrication procedures are required to take a step closer to condensation. Another direction, not shown in this thesis, is to use a type-I band alignment of molybdenum ditelluride ($MoTe_2$)/WSe_2 heterobilayer to demonstrate cavity coupling of an intralayer moiré lattice exciton. Some work has been done to prepare the $MoTe_2$/WSe_2 sample and perform cursory measurements, but more work is needed to build the measurement setup for this device.

Combining electrical and cavity controls in one device provides a powerful tool that expands the parameter space of measurements and increases the chances of finding the ideal conditions that will lead to exciton-polariton condensation. However, incorporating metal contacts to cavity structures is challenging because the metal absorption can destroy the cavity mode. Thus, finding ways to overcome this challenge is an important next step.

BIBLIOGRAPHY

[1] Paik, E. Y., Zhang, L., Hou, S., Zhao, H., Chou, Y.-H., Forrest, S. R., and Deng, H., "High-Q Microcavity for van der Waals Semiconductor Polaritons Using a Transferrable Mirror," Manuscript submitted to *Advanced Optical Materials*.

[2] Paik, E. Y., Zhang, L., Burg, G. W., Gogna, R., Tutuc, E., and Deng, H., "Interlayer exciton laser of extended spatial coherence in atomically thin heterostructures," *Nature*, Vol. 576, No. 7785, Dec. 2019, pp. 80–84.

[3] Regan, E. C., Wang, D., Paik, E. Y., Zeng, Y., Zhang, L., Zhu, J., MacDonald, A. H., Deng, H., and Wang, F., "Emerging exciton physics in transition metal dichalcogenide heterobilayers," *Nature Reviews Materials*, May 2022.

[4] Liu, Y., Weiss, N. O., Duan, X., Cheng, H.-C., Huang, Y., and Duan, X., "Van der Waals heterostructures and devices," *Nature Reviews Materials*, Vol. 1, No. 9, July 2016, pp. 1–17, Number: 9 Publisher: Nature Publishing Group.

[5] Baranov, D. G., Wersäll, M., Cuadra, J., Antosiewicz, T. J., and Shegai, T., "Novel Nanostructures and Materials for Strong Light–Matter Interactions," *ACS Photonics*, Vol. 5, No. 1, 2018, pp. 24–42.

[6] Splendiani, A., Sun, L., Zhang, Y., Li, T., Kim, J., Chim, C.-Y., Galli, G., and Wang, F., "Emerging Photoluminescence in Monolayer MoS2," *Nano Letters*, Vol. 10, No. 4, 2010, pp. 1271–1275, PMID: 20229981.

[7] Chernikov, A., Berkelbach, T. C., Hill, H. M., Rigosi, A., Li, Y., Aslan, O. B., Reichman, D. R., Hybertsen, M. S., and Heinz, T. F., "Exciton Binding Energy and Nonhydrogenic Rydberg Series in Monolayer WS_2," *Phys. Rev. Lett.*, Vol. 113, Aug 2014, pp. 076802.

[8] Moody, G., Kavir Dass, C., Hao, K., Chen, C.-H., Li, L.-J., Singh, A., Tran, K., Clark, G., Xu, X., Berghäuser, G., Malic, E., Knorr, A., and Li, X., "Intrinsic homogeneous linewidth and broadening mechanisms of excitons in monolayer transition metal dichalcogenides," *Nature Communications*, Vol. 6, No. 1, Sep 2015, pp. 8315.

[9] Liu, Y., Huang, Y., and Duan, X., "Van der Waals integration before and beyond two-dimensional materials," *Nature*, Vol. 567, No. 7748, Mar 2019, pp. 323–333.

[10] Kang, J., Tongay, S., Zhou, J., Li, J., and Wu, J., "Band offsets and heterostructures of two-dimensional semiconductors," *Applied Physics Letters*, Vol. 102, No. 1, 2013, pp. 012111.

[11] Wilson, N. R., Nguyen, P. V., Seyler, K., Rivera, P., Marsden, A. J., Laker, Z. P. L., Constantinescu, G. C., Kandyba, V., Barinov, A., Hine, N. D. M., Xu, X., and Cobden, D. H., "Determination of band offsets, hybridization, and exciton binding in 2D semiconductor heterostructures," *Science Advances*, Vol. 3, No. 2, 2017, pp. e1601832.

[12] Yu, H., Liu, G.-B., and Yao, W., "Brightened spin-triplet interlayer excitons and optical selection rules in van der Waals heterobilayers," *2D Materials*, Vol. 5, No. 3, May 2018, pp. 035021.

[13] Grepstad, J. O., Greve, M. M., Holst, B., Johansen, I.-R., Solgaard, O., and Sudbø, A., "Finite-size limitations on Quality Factor of guided resonance modes in 2D Photonic Crystals," *Opt. Express*, Vol. 21, No. 20, Oct 2013, pp. 23640–23654.

[14] Deng, H., Haug, H., and Yamamoto, Y., "Exciton-polariton Bose-Einstein condensation," *Rev. Mod. Phys.*, Vol. 82, May 2010, pp. 1489–1537.

[15] Jenkins, T., "A brief history of ... semiconductors," *Physics Education*, Vol. 40, No. 5, sep 2005, pp. 430–439.

[16] Novoselov, K. S., Geim, A. K., Morozov, S. V., Jiang, D., Zhang, Y., Dubonos, S. V., Grigorieva, I. V., and Firsov, A. A., "Electric Field Effect in Atomically Thin Carbon Films," *Science*, Vol. 306, No. 5696, 2004, pp. 666–669.

[17] Mak, K. F. and Shan, J., "Photonics and optoelectronics of 2D semiconductor transition metal dichalcogenides," *Nature Photonics*, Vol. 10, No. 4, Apr 2016, pp. 216–226.

[18] Fogler, M. M., Butov, L. V., and Novoselov, K. S., "High-temperature superfluidity with indirect excitons in van der Waals heterostructures," *Nature Communications*, Vol. 5, No. 1, Jul 2014, pp. 4555.

[19] Wu, F., Lovorn, T., and MacDonald, A. H., "Theory of optical absorption by interlayer excitons in transition metal dichalcogenide heterobilayers," *Phys. Rev. B*, Vol. 97, Jan 2018, pp. 035306.

[20] Lee, C.-H., Lee, G.-H., van der Zande, A. M., Chen, W., Li, Y., Han, M., Cui, X., Arefe, G., Nuckolls, C., Heinz, T. F., Guo, J., Hone, J., and Kim, P., "Atomically thin p–n junctions with van der Waals heterointerfaces," *Nature Nanotechnology*, Vol. 9, No. 9, Sep 2014, pp. 676–681.

[21] Ross, J. S., Rivera, P., Schaibley, J., Lee-Wong, E., Yu, H., Taniguchi, T., Watanabe, K., Yan, J., Mandrus, D., Cobden, D., Yao, W., and Xu, X., "Interlayer Exciton Optoelectronics in a 2D Heterostructure p–n Junction," *Nano Letters*, Vol. 17, No. 2, 2017, pp. 638–643, PMID: 28006106.

[22] Jauregui, L. A., Joe, A. Y., Pistunova, K., Wild, D. S., High, A. A., Zhou, Y., Scuri, G., Greve, K. D., Sushko, A., Yu, C.-H., Taniguchi, T., Watanabe, K., Needleman, D. J., Lukin, M. D., Park, H., and Kim, P., "Electrical control of interlayer exciton dynamics in atomically thin heterostructures," *Science*, Vol. 366, No. 6467, 2019, pp. 870–875.

[23] Frindt, R. F., "Single Crystals of MoS2 Several Molecular Layers Thick," *Journal of Applied Physics*, Vol. 37, No. 4, 1966, pp. 1928–1929.

[24] Wilson, J. A. and Yoffe, A. D., "The transition metal dichalcogenides discussion and interpretation of the observed optical, electrical and structural properties," *Advances in Physics*, Vol. 18, No. 73, 1969, pp. 193–335.

[25] Dias, A. C., Qu, F., Azevedo, D. L., and Fu, J., "Band structure of monolayer transition-metal dichalcogenides and topological properties of their nanoribbons: Next-nearest-neighbor hopping," *Phys. Rev. B*, Vol. 98, Aug 2018, pp. 075202.

[26] Mak, K. F., Lee, C., Hone, J., Shan, J., and Heinz, T. F., "Atomically Thin MoS_2: A New Direct-Gap Semiconductor," *Phys. Rev. Lett.*, Vol. 105, Sep 2010, pp. 136805.

[27] Chhowalla, M., Shin, H. S., Eda, G., Li, L.-J., Loh, K. P., and Zhang, H., "The chemistry of two-dimensional layered transition metal dichalcogenide nanosheets," *Nature Chemistry*, Vol. 5, No. 4, Apr 2013, pp. 263–275.

[28] Riva, C., Peeters, F. M., and Varga, K., "Excitons and charged excitons in semiconductor quantum wells," *Phys. Rev. B*, Vol. 61, May 2000, pp. 13873–13881.

[29] Mak, K. F., He, K., Lee, C., Lee, G. H., Hone, J., Heinz, T. F., and Shan, J., "Tightly bound trions in monolayer MoS2," *Nature Materials*, Vol. 12, No. 3, Mar 2013, pp. 207–211.

[30] Berkelbach, T. C., Hybertsen, M. S., and Reichman, D. R., "Theory of neutral and charged excitons in monolayer transition metal dichalcogenides," *Phys. Rev. B*, Vol. 88, Jul 2013, pp. 045318.

[31] Dhara, S., Chakraborty, C., Goodfellow, K. M., Qiu, L., O'Loughlin, T. A., Wicks, G. W., Bhattacharjee, S., and Vamivakas, A. N., "Anomalous dispersion of microcavity trion-polaritons," *Nature Physics*, Vol. 14, No. 2, Feb 2018, pp. 130–133.

[32] Emmanuele, R. P. A., Sich, M., Kyriienko, O., Shahnazaryan, V., Withers, F., Catanzaro, A., Walker, P. M., Benimetskiy, F. A., Skolnick, M. S., Tartakovskii, A. I., Shelykh, I. A., and Krizhanovskii, D. N., "Highly nonlinear trion-polaritons in a monolayer semiconductor," *Nature Communications*, Vol. 11, No. 1, Jul 2020, pp. 3589.

[33] Kyriienko, O., Krizhanovskii, D. N., and Shelykh, I. A., "Nonlinear Quantum Optics with Trion Polaritons in 2D Monolayers: Conventional and Unconventional Photon Blockade," *Phys. Rev. Lett.*, Vol. 125, Nov 2020, pp. 197402.

[34] Wang, G., Chernikov, A., Glazov, M. M., Heinz, T. F., Marie, X., Amand, T., and Urbaszek, B., "Colloquium: Excitons in atomically thin transition metal dichalcogenides," *Rev. Mod. Phys.*, Vol. 90, Apr 2018, pp. 021001.

[35] Haug, H. and Koch, S. W., *Quantum theory of the optical and electronic properties of semiconductors*, World Scientific, 4th ed., 2004.

[36] He, K., Kumar, N., Zhao, L., Wang, Z., Mak, K. F., Zhao, H., and Shan, J., "Tightly Bound Excitons in Monolayer WSe_2," *Phys. Rev. Lett.*, Vol. 113, Jul 2014, pp. 026803.

[37] Cudazzo, P., Tokatly, I. V., and Rubio, A., "Dielectric screening in two-dimensional insulators: Implications for excitonic and impurity states in graphane," *Phys. Rev. B*, Vol. 84, Aug 2011, pp. 085406.

[38] García Flórez, F., Siebbeles, L. D. A., and Stoof, H. T. C., "Effects of material thickness and surrounding dielectric medium on Coulomb interactions and two-dimensional excitons," *Phys. Rev. B*, Vol. 102, Sep 2020, pp. 125303.

[39] Latini, S., Olsen, T., and Thygesen, K. S., "Excitons in van der Waals heterostructures: The important role of dielectric screening," *Phys. Rev. B*, Vol. 92, Dec 2015, pp. 245123.

[40] Rytova, N. S., "Screened potential of a point charge in a thin film," 2018.

[41] Keldysh, L. V., "Coulomb interaction in thin semiconductor and semimetal films," *Soviet Journal of Experimental and Theoretical Physics Letters*, Vol. 29, June 1979, pp. 658.

[42] Ugeda, M. M., Bradley, A. J., Shi, S.-F., da Jornada, F. H., Zhang, Y., Qiu, D. Y., Ruan, W., Mo, S.-K., Hussain, Z., Shen, Z.-X., Wang, F., Louie, S. G., and Crommie, M. F., "Giant bandgap renormalization and excitonic effects in a monolayer transition metal dichalcogenide semiconductor," *Nature Materials*, Vol. 13, No. 12, Dec 2014, pp. 1091–1095.

[43] Gu, J., Walther, V., Waldecker, L., Rhodes, D., Raja, A., Hone, J. C., Heinz, T. F., Kéna-Cohen, S., Pohl, T., and Menon, V. M., "Enhanced nonlinear interaction of polaritons via excitonic Rydberg states in monolayer WSe2," *Nature Communications*, Vol. 12, No. 1, Apr 2021, pp. 2269.

[44] Klingshirn, C. F., *Semiconductor Optics*, Springer, 4th ed., 2012.

[45] Pelant, I. and Valenta, J., *Luminescence spectroscopy of semiconductors*, Oxford University Press, 2012.

[46] Yang, X. L., Guo, S. H., Chan, F. T., Wong, K. W., and Ching, W. Y., "Analytic solution of a two-dimensional hydrogen atom. I. Nonrelativistic theory," *Phys. Rev. A*, Vol. 43, Feb 1991, pp. 1186–1196.

[47] Cheiwchanchamnangij, T. and Lambrecht, W. R. L., "Quasiparticle band structure calculation of monolayer, bilayer, and bulk MoS_2," *Phys. Rev. B*, Vol. 85, May 2012, pp. 205302.

[48] Edvinsson, T., "Optical quantum confinement and photocatalytic properties in two-, one- and zero-dimensional nanostructures," *Royal Society open science*, Vol. 5, No. 9, Sept. 2018, pp. 180387–180387, Publisher: The Royal Society.

[49] Malic, E., Selig, M., Feierabend, M., Brem, S., Christiansen, D., Wendler, F., Knorr, A., and Berghäuser, G., "Dark excitons in transition metal dichalcogenides," *Phys. Rev. Materials*, Vol. 2, Jan 2018, pp. 014002.

[50] Zhang, X.-X., You, Y., Zhao, S. Y. F., and Heinz, T. F., "Experimental Evidence for Dark Excitons in Monolayer WSe_2," *Phys. Rev. Lett.*, Vol. 115, Dec 2015, pp. 257403.

[51] Glazov, M. M., Amand, T., Marie, X., Lagarde, D., Bouet, L., and Urbaszek, B., "Exciton fine structure and spin decoherence in monolayers of transition metal dichalcogenides," *Phys. Rev. B*, Vol. 89, May 2014, pp. 201302.

[52] Palummo, M., Bernardi, M., and Grossman, J. C., "Exciton Radiative Lifetimes in Two-Dimensional Transition Metal Dichalcogenides," *Nano Letters*, Vol. 15, No. 5, 2015, pp. 2794–2800, PMID: 25798735.

[53] Deveaud, B., Clérot, F., Roy, N., Satzke, K., Sermage, B., and Katzer, D. S., "Enhanced radiative recombination of free excitons in GaAs quantum wells," *Phys. Rev. Lett.*, Vol. 67, Oct 1991, pp. 2355–2358.

[54] Jakubczyk, T., Delmonte, V., Koperski, M., Nogajewski, K., Faugeras, C., Langbein, W., Potemski, M., and Kasprzak, J., "Radiatively Limited Dephasing and Exciton Dynamics in MoSe2 Monolayers Revealed with Four-Wave Mixing Microscopy," *Nano Letters*, Vol. 16, No. 9, 2016, pp. 5333–5339, PMID: 27517124.

[55] Poellmann, C., Steinleitner, P., Leierseder, U., Nagler, P., Plechinger, G., Porer, M., Bratschitsch, R., Schüller, C., Korn, T., and Huber, R., "Resonant internal quantum transitions and femtosecond radiative decay of excitons in monolayer WSe2," *Nature Materials*, Vol. 14, No. 9, Sep 2015, pp. 889–893.

[56] Robert, C., Lagarde, D., Cadiz, F., Wang, G., Lassagne, B., Amand, T., Balocchi, A., Renucci, P., Tongay, S., Urbaszek, B., and Marie, X., "Exciton radiative lifetime in transition metal dichalcogenide monolayers," *Phys. Rev. B*, Vol. 93, May 2016, pp. 205423.

[57] Cadiz, F., Courtade, E., Robert, C., Wang, G., Shen, Y., Cai, H., Taniguchi, T., Watanabe, K., Carrere, H., Lagarde, D., Manca, M., Amand, T., Renucci, P., Tongay, S., Marie, X., and Urbaszek, B., "Excitonic Linewidth Approaching the Homogeneous Limit in MoS_2-Based van der Waals Heterostructures," *Phys. Rev. X*, Vol. 7, May 2017, pp. 021026.

[58] Fang, H. H., Han, B., Robert, C., Semina, M. A., Lagarde, D., Courtade, E., Taniguchi, T., Watanabe, K., Amand, T., Urbaszek, B., Glazov, M. M., and Marie, X., "Control of the Exciton Radiative Lifetime in van der Waals Heterostructures," *Phys. Rev. Lett.*, Vol. 123, Aug 2019, pp. 067401.

[59] Martin, E. W., Horng, J., Ruth, H. G., Paik, E., Wentzel, M.-H., Deng, H., and Cundiff, S. T., "Encapsulation Narrows and Preserves the Excitonic Homogeneous Linewidth of Exfoliated Monolayer $MoSe_2$," *Phys. Rev. Applied*, Vol. 14, Aug 2020, pp. 021002.

[60] Zhu, Z. Y., Cheng, Y. C., and Schwingenschlögl, U., "Giant spin-orbit-induced spin splitting in two-dimensional transition-metal dichalcogenide semiconductors," *Phys. Rev. B*, Vol. 84, Oct 2011, pp. 153402.

[61] Xiao, D., Liu, G.-B., Feng, W., Xu, X., and Yao, W., "Coupled Spin and Valley Physics in Monolayers of MoS_2 and Other Group-VI Dichalcogenides," *Phys. Rev. Lett.*, Vol. 108, May 2012, pp. 196802.

[62] Wang, G., Robert, C., Suslu, A., Chen, B., Yang, S., Alamdari, S., Gerber, I. C., Amand, T., Marie, X., Tongay, S., and Urbaszek, B., "Spin-orbit engineering in transition metal dichalcogenide alloy monolayers," *Nature Communications*, Vol. 6, No. 1, Dec. 2015, pp. 10110, Number: 1 Publisher: Nature Publishing Group.

[63] Berry, M. V., "Quantal phase factors accompanying adiabatic changes," *Proceedings of the Royal Society of London. A. Mathematical and Physical Sciences*, Vol. 392, No. 1802, 1984, pp. 45–57.

[64] Xiao, D., Chang, M.-C., and Niu, Q., "Berry phase effects on electronic properties," *Rev. Mod. Phys.*, Vol. 82, Jul 2010, pp. 1959–2007.

[65] Mak, K. F., Xiao, D., and Shan, J., "Light–valley interactions in 2D semiconductors," *Nature Photonics*, Vol. 12, No. 8, Aug 2018, pp. 451–460.

[66] Schaibley, J. R., Yu, H., Clark, G., Rivera, P., Ross, J. S., Seyler, K. L., Yao, W., and Xu, X., "Valleytronics in 2D materials," *Nature Reviews Materials*, Vol. 1, No. 11, Nov. 2016, pp. 16055.

[67] Islam, M. N., Hillman, R. L., Miller, D. A. B., Chemla, D. S., Gossard, A. C., and English, J. H., "Electroabsorption in GaAs/AlGaAs coupled quantum well waveguides," *Applied Physics Letters*, Vol. 50, No. 16, 1987, pp. 1098–1100.

[68] Wang, Z., Chiu, Y.-H., Honz, K., Mak, K. F., and Shan, J., "Electrical Tuning of Interlayer Exciton Gases in WSe2 Bilayers," *Nano Letters*, Vol. 18, No. 1, 2018, pp. 137–143, PMID: 29240440.

[69] Mak, K. F. and Shan, J., "Opportunities and challenges of interlayer exciton control and manipulation," *Nature Nanotechnology*, Vol. 13, No. 11, Nov 2018, pp. 974–976.

[70] Ciarrocchi, A., Unuchek, D., Avsar, A., Watanabe, K., Taniguchi, T., and Kis, A., "Polarization switching and electrical control of interlayer excitons in two-dimensional van der Waals heterostructures," *Nature Photonics*, Vol. 13, No. 2, Feb 2019, pp. 131–136.

[71] Huang, Z., Zhao, Y., Bo, T., Chu, Y., Tian, J., Liu, L., Yuan, Y., Wu, F., Zhao, J., Xian, L., Watanabe, K., Taniguchi, T., Yang, R., Shi, D., Du, L., Sun, Z., Meng, S., Yang, W., and Zhang, G., "Spatially indirect intervalley excitons in bilayer $\mathrm{WSe_2}$," *Phys. Rev. B*, Vol. 105, Jan 2022, pp. L041409.

[72] Eisenstein, J. P. and MacDonald, A. H., "Bose–Einstein condensation of excitons in bilayer electron systems," *Nature*, Vol. 432, No. 7018, Dec 2004, pp. 691–694.

[73] Wang, Z., Rhodes, D. A., Watanabe, K., Taniguchi, T., Hone, J. C., Shan, J., and Mak, K. F., "Evidence of high-temperature exciton condensation in two-dimensional atomic double layers," *Nature*, Vol. 574, No. 7776, Oct 2019, pp. 76–80.

[74] Shi, Q., Shih, E.-M., Rhodes, D., Kim, B., Barmak, K., Watanabe, K., Taniguchi, T., Papić, Z., Abanin, D. A., Hone, J., and Dean, C. R., "Bilayer WSe2 as a natural platform for interlayer exciton condensates in the strong coupling limit," *Nature Nanotechnology*, Apr 2022.

[75] Li, J. I. A., Taniguchi, T., Watanabe, K., Hone, J., and Dean, C. R., "Excitonic superfluid phase in double bilayer graphene," *Nature Physics*, Vol. 13, No. 8, Aug 2017, pp. 751–755.

[76] Liu, X., Watanabe, K., Taniguchi, T., Halperin, B. I., and Kim, P., "Quantum Hall drag of exciton condensate in graphene," *Nature Physics*, Vol. 13, No. 8, Aug 2017, pp. 746–750.

[77] Ma, L., Nguyen, P. X., Wang, Z., Zeng, Y., Watanabe, K., Taniguchi, T., MacDonald, A. H., Mak, K. F., and Shan, J., "Strongly correlated excitonic insulator in atomic double layers," *Nature*, Vol. 598, No. 7882, Oct 2021, pp. 585–589.

[78] Zhang, Z., Regan, E. C., Wang, D., Zhao, W., Wang, S., Sayyad, M., Yumigeta, K., Watanabe, K., Taniguchi, T., Tongay, S., Crommie, M., Zettl, A., Zaletel, M. P., and Wang, F., "Correlated interlayer exciton insulator in double layers of monolayer WSe2 and moiré WS2/WSe2," 2021.

[79] Gu, J., Ma, L., Liu, S., Watanabe, K., Taniguchi, T., Hone, J. C., Shan, J., and Mak, K. F., "Dipolar excitonic insulator in a moiré lattice," *Nature Physics*, Vol. 18, No. 4, Apr 2022, pp. 395–400.

[80] Horng, J., Stroucken, T., Zhang, L., Paik, E. Y., Deng, H., and Koch, S. W., "Observation of interlayer excitons in $\mathrm{MoSe_2}$ single crystals," *Phys. Rev. B*, Vol. 97, Jun 2018, pp. 241404.

[81] Gerber, I. C., Courtade, E., Shree, S., Robert, C., Taniguchi, T., Watanabe, K., Balocchi, A., Renucci, P., Lagarde, D., Marie, X., and Urbaszek, B., "Interlayer excitons in bilayer MoS_2 with strong oscillator strength up to room temperature," *Phys. Rev. B*, Vol. 99, Jan 2019, pp. 035443.

[82] Rivera, P., Schaibley, J. R., Jones, A. M., Ross, J. S., Wu, S., Aivazian, G., Klement, P., Seyler, K., Clark, G., Ghimire, N. J., Yan, J., Mandrus, D. G., Yao, W., and Xu, X., "Observation of long-lived interlayer excitons in monolayer MoSe2–WSe2 heterostructures," *Nature Communications*, Vol. 6, No. 1, Feb 2015, pp. 6242.

[83] Rivera, P., Seyler, K. L., Yu, H., Schaibley, J. R., Yan, J., Mandrus, D. G., Yao, W., and Xu, X., "Valley-polarized exciton dynamics in a 2D semiconductor heterostructure," *Science*, Vol. 351, No. 6274, 2016, pp. 688–691.

[84] Zhang, L., Gogna, R., Burg, G. W., Horng, J., Paik, E., Chou, Y.-H., Kim, K., Tutuc, E., and Deng, H., "Highly valley-polarized singlet and triplet interlayer excitons in van der Waals heterostructure," *Phys. Rev. B*, Vol. 100, Jul 2019, pp. 041402.

[85] Liu, E., Barré, E., van Baren, J., Wilson, M., Taniguchi, T., Watanabe, K., Cui, Y.-T., Gabor, N. M., Heinz, T. F., Chang, Y.-C., and Lui, C. H., "Signatures of moiré trions in WSe2/MoSe2 heterobilayers," *Nature*, Vol. 594, No. 7861, Jun 2021, pp. 46–50.

[86] Brotons-Gisbert, M., Baek, H., Campbell, A., Watanabe, K., Taniguchi, T., and Gerardot, B. D., "Moiré-Trapped Interlayer Trions in a Charge-Tunable $WSe_2/MoSe_2$ Heterobilayer," *Phys. Rev. X*, Vol. 11, Aug 2021, pp. 031033.

[87] Heo, H., Sung, J. H., Cha, S., Jang, B.-G., Kim, J.-Y., Jin, G., Lee, D., Ahn, J.-H., Lee, M.-J., Shim, J. H., Choi, H., and Jo, M.-H., "Interlayer orientation-dependent light absorption and emission in monolayer semiconductor stacks," *Nature Communications*, Vol. 6, No. 1, Jun 2015, pp. 7372.

[88] Okada, M., Kutana, A., Kureishi, Y., Kobayashi, Y., Saito, Y., Saito, T., Watanabe, K., Taniguchi, T., Gupta, S., Miyata, Y., Yakobson, B. I., Shinohara, H., and Kitaura, R., "Direct and Indirect Interlayer Excitons in a van der Waals Heterostructure of hBN/WS2/MoS2/hBN," *ACS Nano*, Vol. 12, No. 3, 2018, pp. 2498–2505, PMID: 29481065.

[89] Kunstmann, J., Mooshammer, F., Nagler, P., Chaves, A., Stein, F., Paradiso, N., Plechinger, G., Strunk, C., Schüller, C., Seifert, G., Reichman, D. R., and Korn, T., "Momentum-space indirect interlayer excitons in transition-metal dichalcogenide van der Waals heterostructures," *Nature Physics*, Vol. 14, No. 8, Aug 2018, pp. 801–805.

[90] Karni, O., Barré, E., Lau, S. C., Gillen, R., Ma, E. Y., Kim, B., Watanabe, K., Taniguchi, T., Maultzsch, J., Barmak, K., Page, R. H., and Heinz, T. F., "Infrared Interlayer Exciton Emission in MoS_2/WSe_2 Heterostructures," *Phys. Rev. Lett.*, Vol. 123, Dec 2019, pp. 247402.

[91] Yuan, L., Zheng, B., Kunstmann, J., Brumme, T., Kuc, A. B., Ma, C., Deng, S., Blach, D., Pan, A., and Huang, L., "Twist-angle-dependent interlayer exciton diffusion in WS2–WSe2 heterobilayers," *Nature Materials*, Vol. 19, No. 6, Jun 2020, pp. 617–623.

[92] Tersoff, J., "Theory of semiconductor heterojunctions: The role of quantum dipoles," *Phys. Rev. B*, Vol. 30, Oct 1984, pp. 4874–4877.

[93] Ovesen, S., Brem, S., Linderälv, C., Kuisma, M., Korn, T., Erhart, P., Selig, M., and Malic, E., "Interlayer exciton dynamics in van der Waals heterostructures," *Communications Physics*, Vol. 2, No. 1, Feb 2019, pp. 23.

[94] Rivera, P., Yu, H., Seyler, K. L., Wilson, N. P., Yao, W., and Xu, X., "Interlayer valley excitons in heterobilayers of transition metal dichalcogenides," *Nature Nanotechnology*, Vol. 13, No. 11, Nov. 2018, pp. 1004–1015.

[95] Ruiz-Tijerina, D. A. and Fal'ko, V. I., "Interlayer hybridization and moiré superlattice minibands for electrons and excitons in heterobilayers of transition-metal dichalcogenides," *Phys. Rev. B*, Vol. 99, Mar 2019, pp. 125424.

[96] Komsa, H.-P. and Krasheninnikov, A. V., "Electronic structures and optical properties of realistic transition metal dichalcogenide heterostructures from first principles," *Phys. Rev. B*, Vol. 88, Aug 2013, pp. 085318.

[97] Kormányos, A., Burkard, G., Gmitra, M., Fabian, J., Zólyomi, V., Drummond, N. D., and Fal'ko, V., "k·p theory for two-dimensional transition metal dichalcogenide semiconductors," *2D Materials*, Vol. 2, No. 2, apr 2015, pp. 022001.

[98] Wang, Y., Wang, Z., Yao, W., Liu, G.-B., and Yu, H., "Interlayer coupling in commensurate and incommensurate bilayer structures of transition-metal dichalcogenides," *Phys. Rev. B*, Vol. 95, Mar 2017, pp. 115429.

[99] Yu, H., Wang, Y., Tong, Q., Xu, X., and Yao, W., "Anomalous Light Cones and Valley Optical Selection Rules of Interlayer Excitons in Twisted Heterobilayers," *Phys. Rev. Lett.*, Vol. 115, Oct 2015, pp. 187002.

[100] Miller, B., Steinhoff, A., Pano, B., Klein, J., Jahnke, F., Holleitner, A., and Wurstbauer, U., "Long-Lived Direct and Indirect Interlayer Excitons in van der Waals Heterostructures," *Nano Letters*, Vol. 17, No. 9, 2017, pp. 5229–5237, PMID: 28742367.

[101] Jiang, C., Xu, W., Rasmita, A., Huang, Z., Li, K., Xiong, Q., and Gao, W.-b., "Microsecond dark-exciton valley polarization memory in two-dimensional heterostructures," *Nature Communications*, Vol. 9, No. 1, Feb 2018, pp. 753.

[102] Ross, J. S., Wu, S., Yu, H., Ghimire, N. J., Jones, A. M., Aivazian, G., Yan, J., Mandrus, D. G., Xiao, D., Yao, W., and Xu, X., "Electrical control of neutral and charged excitons in a monolayer semiconductor," *Nature Communications*, Vol. 4, No. 1, Feb 2013, pp. 1474.

[103] Chernikov, A., van der Zande, A. M., Hill, H. M., Rigosi, A. F., Velauthapillai, A., Hone, J., and Heinz, T. F., "Electrical Tuning of Exciton Binding Energies in Monolayer WS_2," *Phys. Rev. Lett.*, Vol. 115, Sep 2015, pp. 126802.

[104] Newaz, A., Prasai, D., Ziegler, J., Caudel, D., Robinson, S., Haglund Jr., R., and Bolotin, K., "Electrical control of optical properties of monolayer MoS2," *Solid State Communications*, Vol. 155, 2013, pp. 49–52.

[105] Yu, Y., Yu, Y., Huang, L., Peng, H., Xiong, L., and Cao, L., "Giant Gating Tunability of Optical Refractive Index in Transition Metal Dichalcogenide Monolayers," *Nano Letters*, Vol. 17, No. 6, 2017, pp. 3613–3618, PMID: 28505462.

[106] Jariwala, D., Davoyan, A. R., Wong, J., and Atwater, H. A., "Van der Waals Materials for Atomically-Thin Photovoltaics: Promise and Outlook," *ACS Photonics*, Vol. 4, No. 12, 2017, pp. 2962–2970.

[107] Pospischil, A., Furchi, M. M., and Mueller, T., "Solar-energy conversion and light emission in an atomic monolayer p–n diode," *Nature Nanotechnology*, Vol. 9, No. 4, Apr 2014, pp. 257–261.

[108] Baugher, B. W. H., Churchill, H. O. H., Yang, Y., and Jarillo-Herrero, P., "Optoelectronic devices based on electrically tunable p–n diodes in a monolayer dichalcogenide," *Nature Nanotechnology*, Vol. 9, No. 4, Apr 2014, pp. 262–267.

[109] Ross, J. S., Klement, P., Jones, A. M., Ghimire, N. J., Yan, J., Mandrus, D. G., Taniguchi, T., Watanabe, K., Kitamura, K., Yao, W., Cobden, D. H., and Xu, X., "Electrically tunable excitonic light-emitting diodes based on monolayer WSe2 p–n junctions," *Nature Nanotechnology*, Vol. 9, No. 4, Apr 2014, pp. 268–272.

[110] Withers, F., Del Pozo-Zamudio, O., Mishchenko, A., Rooney, A. P., Gholinia, A., Watanabe, K., Taniguchi, T., Haigh, S. J., Geim, A. K., Tartakovskii, A. I., and Novoselov, K. S., "Light-emitting diodes by band-structure engineering in van der Waals heterostructures," *Nature Materials*, Vol. 14, No. 3, Mar 2015, pp. 301–306.

[111] Chaves, A., Azadani, J. G., Özçelik, V. O., Grassi, R., and Low, T., "Electrical control of excitons in van der Waals heterostructures with type-II band alignment," *Phys. Rev. B*, Vol. 98, Sep 2018, pp. 121302.

[112] Tang, Y., Gu, J., Liu, S., Watanabe, K., Taniguchi, T., Hone, J., Mak, K. F., and Shan, J., "Tuning layer-hybridized moiré excitons by the quantum-confined Stark effect," *Nature Nanotechnology*, Vol. 16, No. 1, Jan 2021, pp. 52–57.

[113] Yu, H., Liu, G.-B., Tang, J., Xu, X., and Yao, W., "Moiré excitons: From programmable quantum emitter arrays to spin-orbit–coupled artificial lattices," *Science Advances*, Vol. 3, No. 11, 2017, pp. e1701696.

[114] Tran, K., Moody, G., Wu, F., Lu, X., Choi, J., Kim, K., Rai, A., Sanchez, D. A., Quan, J., Singh, A., Embley, J., Zepeda, A., Campbell, M., Autry, T., Taniguchi, T.,

Watanabe, K., Lu, N., Banerjee, S. K., Silverman, K. L., Kim, S., Tutuc, E., Yang, L., MacDonald, A. H., and Li, X., "Evidence for moiré excitons in van der Waals heterostructures," *Nature*, Vol. 567, No. 7746, Mar 2019, pp. 71–75.

[115] Seyler, K. L., Rivera, P., Yu, H., Wilson, N. P., Ray, E. L., Mandrus, D. G., Yan, J., Yao, W., and Xu, X., "Signatures of moiré-trapped valley excitons in MoSe2/WSe2 heterobilayers," *Nature*, Vol. 567, No. 7746, Mar 2019, pp. 66–70.

[116] Wang, X., Zhu, J., Seyler, K. L., Rivera, P., Zheng, H., Wang, Y., He, M., Taniguchi, T., Watanabe, K., Yan, J., Mandrus, D. G., Gamelin, D. R., Yao, W., and Xu, X., "Moiré trions in MoSe2/WSe2 heterobilayers," *Nature Nanotechnology*, Vol. 16, No. 11, Nov 2021, pp. 1208–1213.

[117] Jin, C., Regan, E. C., Wang, D., Iqbal Bakti Utama, M., Yang, C.-S., Cain, J., Qin, Y., Shen, Y., Zheng, Z., Watanabe, K., Taniguchi, T., Tongay, S., Zettl, A., and Wang, F., "Identification of spin, valley and moiré quasi-angular momentum of interlayer excitons," *Nature Physics*, Vol. 15, No. 11, Nov 2019, pp. 1140–1144.

[118] Regan, E. C., Wang, D., Jin, C., Bakti Utama, M. I., Gao, B., Wei, X., Zhao, S., Zhao, W., Zhang, Z., Yumigeta, K., Blei, M., Carlström, J. D., Watanabe, K., Taniguchi, T., Tongay, S., Crommie, M., Zettl, A., and Wang, F., "Mott and generalized Wigner crystal states in WSe2/WS2 moiré superlattices," *Nature*, Vol. 579, No. 7799, Mar 2020, pp. 359–363.

[119] Tang, Y., Li, L., Li, T., Xu, Y., Liu, S., Barmak, K., Watanabe, K., Taniguchi, T., MacDonald, A. H., Shan, J., and Mak, K. F., "Simulation of Hubbard model physics in WSe2/WS2 moiré superlattices," *Nature*, Vol. 579, No. 7799, Mar 2020, pp. 353–358.

[120] Xu, Y., Liu, S., Rhodes, D. A., Watanabe, K., Taniguchi, T., Hone, J., Elser, V., Mak, K. F., and Shan, J., "Correlated insulating states at fractional fillings of moiré superlattices," *Nature*, Vol. 587, No. 7833, Nov 2020, pp. 214–218.

[121] Kennes, D. M., Claassen, M., Xian, L., Georges, A., Millis, A. J., Hone, J., Dean, C. R., Basov, D. N., Pasupathy, A. N., and Rubio, A., "Moiré heterostructures as a condensed-matter quantum simulator," *Nature Physics*, Vol. 17, No. 2, Feb 2021, pp. 155–163.

[122] Siegman, A. E., *Lasers*, University Science Books, 1986.

[123] Vahala, K. J., "Optical microcavities," *Nature*, Vol. 424, No. 6950, Aug 2003, pp. 839–846.

[124] Saleh, B. E. A. and Teich, M. C., *Fundamentals of photonics*, Wiley series in pure and applied optics, Wiley, 1991.

[125] Srinivasan, K., Borselli, M., Painter, O., Stintz, A., and Krishna, S., "Cavity Q, mode volume, and lasing threshold in small diameter AlGaAs microdisks with embedded quantum dots," *Opt. Express*, Vol. 14, No. 3, Feb 2006, pp. 1094–1105.

[126] Fowles, G. R., *Introduction to Modern Optics*, Dover Books on Physics, Dover Publications, 2012.

[127] Osting, B., "Bragg structure and the first spectral gap," *Applied Mathematics Letters*, Vol. 25, No. 11, 2012, pp. 1926–1930.

[128] Yamamoto, Y., Tassone, F., and Cao, H., *Semiconductor cavity quantum electrodynamics*, Springer tracts in modern physics, Springer, 2000.

[129] Rosenblatt, D., Sharon, A., and Friesem, A., "Resonant grating waveguide structures," *IEEE Journal of Quantum Electronics*, Vol. 33, No. 11, 1997, pp. 2038–2059.

[130] Fan, S. and Joannopoulos, J. D., "Analysis of guided resonances in photonic crystal slabs," *Phys. Rev. B*, Vol. 65, Jun 2002, pp. 235112.

[131] Zhang, L., Hu, J., and Deng, H., "Chapter Two - Microcavity exciton polaritons," *Semiconductor Quantum Science and Technology*, edited by S. T. Cundiff and M. Kira, Vol. 105 of *Semiconductors and Semimetals*, Elsevier, 2020, pp. 29–87.

[132] Hopfield, J. J., "Theory of the Contribution of Excitons to the Complex Dielectric Constant of Crystals," *Phys. Rev.*, Vol. 112, Dec 1958, pp. 1555–1567.

[133] Kleppner, D., "Inhibited Spontaneous Emission," *Phys. Rev. Lett.*, Vol. 47, Jul 1981, pp. 233–236.

[134] Yariv, A. and Yeh, P., *Optical waves in crystals*, Wiley series in pure and applied optics, Wiley, 1984.

[135] Psilodimitrakopoulos, S., Mouchliadis, L., Paradisanos, I., Lemonis, A., Kioseoglou, G., and Stratakis, E., "Ultrahigh-resolution nonlinear optical imaging of the armchair orientation in 2D transition metal dichalcogenides," *Light: Science & Applications*, Vol. 7, No. 5, May 2018, pp. 18005–18005.

[136] Weisbuch, C., Nishioka, M., Ishikawa, A., and Arakawa, Y., "Observation of the coupled exciton-photon mode splitting in a semiconductor quantum microcavity," *Phys. Rev. Lett.*, Vol. 69, Dec 1992, pp. 3314–3317.

[137] Byrnes, T., Kim, N. Y., and Yamamoto, Y., "Exciton–polariton condensates," *Nature Physics*, Vol. 10, No. 11, Nov. 2014, pp. 803–813.

[138] Liu, X., Galfsky, T., Sun, Z., Xia, F., Lin, E.-C., Lee, Y.-H., Kéna-Cohen, S., and Menon, V. M., "Strong light–matter coupling in two-dimensional atomic crystals," *Nature Photonics*, Vol. 9, No. 1, Jan 2015, pp. 30–34.

[139] Dufferwiel, S., Schwarz, S., Withers, F., Trichet, A. A. P., Li, F., Sich, M., Del Pozo-Zamudio, O., Clark, C., Nalitov, A., Solnyshkov, D. D., Malpuech, G., Novoselov, K. S., Smith, J. M., Skolnick, M. S., Krizhanovskii, D. N., and Tartakovskii, A. I., "Exciton-polaritons in van der Waals heterostructures embedded in tunable microcavities," *Nature Communications*, Vol. 6, No. 1, Oct 2015, pp. 8579.

[140] Lundt, N., Klembt, S., Cherotchenko, E., Betzold, S., Iff, O., Nalitov, A. V., Klaas, M., Dietrich, C. P., Kavokin, A. V., Höfling, S., and Schneider, C., "Room-temperature Tamm-plasmon exciton-polaritons with a WSe2 monolayer," *Nature Communications*, Vol. 7, No. 1, Oct 2016, pp. 13328.

[141] Wang, S., Li, S., Chervy, T., Shalabney, A., Azzini, S., Orgiu, E., Hutchison, J. A., Genet, C., Samorì, P., and Ebbesen, T. W., "Coherent Coupling of WS2 Monolayers with Metallic Photonic Nanostructures at Room Temperature," *Nano Letters*, Vol. 16, No. 7, 2016, pp. 4368–4374, PMID: 27266674.

[142] Zhang, L., Gogna, R., Burg, W., Tutuc, E., and Deng, H., "Photonic-crystal exciton-polaritons in monolayer semiconductors," *Nature Communications*, Vol. 9, No. 1, 2018, pp. 713.

[143] Lundt, N., Klaas, M., Sedov, E., Waldherr, M., Knopf, H., Blei, M., Tongay, S., Klembt, S., Taniguchi, T., Watanabe, K., Schulz, U., Kavokin, A., Höfling, S., Eilenberger, F., and Schneider, C., "Magnetic-field-induced splitting and polarization of monolayer-based valley exciton polaritons," *Phys. Rev. B*, Vol. 100, Sep 2019, pp. 121303.

[144] Dufferwiel, S., Lyons, T. P., Solnyshkov, D. D., Trichet, A. A. P., Withers, F., Schwarz, S., Malpuech, G., Smith, J. M., Novoselov, K. S., Skolnick, M. S., Krizhanovskii, D. N., and Tartakovskii, A. I., "Valley-addressable polaritons in atomically thin semiconductors," *Nature Photonics*, Vol. 11, No. 8, Aug 2017, pp. 497–501.

[145] Lundt, N., Dusanowski, Ł., Sedov, E., Stepanov, P., Glazov, M. M., Klembt, S., Klaas, M., Beierlein, J., Qin, Y., Tongay, S., Richard, M., Kavokin, A. V., Höfling, S., and Schneider, C., "Optical valley Hall effect for highly valley-coherent exciton-polaritons in an atomically thin semiconductor," *Nature Nanotechnology*, Vol. 14, No. 8, Aug. 2019, pp. 770–775.

[146] Rupprecht, C., Lundt, N., Wurdack, M., Stepanov, P., Estrecho, E., Richard, M., Ostrovskaya, E. A., Höfling, S., and Schneider, C., "Micro-mechanical assembly and characterization of high-quality Fabry–Pérot microcavities for the integration of two-dimensional materials," *Applied Physics Letters*, Vol. 118, No. 10, 2021, pp. 103103.

[147] Kedawat, G., Srivastava, S., Jain, V. K., Kumar, P., Kataria, V., Agrawal, Y., Gupta, B. K., and Vijay, Y. K., "Fabrication of Artificially Stacked Ultrathin ZnS/MgF2 Multilayer Dielectric Optical Filters," *ACS Applied Materials & Interfaces*, Vol. 5, No. 11, 2013, pp. 4872–4877.

[148] Qu, Y., Hou, S., and Forrest, S. R., "Temperature-Dependence of an Amorphous Organic Thin Film Polariton Laser," *ACS Photonics*, Vol. 7, No. 4, 2020, pp. 867–872.

[149] Geim, A. K. and Grigorieva, I. V., "Van der Waals heterostructures," *Nature*, Vol. 499, Jul 2013, pp. 419–425.

[150] Zhang, C., Chuu, C.-P., Ren, X., Li, M.-Y., Li, L.-J., Jin, C., Chou, M.-Y., and Shih, C.-K., "Interlayer couplings, Moiré patterns, and 2D electronic superlattices in MoS_2/WSe_2 hetero-bilayers," *Science Advances*, Vol. 3, No. 1, 2017.

[151] Fang, H., Battaglia, C., Carraro, C., Nemsak, S., Ozdol, B., Kang, J. S., Bechtel, H. A., Desai, S. B., Kronast, F., Unal, A. A., Conti, G., Conlon, C., Palsson, G. K., Martin, M. C., Minor, A. M., Fadley, C. S., Yablonovitch, E., Maboudian, R., and Javey, A., "Strong interlayer coupling in van der Waals heterostructures built from single-layer chalcogenides," *Proceedings of the National Academy of Sciences*, Vol. 111, No. 17, 2014, pp. 6198–6202.

[152] Eaton, S. W., Fu, A., Wong, A. B., Ning, C.-Z., and Yang, P., "Semiconductor nanowire lasers," *Nature Reviews Materials*, Vol. 1, May 2016, pp. 16028.

[153] Noginov, M. A., Zhu, G., Belgrave, A. M., Bakker, R., Shalaev, V. M., Narimanov, E. E., Stout, S., Herz, E., Suteewong, T., and Wiesner, U., "Demonstration of a spaser-based nanolaser," *Nature*, Vol. 460, Aug 2009, pp. 1110–1112.

[154] Noda, S., "Seeking the Ultimate Nanolaser," *Science*, Vol. 314, No. 5797, 2006, pp. 260–261.

[155] Wu, S., Buckley, S., Schaibley, J. R., Feng, L., Yan, J., Mandrus, D. G., Hatami, F., Yao, W., Vuckovic, J., Majumdar, A., and Xu, X., "Monolayer semiconductor nanocavity lasers with ultralow thresholds," *Nature*, Vol. 520, Mar 2015, pp. 69–72.

[156] Ye, Y., Wong, Z. J., Lu, X., Ni, X., Zhu, H., Chen, X., Wang, Y., and Zhang, X., "Monolayer excitonic laser," *Nature Photonics*, Vol. 9, Oct 2015, pp. 733–737.

[157] Salehzadeh, O., Djavid, M., Tran, N. H., Shih, I., and Mi, Z., "Optically Pumped Two-Dimensional MoS_2 Lasers Operating at Room-Temperature," *Nano Letters*, Vol. 15, No. 8, 2015, pp. 5302–5306.

[158] Li, Y., Zhang, J., Huang, D., Sun, H., Fan, F., Feng, J., Wang, Z., and Ning, C. Z., "Room-temperature continuous-wave lasing from monolayer molybdenum ditelluride integrated with a silicon nanobeam cavity," *Nature Nanotechnology*, Vol. 12, Jul 2017, pp. 987–992.

[159] Shang, J., Cong, C., Wang, Z., Peimyoo, N., Wu, L., Zou, C., Chen, Y., Chin, X. Y., Wang, J., Soci, C., Huang, W., and Yu, T., "Room-temperature 2D semiconductor activated vertical-cavity surface-emitting lasers," *Nature Communications*, Vol. 8, No. 1, 2017, pp. 543.

[160] Zhao, L., Shang, Q., Gao, Y., Shi, J., Liu, Z., Chen, J., Mi, Y., Yang, P., Zhang, Z., Du, W., Hong, M., Liang, Y., Xie, J., Hu, X., Peng, B., Leng, J., Liu, X., Zhao, Y., Zhang, Y., and Zhang, Q., "High-Temperature Continuous-Wave Pumped Lasing

from Large-Area Monolayer Semiconductors Grown by Chemical Vapor Deposition," *ACS Nano, Article ASAP*, 2018.

[161] Reeves, L., Wang, Y., and Krauss, T. F., "2D Material Microcavity Light Emitters: To Lase or Not to Lase?" *Advanced Optical Materials*, Vol. 6, No. 19, 2018, pp. 1800272.

[162] Butov, L. V., Zrenner, A., Abstreiter, G., Böhm, G., and Weimann, G., "Condensation of Indirect Excitons in Coupled AlAs/GaAs Quantum Wells," *Phys. Rev. Lett.*, Vol. 73, Jul 1994, pp. 304–307.

[163] Rigosi, A. F., Hill, H. M., Li, Y., Chernikov, A., and Heinz, T. F., "Probing Interlayer Interactions in Transition Metal Dichalcogenide Heterostructures by Optical Spectroscopy: MoS_2/WS_2 and $MoSe_2/WSe_2$," *Nano Letters*, Vol. 15, No. 8, 2015, pp. 5033–5038.

[164] Jin, Z., Li, X., Mullen, J. T., and Kim, K. W., "Intrinsic transport properties of electrons and holes in monolayer transition-metal dichalcogenides," *Phys. Rev. B*, Vol. 90, Jul 2014, pp. 045422.

[165] Spivak, B. and Luryi, S., "Is There a Linewidth Theory for Semiconductor Lasers?" *Future Trends in Microelectronics*, Wiley-Blackwell, 2007, pp. 68–76.

[166] Deng, H., Solomon, G. S., Hey, R., Ploog, K. H., and Yamamoto, Y., "Spatial Coherence of a Polariton Condensate," *Phys. Rev. Lett.*, Vol. 99, Sep 2007, pp. 126403.

[167] Hoang, T. B., Akselrod, G. M., Yang, A., Odom, T. W., and Mikkelsen, M. H., "Millimeter-Scale Spatial Coherence from a Plasmon Laser," *Nano Letters*, Vol. 17, No. 11, Nov 2017, pp. 6690–6695.

[168] Daskalakis, K. S., Maier, S. A., and Kéna-Cohen, S., "Spatial Coherence and Stability in a Disordered Organic Polariton Condensate," *Phys. Rev. Lett.*, Vol. 115, Jul 2015, pp. 035301.

[169] Jin, C., Regan, E. C., Yan, A., Utama, M. I. B., Wang, D., Zhao, S., Qin, Y., Yang, S., Zheng, Z., Shi, S., Watanabe, K., Taniguchi, T., Tongay, S., Zettl, A., and Wang, F., "Observation of moiré excitons in WSe_2 /WS_2 heterostructure superlattices," *Nature*, Vol. 567, No. 7746, March 2019, pp. 76.

[170] Kirstaedter, N., Ledentsov, N. N., Grundmann, M., Bimberg, D., Ustinov, V. M., Ruvimov, S. S., Maximov, M. V., Kop'ev, P. S., Alferov, Z. I., Richter, U., Werner, P., Gosele, U., and Heydenreich, J., "Low threshold, large T/sub o/ injection laser emission from (InGa)As quantum dots," *Electronics Letters*, Vol. 30, No. 17, Aug. 1994, pp. 1416–1417.

[171] Shahnazaryan, V., Kyriienko, O., and Shelykh, I. A., "Adiabatic preparation of a cold exciton condensate," *Physical Review B*, Vol. 91, No. 8, Feb. 2015, pp. 085302.

[172] Zhang, L., Zhang, Z., Wu, F., Wang, D., Gogna, R., Hou, S., Watanabe, K., Taniguchi, T., Kulkarni, K., Kuo, T., Forrest, S. R., and Deng, H., "Twist-angle dependence of moiré excitons in WS2/MoSe2 heterobilayers," *Nature Communications*, Vol. 11, No. 1, Dec. 2020, pp. 5888.

[173] Kiemle, J., Sigger, F., Lorke, M., Miller, B., Watanabe, K., Taniguchi, T., Holleitner, A., and Wurstbauer, U., "Hybridized indirect excitons in MoS2/WS2 heterobilayers," 2018.

[174] Zhang, L., Wu, F., Hou, S., Zhang, Z., Chou, Y.-H., Watanabe, K., Taniguchi, T., Forrest, S. R., and Deng, H., "Van der Waals heterostructure polaritons with moiré-induced nonlinearity," *Nature*, Vol. 591, No. 7848, March 2021, pp. 61–65.